Inorganic Chemistry

Article

pubs.acs.org/IC

Environmental Influence on the Single-Molecule Magnet Behavior of $[Mn^{III}_6Cr^{III}]^{3+}$: Molecular Symmetry versus Solid-State Effects

Veronika Hoeke,[†] Maik Heidemeier,[†] Erich Krickemeyer,[†] Anja Stammler,[†] Hartmut Bögge,[†] Jürgen Schnack,[‡] Andrei Postnikov,[§] and Thorsten Glaser*[,†]

[†]Lehrstuhl für Anorganische Chemie I, Fakultät für Chemie, Universität Bielefeld, Universitätsstr. 25, D-33615 Bielefeld, Germany

[‡]Fakultät für Physik, Universität Bielefeld, Universitätsstr. 25, D-33615 Bielefeld, Germany

[§]University of Lorraine—Institut de Chimie, Physique et Matériaux, LCP-A2MC, 1 Bd Arago, F-57078 Metz, France

Supporting Information

ABSTRACT: The structural, spectroscopic, and magnetic properties of a series of $[\mathbf{Mn^{III}_6Cr^{III}}]^{3+}$ (= $[\{(talen^{t\text{-}Bu_2})\text{-}Mn^{III}\}_3\{Cr^{III}(CN)_6\}]^{3+}$) compounds have been investigated by single-crystal X-ray diffraction (XRD), Fourier transform infrared (FT-IR) and electronic absorption spectroscopy, elemental analysis, electro spray ionization−mass spectrometry (ESI-MS) and matrix-assisted laser desorption ionization−mass spectrometry (MALDI-MS), cyclic voltammetry, AC and DC magnetic measurements, as well as theoretical analysis. The crystal structures obtained with $[Cr^{III}(CN)_6]^{3-}$ as a counterion exhibit (quasi-)one-dimensional (1D) chains formed by hydrogen-bonded (**1**) or covalently linked (**2**) trications and trianions. The rod-shaped anion lactate enforces a rod packing of the $[\mathbf{Mn^{III}_6Cr^{III}}]^{3+}$ complexes in the highly symmetric space group $R\bar{3}$ (**3**) with a collinear arrangement of the molecular S_6 axes. Incorporation of the spherical anion BPh_4^- leads to less-symmetric crystal structures (**4**−**6**) with noncollinear orientations of the $[\mathbf{Mn^{III}_6Cr^{III}}]^{3+}$ complexes, as evidenced by the angle between the approximate molecular C_3 axes taking no specific values in the range of 2°−69°. AC magnetic measurements on freshly isolated crystals (**1a** and **3a**−**6a**), air-dried crystals (**3b**−**6b**), and vacuum-dried powder samples (**3c**−**6c**) indicate single-molecule magnet (SMM) behavior for all samples with U_{eff} values up to 28 K. The DC magnetic data are analyzed by a full-matrix diagonalization of the appropriate spin-Hamiltonian including isotropic exchange, zero-field splitting, and Zeeman interaction, taking into account the relative orientation of the **D**-tensors. Simulations for **3a**−**6a** and **3c**−**6c** indicate a weak antiferromagnetic exchange between the Mn^{III} ions in the trinuclear subunits (J_{Mn-Mn} = −0.70 to −0.85 cm^{-1}, $\hat{H}_{ex} = -2\sum_{i<j} J_{ij}\hat{\mathbf{S}}_i\cdot\hat{\mathbf{S}}_j$) that is overcome by the stronger antiferromagnetic interaction via the Cr−C≡N−Mn pathway (J_{Cr-Mn} = −3.00 to −5.00 cm^{-1}), leading to an overall ferrimagnetic coupling scheme with an $S_t = {}^{21}/_2$ spin ground state. The differences in U_{eff}, J_{Mn-Mn}, and J_{Cr-Mn} for the investigated samples are rationalized in terms of subtle variations in the molecular and crystal structures. In particular, a magnetostructural correlation between the Mn−$N^{C\equiv N}$ bond length and the J_{Cr-Mn} exchange coupling is inferred from the magnetic measurements and corroborated by DFT calculations. The results of this detailed study on $[\mathbf{Mn^{III}_6Cr^{III}}]^{3+}$ allow the formulation of some key recipes for a rational improvement of the SMM behavior.

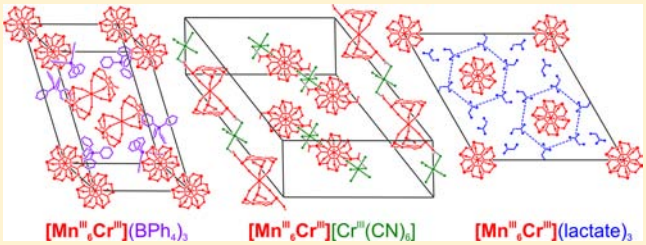

INTRODUCTION

Single-molecule magnets (SMMs) are coordination compounds that exhibit a hysteresis of the magnetization which is of purely molecular origin.[1−6] This phenomenon is related to a slow relaxation of the magnetization due to an energy barrier for spin reversal, which arises from the combination of a high-spin ground state S_t and a strong magnetic anisotropy D_{S_t}. In addition to allowing for the direct observation of quantum effects, these bistable molecules attract attention because of their potential applications in information storage and quantum computing.[7−16] Besides the archetype family of $\mathbf{Mn_{12}}$ (= $[Mn^{III}_8Mn^{IV}_4O_{12}(O_2CR)_{16}(OH_2)_4]$) SMMs,[1,2,17−26] many other SMMs based on 3d transition-metal ions have been described,[4,27−37] among which manganese-based SMMs are particularly numerous.[31,32,38−45] On the other hand, there is a growing interest in SMMs containing 4d and 5d transition-metal ions[46−55] and lanthanide ions.[56−67]

The relaxation of the magnetization in SMMs may proceed via a thermal pathway over the top of the anisotropy barrier or via quantum-mechanical magnetization tunneling (QTM) through the anisotropy barrier. The probability of QTM is related to the magnitude of the rhombic component of the magnetic anisotropy E_{S_t}, which is controlled by symmetry.[3] As E_{S_t} vanishes for systems of at least C_3 symmetry, the overall molecular symmetry should be at least trigonal, to minimize the QTM, but lower than cubic, to avoid an isotropic system. Hence, the design of an SMM requires not only a high-spin

Received: June 29, 2012
Published: September 27, 2012

ground state S_t and some source of magnetic anisotropy, but also a control of the molecular topology.

In order to meet these requirements, we have designed the C_3 symmetric ligand system triplesalen, which combines the phloroglucinol bridging unit for high-spin ground states S_t by the spin-polarization mechanism[68−72] with a salen-like ligand environment for single-site magnetic anisotropies D_i by a strong tetragonal ligand field.[72−76] The C_3 symmetry of the ligand should result in C_3 symmetric complexes which have, by symmetry, a rhombicity of $E_{S_t} = 0$. The trinuclear complexes of the triplesalen ligand $[(\text{talen}^{t\text{-Bu}_2})M^t_3]^{m+}$ (shown in Chart 1 for

Chart 1

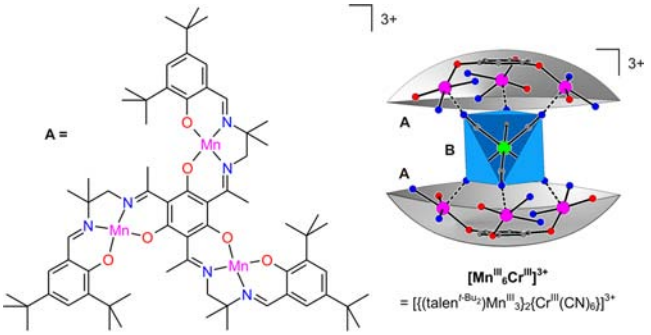

Complex	Abbreviation for [a]			
	X-ray diffraction sample	samples for magnetic measurements		
		freshly isolated crystals	air-dried crystals	vacuum-dried powder
$[Mn^{III}_6Cr^{III}][Cr^{III}(CN)_6]$	1	1a	-	-
$[Mn^{III}_6Cr^{III}](\mu_2\text{-}[Cr^{III}(CN)_6])$	2	-	-	-
$[Mn^{III}_6Cr^{III}](lac)_3$	3	3a	3b	3c
	4	4a	4b	4c
$[Mn^{III}_6Cr^{III}](BPh_4)_3$	5	5a	5b	5c
	6	6a	6b	6c

[a] For detailed coordinated and non-coordinated solvent content see experimental section.

$M^t = Mn^{III}$ (**A**)) are indeed C_3 symmetric and exhibit a bowl-shaped molecular structure[74,77] which preorganizes the axial coordination sites of the metal-salen subunits for the complementary binding of three facial nitrogen atoms of a hexacyanometallate (**B** for $M^c = Cr^{III}$). Hence, the ligand folding allows for the targeted construction of heptanuclear complexes $[\mathbf{M^t_6M^c}]^{n+}$ (= $[\{(\text{talen}^{t\text{-Bu}_2})M^t_3\}_2\{M^c(CN)_6\}]^{n+}$) from two trinuclear triplesalen building blocks and one hexacyanometallate by relying on the concepts of supramolecular chemistry,[78−80] i.e. the molecular recognition of three preorganized and complementary molecular building blocks provides the driving force for their association to a heptanuclear complex, in analogy to the key-and-lock principle. Importantly, this modular approach allows the fine-tuning of steric and electronic properties of the individual building blocks without losing the driving force for the assembly of the entire entity.

The success of our design concept was confirmed by the formation and the structural and magnetic properties of $[\mathbf{Mn^{III}_6Cr^{III}}]^{3+}$,[81] which is indeed an SMM. The molecule is approximately C_3 symmetric, and the magnetic data indicate a ferrimagnetic coupling scheme resulting in an $S_t = {}^{21}/_2$ spin ground state with a sizable magnetic anisotropy D_{S_t}. The SMM nature of $[\mathbf{Mn^{III}_6Cr^{III}}]^{3+}$ as indicated by a nonzero out-of-phase component of the AC susceptibility was confirmed by a hysteresis of the magnetization in single-crystal measurements.

The general applicability of the supramolecular approach for the construction of heptanuclear complexes of the $[\mathbf{M^t_6M^c}]^{n+}$ type was demonstrated by our successful synthesis of the isostructural series $[\mathbf{Mn^{III}_6Fe^{III}}]^{3+}$,[82] $[\mathbf{Mn^{III}_6Co^{III}}]^{3+}$,[83] and $[\mathbf{Mn^{III}_6Mn^{III}}]^{3+}$,[84] indicating a high stability of the $[\mathbf{M^t_6M^c}]^{n+}$ complex. A detailed comparison of $[\mathbf{Mn^{III}_6Cr^{III}}]^{3+}$ with the related tetranuclear complex $[\mathbf{Mn^{III}_3Cr^{III}}]^{3+}$ (= $[\{(\text{talen}^{t\text{-Bu}_2})\text{-}Mn^{III}_3\}\{(Me_3tacn)Cr^{III}(CN)_3\}]^{3+}$)[85] identified van der Waals-type contacts between the two trinuclear triplesalen building blocks in $[\mathbf{M^t_6M^c}]^{n+}$ as the main source of its strong driving force for formation and its high stability.

While this design approach does allow the fine-tuning of steric and electronic properties of the individual building blocks of $[\mathbf{M^t_6M^c}]^{n+}$, e.g., by incorporating different metal ions or varying the substituents on the ligand backbone, it does not permit a predetermination or targeted variation of structural parameters such as bond distances and angles, ligand folding, the extent of Jahn−Teller distortions, or the exact molecular symmetry in the solid state. Furthermore, aspects of the crystal structure such as the overall crystal symmetry, the packing and relative orientation of the individual SMM complexes in the crystal, the presence or absence of (weak) intermolecular interactions between the complexes, or the nature and number of solvent molecules of crystallization and their arrangement relative to the SMM complexes within the crystal structure, are difficult to control. However, such rather slight modifications of the molecular environment were shown to have a strong impact on the SMM properties of $\mathbf{Mn_{12}}$[17−26,86−95] and other families of SMMs.[37,96−106]

In an attempt to systematically evaluate the influence of environmental changes on SMM behavior, we have taken advantage of the high stability of the $[\mathbf{Mn^{III}_6Cr^{III}}]^{3+}$ complex to synthesize and structurally and magnetically characterize a series of $[\mathbf{Mn^{III}_6Cr^{III}}]^{3+}$ SMMs differing in the counterion and/or the solvent molecules of crystallization (see Chart 1). The use of $[Cr^{III}(CN)_6]^{3-}$ as counterion led to the isolation of a zero-dimensional (0D) $[\mathbf{Mn^{III}_6Cr^{III}}][Cr^{III}(CN)_6]$ compound (**1**) as well as a one-dimensional (1D) $[\mathbf{Mn^{III}_6Cr^{III}}](\mu_2\text{-}[Cr^{III}\text{-}(CN)_6])$ chain compound (**2**). In order to enforce a high crystal symmetry by rod packing, we employed the rod-shaped anion lactate (= lac), which resulted in the crystallization of $[\mathbf{Mn^{III}_6Cr^{III}}](lac)_3$ (**3**) in the highly symmetric space group $R\bar{3}$ with the molecular S_6 axes of the $[\mathbf{Mn^{III}_6Cr^{III}}]^{3+}$ complexes all aligned with the *c*-axis of the unit cell. Furthermore, we succeeded in crystallizing two more solvates of $[\mathbf{Mn^{III}_6Cr^{III}}](BPh_4)_3$ from acetonitrile (**4**) and acetone (**5**), in addition to our first-reported[81] $[\mathbf{Mn^{III}_6Cr^{III}}](BPh_4)_3$ SMM obtained from acetonitrile/ether (**6**). All compounds are rigorously characterized structurally, spectroscopically, and magnetically by DC and AC measurements. The magnetic properties are analyzed by the full anisotropic spin-Hamiltonian to extract the exchange coupling constants (J_i) and the local zero-field splittings (D_i). This analysis is supported by density functional theory (DFT) calculations. The series of $[\mathbf{Mn^{III}_6Cr^{III}}]^{3+}$ compounds **1**−**6** allows a detailed investigation of the influence of a variety of environmental factors on the SMM properties, which we report herein.

EXPERIMENTAL SECTION

Preparation of Compounds. $H_6\text{talen}^{t\text{-Bu}_2}$ {= 2,4,6-tris{1-[2-(3,5-di-*tert*-butylsalicylaldimino)-2-methylpropylimino]-ethyl}-1,3,5-trihydroxybenzene} was synthesized as described previously.[77,107] Filter

dx.doi.org/10.1021/ic301406j | *Inorg. Chem.* 2012, 51, 10929−10954

paper for extremely fine precipitates was obtained from MACHERY-NAGEL (Grade No. 5, MN 619 de).

[{(talen$^{t\text{-}Bu_2}$)(Mn^{III}(MeOH))$_3$}$_2${Cr^{III}(CN)$_6$}][Cr^{III}(CN)$_6$]·14MeOH·5H$_2$O (**1**). A suspension of H$_6$talen$^{t\text{-}Bu_2}$ (111 mg, 0.100 mmol) and Mn(OAc)$_2$·4H$_2$O (69 mg, 0.28 mmol) in methanol (40 mL) was heated at reflux for 2 h. The resulting brown solution was cooled to room temperature, purged with air for 30 min, and heated at reflux for an additional 2 h. After cooling to room temperature, the reaction solution was treated with a solution of K$_3$[Cr(CN)$_6$] (71 mg, 0.22 mmol) in water (1.5 mL). Stirring of the reaction mixture at room temperature for 1 min resulted in the formation of a brown precipitate, which was removed using filter paper for extremely fine precipitates (vide supra). The filtrate was allowed to stand at room temperature. The precipitated small brown crystals were removed after 90, 180, and 300 min, using filter paper for extremely fine precipitates (vide supra). Slow evaporation of the filtrate then afforded large brown crystals. Yield: 33 mg (19%). ESI-MS (MeOH): *m*/*z*: 916.2 [{(talen$^{t\text{-}Bu_2}$)-Mn$_3$}$_2${Cr(CN)$_6$}]$^{3+}$; MALDI-TOF-MS (matrix DCTB): *m*/*z*: 2747 [{(talen$^{t\text{-}Bu_2}$)Mn$_3$}$_2${Cr(CN)$_6$}]$^+$; IR (KBr): $\tilde{\nu}$ (cm^{-1}) = 2959 m, 2907 m, 2868 m, 2147 w, 2126 vw, 1613 s, 1570 s, 1535 s, 1491 vs, 1437 m, 1393 m, 1364 m, 1341 m, 1312 m, 1275 s, 1254 s, 1188 m, 1160 m, 1063 w, 1026 w, 847 m, 820 w, 781 w, 750 w, 644 w, 608 w, 577 m, 552 m. Elemental analysis (%): calcd for [{(talen$^{t\text{-}Bu_2}$)-(Mn^{III}(MeOH))$_3$}$_2${Cr^{III}(CN)$_6$}][Cr^{III}(CN)$_6$]·3MeOH·8H$_2$O (**1a**, C$_{159}$H$_{244}$N$_{24}$O$_{29}$Cr$_2$Mn$_6$): C 56.34, H 7.26, N 9.92; found: C 56.00, H 6.99, N 10.29.

[{(talen$^{t\text{-}Bu_2}$)Mn$^{III}_3$(MeOH)(H$_2$O)}$_2${Cr^{III}(CN)$_6$}](μ$_2$-[Cr^{III}(CN)$_6$])·9MeOH·2H$_2$O (**2**). A suspension of H$_6$talen$^{t\text{-}Bu_2}$ (500 mg, 0.450 mmol) and Mn(OAc)$_2$·4H$_2$O (310 mg, 1.26 mmol) in methanol (200 mL) was heated at reflux for 2 h. The resulting brown solution was cooled to room temperature, purged with air for 30 min, and heated at reflux for an additional 2 h. The hot reaction solution was then treated with a solution of K$_3$[Cr(CN)$_6$] (320 mg, 0.983 mmol) in water (5 mL) and subsequently with a solution of D,L-Na(lac) (600 mg, 5.35 mmol) in water (10 mL). Stirring of the hot reaction mixture at room temperature for 1 min resulted in the formation of a brown precipitate, which was removed from the hot suspension using filter paper for extremely fine precipitates (vide supra). The filtrate was allowed to stand at room temperature. The precipitated brown crystals were removed after 90, 180, and 300 min, using filter paper for extremely fine precipitates (vide supra). Slow evaporation of the filtrate then afforded brown crystals suitable for X-ray diffraction (XRD) studies and some colorless precipitate, which were collected by filtration after 7 days and dried in air. The colorless precipitate was removed from the crystals by heating the suspension of both in methanol (160 mL) to reflux for 15 min without stirring, and subsequently collecting the undissolved crystals from the hot suspension by filtration. Yield: 150 mg (21%). IR (KBr): $\tilde{\nu}$ (cm^{-1}) = 2959 m, 2907 m, 2868 m, 2149 w, 2126 vw, 1613 s, 1572 s, 1535 s, 1491 vs, 1437 m, 1395 m, 1364 m, 1341 m, 1314 m, 1275 s, 1254 s, 1188 m, 1159 m, 1065 w, 1026 w, 847 m, 820 w, 781 w, 750 w, 646 w, 608 w, 577 m, 552 m.

[{(talen$^{t\text{-}Bu_2}$)(Mn^{III}(MeOH))$_3$}$_2${Cr^{III}(CN)$_6$}](lac)$_3$·9MeOH (**3**). A suspension of H$_6$talen$^{t\text{-}Bu_2}$ (222 mg, 0.200 mmol) and Mn(OAc)$_2$·4H$_2$O (138 mg, 0.563 mmol) in methanol (80 mL) was heated at reflux for 2 h. The resulting brown solution was cooled to room temperature, purged with air for 30 min, and heated at reflux for an additional 2 h. After cooling to room temperature, the reaction solution was treated with a solution of K$_3$[Cr(CN)$_6$] (32 mg, 0.099 mmol) in water (2 mL). The reaction mixture was stirred at room temperature for 60 min and filtered using filter paper for extremely fine precipitates (vide supra). A solution of D,L-Na(lac) (1010 mg, 9.013 mmol) in methanol (12 mL) was added to the filtrate. The reaction mixture was stirred at room temperature for 30 min and filtered again, using filter paper for extremely fine precipitates (vide supra). Slow evaporation of the solvent from the filtrate afforded a pasty black precipitate, which was collected by filtration and redissolved in methanol. The solution was filtered using filter paper for extremely fine precipitates (vide supra). Slow evaporation of the solvent from the filtrate led to the formation of brown crystals. Yield: 23 mg (7%). ESI-MS (CH$_2$Cl$_2$): *m*/*z*: 916.3 [{(talen$^{t\text{-}Bu_2}$)Mn$_3$}$_2${Cr(CN)$_6$}]$^{3+}$; MALDI-TOF-MS (matrix DCTB): *m*/*z*: 2748.1 [{(talen$^{t\text{-}Bu_2}$)Mn$_3$}$_2${Cr(CN)$_6$}]$^+$; IR (KBr): $\tilde{\nu}$ (cm^{-1}) = 2957 m, 2907 m, 2870 m, 2151 w, 1613 s, 1570 s, 1535 s, 1491 vs, 1437 m, 1393 m, 1364 m, 1341 m, 1314 m, 1275 s, 1254s, 1188 m, 1157 m, 1092 w, 1061 w, 1026 w, 845 m, 818 w, 781 w, 750 w, 642 w, 608 w, 575 m, 550 m. Elemental analysis (%): calcd for [{(talen$^{t\text{-}Bu_2}$)-(Mn^{III}(MeOH))$_3$}$_2${Cr^{III}(CN)$_6$}](lac)$_3$·1.5MeOH (**3a**, C$_{160.5}$H$_{237}$N$_{18}$-O$_{28.5}$CrMn$_6$): C 59.20, H 7.34, N 7.74; found: C 58.80, H 7.04, N 8.14.

[{(talen$^{t\text{-}Bu_2}$)Mn$^{III}_3$}$_2${Cr^{III}(CN)$_6$}(solv)$_n$](BPh$_4$)$_3$. [{(talen$^{t\text{-}Bu_2}$)-Mn$^{III}_3$}$_2${Cr^{III}(CN)$_6$}(solv)$_n$](BPh$_4$)$_3$, which was subsequently recrystallized from different solvents, affording **4**, **5**, and **6**, was prepared as follows: A suspension of H$_6$talen$^{t\text{-}Bu_2}$ (150 mg, 0.135 mmol) and Mn(OAc)$_2$·4H$_2$O (93 mg, 0.38 mmol) in methanol (60 mL) was heated at reflux for 2 h. The resulting brown solution was cooled to room temperature, purged with air for 30 min, and heated at reflux for an additional 2 h. After cooling to room temperature, the reaction solution was treated with a solution of K$_3$[Cr(CN)$_6$] (22 mg, 0.068 mmol) in water (3 mL). The reaction mixture was stirred at room temperature for 60 min and filtered using filter paper for extremely fine precipitates (vide supra). A solution of NaBPh$_4$ (277 mg, 0.809 mmol) in methanol (30 mL) was added to the filtrate. The reaction mixture was stirred at room temperature for 10 min and filtered again, using filter paper for extremely fine precipitates (vide supra). Stirring of the filtrate for 16 h at room temperature resulted in the formation of a brown precipitate, which was collected by filtration and dried in vacuo. Yield: 227 mg.

[{(talen$^{t\text{-}Bu_2}$)Mn$^{III}_3$(MeCN)$_2$}$_2${Cr^{III}(CN)$_6$}]$_{0.5}$[{(talen$^{t\text{-}Bu_2}$)Mn$^{III}_3$(MeCN)-(H$_2$O)}$_2${Cr^{III}(CN)$_6$}]$_{0.5}$(BPh$_4$)$_3$·16MeCN (**4**). A suspension of [{(talen$^{t\text{-}Bu_2}$)Mn$^{III}_3$}$_2${Cr^{III}(CN)$_6$}(solv)$_n$](BPh$_4$)$_3$ (227 mg) in acetonitrile (25 mL) was heated at reflux for 1 min. The resulting brown solution was cooled to room temperature and filtered using filter paper for extremely fine precipitates (vide supra). Slow evaporation of the solvent from the filtrate afforded large brown crystals. Yield: 151 mg (53%). ESI-MS (MeCN): *m*/*z*: 916.3 [{(talen$^{t\text{-}Bu_2}$)Mn$_3$}$_2${Cr-(CN)$_6$}]$^{3+}$; MALDI-TOF-MS (matrix DCTB): *m*/*z*: 2748.3 [{(talen$^{t\text{-}Bu_2}$)Mn$_3$}$_2${Cr(CN)$_6$}]$^+$, 1373.5 [{(talen$^{t\text{-}Bu_2}$)Mn$_3$}$_2${Cr-(CN)$_6$}]$^{2+}$; IR (KBr): $\tilde{\nu}$ (cm^{-1}) = 3055 m, 3032 m, 2959 m, 2905 m, 2868 m, 2155 w, 1609 s, 1560 s, 1535 s, 1491 vs, 1437 m, 1393 m, 1364 m, 1341 m, 1310 m, 1275 s, 1252 s, 1188 m, 1155 m, 1063 w, 1026 w, 847 m, 820 w, 779 w, 750 w, 733 w, 704 m, 644 w, 611 w, 577 m, 554 m. Elemental analysis (%): calcd for [{(talen$^{t\text{-}Bu_2}$)-Mn$^{III}_3$(MeCN)$_2$}$_2${Cr^{III}(CN)$_6$}]$_{0.5}$[{(talen$^{t\text{-}Bu_2}$)Mn$^{III}_3$(MeCN)(H$_2$O)}$_2$-{Cr^{III}(CN)$_6$}]$_{0.5}$(BPh$_4$)$_3$·4MeCN (**4a**, C$_{230}$H$_{275}$N$_{25}$O$_{13}$B$_3$CrMn$_6$): C 68.86, H 6.91, N 8.73; found: C 68.93, H 6.92, N 8.70.

[{(talen$^{t\text{-}Bu_2}$)Mn$^{III}_3$(H$_2$O)((CH$_3$)$_2$CO)}$_2${Cr^{III}(CN)$_6$}]$_{0.5}$[{(talen$^{t\text{-}Bu_2}$)Mn$^{III}_3$-(H$_2$O)$_{0.18}$}$_2${Cr^{III}(CN)$_6$}]$_{0.5}$(BPh$_4$)$_3$·9.5(CH$_3$)$_2$CO (**5**). A suspension of [{(talen$^{t\text{-}Bu_2}$)Mn$^{III}_3$}$_2${Cr^{III}(CN)$_6$}(solv)$_n$](BPh$_4$)$_3$ (227 mg) in acetone (15 mL) was heated at reflux for 1 min. The resulting brown solution was cooled to room temperature and filtered using filter paper for extremely fine precipitates (vide supra). Slow evaporation of the solvent from the filtrate afforded large brown crystals. Yield: 144 mg (53%). ESI-MS (MeCN): *m*/*z*: 916.3 [{(talen$^{t\text{-}Bu_2}$)Mn$_3$}$_2${Cr-(CN)$_6$}]$^{3+}$; MALDI-TOF-MS (matrix DCTB): *m*/*z*: 2748.5 [{(talen$^{t\text{-}Bu_2}$)Mn$_3$}$_2${Cr(CN)$_6$}]$^+$, 1373.9 [{(talen$^{t\text{-}Bu_2}$)Mn$_3$}$_2${Cr-(CN)$_6$}]$^{2+}$; IR (KBr): $\tilde{\nu}$ (cm^{-1}) = 3055 m, 3034 m, 2961 m, 2905 m, 2868 m, 2155 w, 1611 s, 1560 s, 1535 s, 1491 vs, 1437 m, 1393 m, 1364 m, 1341 m, 1310 m, 1275 s, 1252 s, 1188 m, 1155 m, 1063 w, 1026 w, 847 m, 820 w, 779 w, 750 w, 733 w, 704 m, 644 w, 611 w, 577 m, 554 m. Elemental analysis (%): calcd for [{(talen$^{t\text{-}Bu_2}$)Mn$^{III}_3$-(H$_2$O)((CH$_3$)$_2$CO)}$_2${Cr^{III}(CN)$_6$}]$_{0.5}$[{(talen$^{t\text{-}Bu_2}$)Mn$^{III}_3$(H$_2$O)$_{0.18}$}$_2$-{Cr^{III}(CN)$_6$}]$_{0.5}$(BPh$_4$)$_3$·9(CH$_3$)$_2$CO (**5a**, C$_{246}$H$_{314.36}$N$_{18}$-O$_{23.18}$B$_3$CrMn$_6$): C 68.58, H 7.35, N 5.85; found: C 68.86, H 7.05, N 6.23.

[{(talen$^{t\text{-}Bu_2}$)Mn$^{III}_3$}$_2${Cr^{III}(CN)$_6$}(MeOH)$_3$(MeCN)$_2$]-(BPh$_4$)$_3$·4MeCN·2Et$_2$O (**6**). A suspension of [{(talen$^{t\text{-}Bu_2}$)-Mn$^{III}_3$}$_2${Cr^{III}(CN)$_6$}(solv)$_n$](BPh$_4$)$_3$ (227 mg) in acetonitrile (25 mL) was heated at reflux for 1 min. The resulting brown solution was cooled to room temperature and filtered using filter paper for

dx.doi.org/10.1021/ic301406j | Inorg. Chem. 2012, 51, 10929−10954

extremely fine precipitates (vide supra). Slow diffusion of diethyl ether into the filtrate afforded large brown crystals.[81] Yield: 194 mg (75%). Elemental analysis (%): calcd for $[\{(talen^{t\text{-}Bu_2})Mn^{III}_3\}_2\{Cr^{III}(CN)_6\}(MeOH)_3(MeCN)_2](BPh_4)_3\cdot 3MeCN\cdot Et_2O$ (**6a**, $C_{233}H_{289}N_{23}O_{16}B_3CrMn_6$): C 68.56, H 7.14, N 7.89; found: C 68.90, H 7.04, N 7.62.

X-ray Crystallography. Brown single crystals of **1**, **2**, **4**, and **5** were removed from the mother liquor, coated with paraffin oil, and immediately cooled to 183(2) K on a Bruker AXS SMART diffractometer (three-circle goniometer with 1 K CCD detector, Mo Kα radiation (λ = 0.71073 Å), graphite monochromator; sphere data collection in ω at 0.3° scan width in four runs with 606, 500, 606, and 500 frames (ϕ = 0°, 88°, 180°, and 268°); detector distance = 5 cm). A brown single crystal of **3** was measured at 100(2) K on a Nonius Kappa CCD diffractometer (four-circle goniometer, Mo Kα radiation, graphite monochromator, detector distance = 5 cm) using ω- and φ-scans. Empirical absorption corrections using equivalent reflections were performed with the program SADABS 2.10.[108] The structures were solved with the program SHELXS-97[109] and refined using SHELXL-97.[109] All hydrogen atoms were refined on calculated positions except some H positions for **3**, where one (O−)H atom could be located and refined at a coordinated MeOH molecule, one at an uncoordinated MeOH molecule, and one at the lactate −OH group. In **5**, one phenyl ring of a BPh_4^- anion is disordered over two positions. The higher-occupied arm (sof = 0.82) eliminates the coordinating H_2O molecule at one Mn atom, thus leading to the noninteger stoichiometry of the complex. Crystal data and further details concerning the crystal structure determination are given in Table S1 in the Supporting Information. CCDC 886620 (**1**), CCDC 886619 (**2**), CCDC 886622 (**3**), CCDC 886621 (**4**), and CCDC 886618 (**5**) from the Cambridge Crystallographic Data Centre contains the supplementary crystallographic data for this paper.

Other Physical Measurements. Infrared spectra (400−4000 cm^{-1}) of solid samples were recorded on a Shimadzu FT-IR 8400S system as KBr disks. ESI and MALDI-TOF mass spectra were recorded on a Bruker Esquire 3000 ion-trap mass spectrometer and a PE Biosystems Voyager DE mass spectrometer, respectively. Elemental analyses were carried out on a LECO CHN-932 or a HEKAtech Euro EA elemental analyzer. UV/vis/NIR absorption spectra of solutions were measured on a Shimadzu UV-3101PC spectrophotometer in the range of 190−1200 nm at ambient temperatures. The electrochemical experiments were performed on Ar-flushed MeCN solutions containing 0.1 M $[NBu_4]PF_6$ in a classical three-electrode cell. The working electrode was a glassy carbon disk electrode, the counter electrode was a platinum wire, and the reference electrode was Ag/0.01 M $AgNO_3$ MeCN. All potentials are referenced to the ferrocenium/ferrocene (Fc^+/Fc) couple used as an internal standard. The electrochemical cell was connected to an EG&G potentiostat/galvanostat (Model 273A). Temperature-dependent magnetic susceptibilities were measured by using a SQUID magnetometer (MPMS XL-7 EC, Quantum Design) in a static field of 0.01, 0.05, or 1 T in the temperature range of 2−290 K. Field-dependent magnetizations were measured at 2 K in the range of 0.2−7 T. Variable-temperature variable-field (VTVH) measurements were performed in various static fields (1−7 T) in the range of 2−10 K with the magnetization equidistantly sampled on an inverse temperature ($1/T$) scale. To calculate the molar magnetic susceptibilities (χ_m), the measured susceptibilities were corrected for the underlying diamagnetism of the sample holder and the sample, using tabulated Pascal's constants. AC susceptibilities were measured in the temperature range of 1.8−100 K in zero static field with an AC field of 3 Oe, oscillating at frequencies in the range of 0.1−1500 Hz.

Computational Details. *DFT Calculations.* Electronic structure calculations by the SIESTA method[110,111] have been performed using the generalized gradient approximation (GGA)[112,113] of the density functional theory (DFT). Norm-conserving pseudo-potentials were generated according to the Troullier−Martins scheme,[114] using the following electronic configurations and cutoff ("pseudoization") radii (in Bohr units, shown in brackets for each l-channel): Cr $4s^1$ (2.27) $3p^6$ (2.00) $3d^4$ (1.90) $4f^0$ (1.50); Mn $4s^1$ (2.00) $3p^6$ (1.90) $3d^5$ (1.90) $4f^0$ (1.50); C $2s^2$ $2p^2$ (all 1.25); N $2s^2$ $2p^3$ (all 1.25); O $2s^2$ $2p^4$ (all 1.15); H $1s^1$ (all 1.25). Basis functions were numerical, strictly confined, pseudo-atomic orbitals, generated in a standard way in SIESTA (see details in ref 115), with an "energy shift" parameter (which controls the confinement) of 20 mRy. The basis included polarization orbitals and triple-ζ functions for the 3d shells of Cr and Mn, being of double-ζ quality otherwise. An isolated molecule (409 atoms in total) with a 3+ charge was placed in a box 30 Å × 30 Å × 30 Å in size, to avoid an overlap of the basis functions with those of the translated replicas of the molecule. The Kohn−Sham energy levels, for the sake of necessary summations to be more smoothly done over them, were broadened with the "electronic temperature" parameter of 50 K. The real-space grid of 360^3 divisions along the edges of the simulation box corresponded to the "mesh cutoff" parameter of 400 Ry. The reference geometry, corresponding to a $Mn{-}N^{C\equiv N}$ distance of 2.185 Å, was taken from XRD data of **3** and not additionally relaxed. To study the effect of Mn−N distance variation, the two trinuclear Mn^{III} triplesalen building blocks of $[\mathbf{Mn^{III}_6Cr^{III}}]^{3+}$ were rigidly shifted along the molecular S_6 axis, keeping the $[Cr(CN)_6]^{3-}$ core unchanged.

Spin-Hamiltonian Simulations. The magnetic properties of $[\mathbf{Mn^{III}_6Cr^{III}}]^{3+}$ were simulated by a full-matrix diagonalization of the spin-Hamiltonian in eq 1:

$$\hat{H} = -2\sum_{i<j} J_{ij}\hat{\mathbf{S}}_i\cdot\hat{\mathbf{S}}_j + \sum_i D_i(\hat{\mathbf{S}}_i\cdot\mathbf{e}_i(\vartheta_i,\varphi_i))^2 + \mu_B\sum_i \mathbf{B}\cdot\underline{\underline{\mathbf{g}}}_i\cdot\hat{\mathbf{S}}_i \quad (1)$$

Here, the first sum reflects the isotropic exchange interaction between spins given by the spin vector operators $\hat{\mathbf{S}}_i$ at sites i. The anisotropic magnetization behavior of the individual ions is taken into account by local anisotropy tensors in the second sum. The tensors are parametrized by a strength factor $D_i = D$, as well as local unit vectors $\mathbf{e}_i$, which are parametrized by polar angles ϑ_i and φ_i. They represent an easy or a hard axis, depending on the sign of D. For the six Mn^{III} ions, the unit vectors point along the local Jahn−Teller axes. Because of the S_6 symmetry, all six local unit vectors $\mathbf{e}_i$ can be parametrized by the common polar angle between the Jahn−Teller axes and the S_6 symmetry axis, which has been extracted from crystal structures for each compound and is in the range of ϑ = 36.1°−39.1° (see Table 1). The relative φ_i angles are determined by the S_6 symmetry. The anisotropy axis of the Cr^{III} ion must point along the S_6 symmetry axis. The third term of the Hamiltonian models the interaction with the applied magnetic field. The term $\underline{\underline{\mathbf{g}}}_i$ represents the local g-matrix at site i. For the Mn^{III} ions, as well as the Cr^{III} ion, an isotropic value of 1.98 is assumed. The Hilbert space of the full spin-Hamiltonian has a dimension of 62 500. In the presence of a magnetic field, we employ inversion symmetry. This reduces the average matrix size to roughly half of the full size. Since the measurements are performed on ensembles of small crystallites, we also employ an orientational average using an isotropic grid with 20 orientations.[82,116]

RESULTS AND ANALYSIS

Synthesis and Characterization. In our attempt to investigate the influence of the molecular environment on the magnetic behavior of $[\mathbf{Mn^{III}_6Cr^{III}}]^{3+}$, we employed different anions and solvents of crystallization with the aim of obtaining different salts and solvates of $[\mathbf{Mn^{III}_6Cr^{III}}]^{3+}$. In analogy to the preparation of $[\mathbf{Mn^{III}_6Fe^{III}}][Fe^{III}(CN)_6]$,[82] we tried to synthesize $[\mathbf{Mn^{III}_6Cr^{III}}][Cr^{III}(CN)_6]$. The molecular building block $[(talen^{t\text{-}Bu_2})\{Mn^{III}(solv)_n\}_3]^{3+}$ was generated in situ by reacting the ligand $H_6talen^{t\text{-}Bu_2}$ with 3 equiv of $Mn^{II}(OAc)_2\cdot 4H_2O$ in methanol. The subsequent addition of 2 equiv of $K_3[Cr^{III}(CN)_6]$ in a minimal amount of water, followed by slow evaporation of the solvent, led to the formation of brown crystals. Visual inspection indicated the contamination with some fine colorless precipitate and the presence of crystals with different morphologies. While the

Table 1. Selected Structural Parameters of Compounds 1−6

	1	2	3	4	5	6
$\angle(C_3^{(1)},C_3^{(2)})^a$ [°]	81.8	77.5	0.0	68.9	2.2	41.7
shortest Cr···Cr distance [Å]	18.28	17.89	15.89	18.05	19.12	18.52
shortest intermolecular Mn···Mn distance [Å]	8.36	9.03	8.79	9.82	11.47	8.90
fraction(s) of $[\mathbf{Mn^{III}_6Cr^{III}}]^{3+}$ in the asymmetric unit	1/2	1/2	2 × 1/6	2 × 1/2	2 × 1/2	1
coordination number of Mn^{III}	6	5 or 6	6	5 or 6	5 or 6	5 or 6
$d(Mn-N^{C\equiv N})^b$ [Å]	2.21	2.22	2.19	2.19	2.17	2.18
$d(Cr-C)^b$ [Å]	2.08	2.09	2.06	2.08	2.07	2.07
$d(C\equiv N)^b$ [Å]	1.15	1.15	1.15	1.15	1.15	1.15
$\angle(Cr-C\equiv N)^b$ [°]	176.6	175.9	179.0	176.6	175.7	176.1
$\angle(C\equiv N-Mn)^b$ [°]	161.3	161.9	159.4	159.9	161.3	161.3
$\angle(C-Cr-C)^b$ [°]	89.2	88.5	91.4	89.0	88.5	88.7
$\varphi^{terminal}$ [°]^b	7.5	8.3	10.5	9.1	10.1	8.5
$\varphi^{central}$ [°]^b	43.4	44.5	34.6	46.1	48.0	46.7
θ [°]^b	1.8	1.0	8.5	0.9	1.7	1.3
ϑ [°]^b	38.7	39.1	36.1	38.9	38.7	39.0

^{a}Angle between the (approximate) molecular C_3 axes of the $[\mathbf{Mn^{III}_6Cr^{III}}]^{3+}$ complexes in the crystal. ^{b}Mean values.

majority of crystals are best described as columns, some rhombs were also found as a minor component, with both crystallizing in the space group $C2/c$. Single-crystal XRD analysis of the major species resulted in the formulation as $[\{(talen^{t\text{-}Bu_2})(Mn^{III}(MeOH))_3\}_2\{Cr^{III}(CN)_6\}][Cr^{III}(CN)_6]\cdot 14MeOH\cdot 5H_2O$ (**1**) with separated $[\mathbf{Mn^{III}_6Cr^{III}}]^{3+}$ cations and $[Cr^{III}(CN)_6]^{3-}$ anions, whereas the minor component analyzed as $[\{(talen^{t\text{-}Bu_2})Mn^{III}{}_3(MeOH)(H_2O)\}_2\{Cr^{III}(CN)_6\}](\mu_2\text{-}[Cr^{III}(CN)_6])\cdot 9MeOH\cdot 2H_2O$ (**2**) with $[\mathbf{Mn^{III}_6Cr^{III}}]^{3+}$ bridged by μ_2-$[Cr^{III}(CN)_6]^{3-}$ resulting in a one-dimensional (1D) chain.

After several optimization steps, we found experimental conditions under which only crystals of compound **1** were obtained. However, visual inspection of these batches revealed that they were still contaminated with some fine colorless precipitate. Temperature-dependent magnetic susceptibility measurements (2−290 K, 0.01 T) on powdered samples of these batches showed an onset of the magnetization at ∼65 K, indicative of magnetic ordering. The lack of reproducibility of both the ordering temperature, which varied between 60 K and 70 K, and the susceptibility maximum, which was more or less pronounced for different batches, led to the assumption that magnetic impurities accounted for the ordering phenomenon. Several examples of Cr^{III}−Mn^{II} Prussian blue-type ferrimagnets exhibiting magnetic ordering in the observed temperature range are known in the literature. Ordering temperatures between 60 K and 74 K were reported for the three-dimensional (3D) Prussian blue analogue $Mn^{II}{}_3[Cr^{III}(CN)_6]_2\cdot xH_2O$.[117−120] The Curie temperature of 3D Prussian blue-type systems of the composition $M^I[Mn^{II}Cr^{III}(CN)_6]\cdot xH_2O$ varies from 60 K (M = Na)[121] to 90 K (M = Cs),[122] revealing a strong dependence of the magnetic ordering on the choice of alkali-metal counterion. Furthermore, cyanide-bridged Cr^{III}−Mn^{II} assemblies of different dimensionality, incorporating bidentate organic ligands, exhibit spontaneous magnetization with T_c varying between 60 K and 71 K.[119,123] Assuming the presence of some unreacted Mn^{II} in solutions containing $[(talen^{t\text{-}Bu_2})\{Mn^{III}(solv)_n\}_3]^{3+}$ during the synthesis of **1**, the addition of $K_3[Cr^{III}(CN)_6]$ may result in the formation of $Mn^{II}{}_3[Cr^{III}(CN)_6]_2\cdot xH_2O$ or $K^I[Mn^{II}Cr^{III}(CN)_6]\cdot xH_2O$, the ratio and total amount of which may differ for distinct batches, leading to the observed variations in the ordering temperature and the susceptibility maximum, respectively. In order to corroborate this supposition, we reacted $K_3[Cr^{III}(CN)_6]$ with 1.5 equiv of $Mn^{II}(OAc)_2\cdot 4H_2O$ in a methanol−water mixture, thus mimicking the reaction conditions for the synthesis of **1** without the ligand $H_6talen^{t\text{-}Bu_2}$ being present. We observed the precipitation of a fine colorless powder which, by visual inspection, closely resembled the precipitate formed during the synthesis of **1**. Temperature-dependent magnetic susceptibility measurements on the powder showed an onset of the magnetization at 70 K, which supported our assumption that contaminations from Cr^{III}−Mn^{II} Prussian blue-type ferrimagnets were the cause of the magnetic ordering observed in batches of **1**.

We have modified the reaction conditions for the synthesis of **1** in order to avoid Prussian blue analogues. Since these 3D ferrimagnets are highly insoluble, one of our aims was to induce their precipitation before $[\mathbf{Mn^{III}_6Cr^{III}}][Cr^{III}(CN)_6]$ begins to crystallize. Therefore, we added more than 2 equiv of $K_3[Cr^{III}(CN)_6]$ to solutions containing $[(talen^{t\text{-}Bu_2})\{Mn^{III}(solv)_n\}_3]^{3+}$, which unfortunately resulted in the precipitation of $[\mathbf{Mn^{III}_6Cr^{III}}][Cr^{III}(CN)_6]$ as a brown powder, along with the Prussian blue analogues. In another effort to optimize the reaction conditions, we employed the precursor $[(talen^{t\text{-}Bu_2})\{Mn^{III}(solv)_n\}_3]Cl_3$ in analogy to the early syntheses of $[\mathbf{Mn^{III}_6Fe^{III}}][Fe^{III}(CN)_6]$,[82] with the aim of avoiding the presence of unreacted Mn^{II} in solution upon the addition of $K_3[Cr^{III}(CN)_6]$. However, this procedure did not prove successful either, as we still detected the Prussian blue analogues by magnetic measurements. A pure batch of **1** was finally obtained by the combination of two means: (1) reducing the amount of unreacted Mn^{II} in solutions containing $[(talen^{t\text{-}Bu_2})\{Mn^{III}(solv)_n\}_3]^{3+}$ by (i) employing less than 3 equiv of $Mn^{II}(OAc)_2\cdot 4H_2O$ and (ii) heating the reaction solution at reflux for a longer time and purging it with air to facilitate the oxidation of Mn^{II} and thus the formation of $[(talen^{t\text{-}Bu_2})\{Mn^{III}(solv)_n\}_3]^{3+}$; and (2) extensive filtration of the reaction solution after addition of $K_3[Cr^{III}(CN)_6]$.

In our attempts to establish a protocol leading to pure batches of **2**, we found that the presence of other anions, such as lactate, favors the formation of this compound. Despite much effort, however, we were not able to obtain **2** in an analytically pure form. Contaminations from crystals of **1** were always detected by single-crystal XRD, and the precipitation of the above-mentioned Prussian blue analogues could not be completely avoided, even by the optimized procedure previously described. Recrystallization of mixtures of **1** and **2** was

dx.doi.org/10.1021/ic301406j | Inorg. Chem. 2012, 51, 10929−10954

not possible, because of the low solubility of these compounds, as well as the sensitivity of the **1**:**2** ratio to the concentration of other components, especially anionic species, in solution. Thus, we had to refrain from a complete characterization of compound **2**.

The $[\mathbf{Mn^{III}_6Cr^{III}}][Cr^{III}(CN)_6]$ compounds **1** and **2** as well as the previously published[81] $[\mathbf{Mn^{III}_6Cr^{III}}](BPh_4)_3$ compound crystallize in monoclinic space groups with a noncollinear arrangement of the $[\mathbf{Mn^{III}_6Cr^{III}}]^{3+}$ units in the crystal structure (vide infra). This entails two drawbacks for the SMM behavior: (i) The molecular structure is not rigorously C_3 symmetric, as no crystallographic C_3-axis (not existing in monoclinic space groups) goes through the molecule; and (ii) the low symmetry of the molecular environment further reduces the symmetry of the individual complexes, especially by stray fields originating from neighboring high-spin molecules.

In order to align the C_3-axes of the $[\mathbf{Mn^{III}_6Cr^{III}}]^{3+}$ molecules in the crystal, we have employed the rod-shaped anion lactate (= lac) to obtain $[\mathbf{Mn^{III}_6Cr^{III}}](lac)_3$. This was inspired by the frequent occurrence of hexagonal and cubic packings in systems with rod-shaped components.[124−140] Recrystallization from methanol afforded pure batches of single crystals, which analyzed as $[\{(talen^{t\text{-}Bu_2})(Mn^{III}(MeOH))_3\}_2\{Cr^{III}(CN)_6\}](lac)_3\cdot 9MeOH$ (**3**) crystallizing in the trigonal space group $R\bar{3}$ with the molecular S_6-axes of the $[\mathbf{Mn^{III}_6Cr^{III}}]^{3+}$ complexes all aligned with the *c*-axis of the unit cell (vide infra).

In the course of our efforts to obtain pure batches of compounds **1**−**3**, the synthesis of the already published complex $[\mathbf{Mn^{III}_6Cr^{III}}](BPh_4)_3$[81] was also optimized according to the new protocol. However, it has to be emphasized that recrystallization of $[\mathbf{Mn^{III}_6Cr^{III}}](BPh_4)_3$ from acetonitrile/diethyl ether had sufficed to obtain pure batches of $[\{(talen^{t\text{-}Bu_2})Mn^{III}_3\}_2\{Cr^{III}(CN)_6\}(MeOH)_3(MeCN)_2](BPh_4)_3\cdot 4MeCN\cdot 2Et_2O$ (**6**) before the optimized procedure was established.[81] The good solubility of $[\mathbf{Mn^{III}_6Cr^{III}}](BPh_4)_3$ in a variety of solvents allowed not only its purification by recrystallization, but also the synthesis of new solvates. Thus, crystals of $[\{(talen^{t\text{-}Bu_2})Mn^{III}_3(MeCN)_2\}_2\{Cr^{III}(CN)_6\}]_{0.5}[\{(talen^{t\text{-}Bu_2})Mn^{III}_3(MeCN)(H_2O)\}_2\{Cr^{III}(CN)_6\}]_{0.5}(BPh_4)_3\cdot 16MeCN$ (**4**) were obtained by recrystallizing $[\mathbf{Mn^{III}_6Cr^{III}}](BPh_4)_3$ from acetonitrile, whereas recrystallization from acetone afforded crystals of $[\{(talen^{t\text{-}Bu_2})Mn^{III}_3(H_2O)((CH_3)_2CO)\}_2\{Cr^{III}(CN)_6\}]_{0.5}[\{(talen^{t\text{-}Bu_2})Mn^{III}_3(H_2O)_{0.18}\}_2\{Cr^{III}(CN)_6\}]_{0.5}(BPh_4)_3\cdot 9.5(CH_3)_2CO$ (**5**).

Newly synthesized batches of $[\mathbf{Mn^{III}_6Cr^{III}}]^{3+}$ compounds were tested for the presence of Prussian blue analogues by temperature-dependent magnetic susceptibility measurements (2−290 K, 0.01 T), since the impurity could neither be identified by elemental analysis nor by FT-IR spectroscopy (vide infra) and was detected by visual inspection only if it appeared in sufficient quantity.

FT-IR spectra of compounds **1**−**6** exhibit the characteristic features of the $[(talen^{t\text{-}Bu_2})Mn^{III}_3]^{3+}$ building block, as found in several other complexes,[82,83,85,141] with prominent bands at 1609, 1560, 1535, and 1491 cm^{-1}. Besides these, the spectra exhibit distinct bands confirming the presence of the different counterions of $[\mathbf{Mn^{III}_6Cr^{III}}]^{3+}$, with the spectra of the three solvates of $[\mathbf{Mn^{III}_6Cr^{III}}](BPh_4)_3$ (**4**−**6**) being superimposable. The symmetric $\nu(C{\equiv}N)$ vibration of the bridging $[Cr^{III}(CN)_6]^{3-}$ unit is detected at 2147, 2151, and 2155 cm^{-1} in spectra of **1**, **3**, and **4**−**6**, respectively, with **3** exhibiting a broader band than the other compounds. The shift to higher energies compared to $K_3[Cr^{III}(CN)_6]$, which shows a band at 2131 cm^{-1} attributed to the symmetric $\nu(C{\equiv}N)$ vibration, is consistent with the symmetric bridging mode of the central hexacyanometallate as found in other $[\mathbf{M^t_6M^c}]^{n+}$ complexes.[82,83] The batch of Prussian blue analogues synthesized for purposes of comparison (vide supra) exhibits a strong band at 2160 cm^{-1}. We tried to associate the presence of Prussian blue analogues detected by magnetic measurements on early $[\mathbf{Mn^{III}_6Cr^{III}}]^{3+}$ batches with the appearance of a shoulder on the higher energy side of the $\nu(C{\equiv}N)$ feature of the $[\mathbf{Mn^{III}_6Cr^{III}}]^{3+}$ trication, but failed to do so, which indicates that the amount of impurity, although strongly affecting the magnetic characteristics of these batches and sometimes visually discernible, was only marginal. The symmetric $\nu(C{\equiv}N)$ vibration of the ionic $[Cr^{III}(CN)_6]^{3-}$ counterion in compound **1** is detected at 2126 cm^{-1}, thus occurring within the wavenumber range of 2110−2131 cm^{-1} found for a series of $[Cr^{III}(CN)_6]^{3-}$ salts, i.e. $(NBu_4)_3[Cr^{III}(CN)_6]$ and $(NEt_4)_3[Cr^{III}(CN)_6]$, which we synthesized according to literature procedures,[142,143] and the already mentioned $K_3[Cr^{III}(CN)_6]$.

ESI mass spectra of compounds **1** and **3**−**6** exhibit a prominent ion at a mass-to-charge-ratio *m*/*z* of 916 with mass and isotope distribution pattern corresponding to the trication $[\{(talen^{t\text{-}Bu_2})Mn_3\}_2\{Cr(CN)_6\}]^{3+}$. In addition, the dication $[\{(talen^{t\text{-}Bu_2})Mn_3\}_2\{Cr(CN)_6\}]^{2+}$ is detected at a mass-to-charge ratio *m*/*z* of 1375 in the spectrum of **6**.[81] MALDI-TOF mass spectra of compounds **1** and **3**−**6** exhibit a pronounced signal with mass and isotope distribution pattern corresponding to the monocation $[\{(talen^{t\text{-}Bu_2})Mn_3\}_2\{Cr(CN)_6\}]^{+}$ (*m*/*z* = 2748). Compounds **4** and **5** additionally show a weak signal corresponding to the dication $[\{(talen^{t\text{-}Bu_2})Mn_3\}_2\{Cr(CN)_6\}]^{2+}$. As evident from these data, none of the Mn^{III} ions carries a solvent molecule at its sixth coordination site in the mass spectra, irrespective of the nature of the solvent molecules coordinating to the Mn^{III} ions in crystals of compounds **1** and **3**−**6** (vide infra). This finding demonstrates the weakness of the $Mn{-}X^{solv}$ bond, which was also observed in other complexes[82,83,144] and is corroborated by an analysis of the respective bond lengths (vide infra).

Crystal and Molecular Structures. Compounds **1** and **2** crystallize in the space group *C*2/*c* with significant differences relating to the assembly of the $[\mathbf{Mn^{III}_6Cr^{III}}]^{3+}$ and $[Cr^{III}(CN)_6]^{3-}$ units in their crystal structures. While in crystals of **1**, these components only interact via hydrogen bonding between two N atoms of each ionic $[Cr^{III}(CN)_6]^{3-}$ and two hydroxyl groups of methanol molecules coordinated to Mn^{III} in adjacent $[\mathbf{Mn^{III}_6Cr^{III}}]^{3+}$ complexes with $d(O^{MeOH}\cdots N^{C{\equiv}N})$ = 2.89 Å, which results in quasi-1D chains (Figure 1a), the $[\mathbf{Mn^{III}_6Cr^{III}}]^{3+}$ and $[Cr^{III}(CN)_6]^{3-}$ units in crystals of **2** are covalently linked through $Mn{-}N^{C{\equiv}N}$ bonds, thus forming true 1D chains (Figure 1b). The quasi-1D chains in crystals of **1** run in the two directions defined by the *ab* diagonals of the unit cell (see Figure S1a in the Supporting Information), whereas the 1D chains in crystals of **2** all propagate parallel to the $\vec{a}+\vec{c}$ diagonal (see Figure S1b in the Supporting Information). The compound $[\mathbf{Mn^{III}_6Fe^{III}}][Fe^{III}(CN)_6]$ exhibits a quasi-1D chain structure analogous to that of **1**.[82]

The $[\mathbf{Mn^{III}_6Cr^{III}}](lac)_3$ compound **3** crystallizes in the trigonal space group $R\bar{3}$. This has important consequences for the relative arrangement of the $[\mathbf{Mn^{III}_6Cr^{III}}]^{3+}$ complexes in the crystal structure: (i) The molecular S_6 axes are all aligned with the *c*-axis of the unit cell (see Figure 2 and Figure S2 in the Supporting Information); and (ii) the environment of each $[\mathbf{Mn^{III}_6Cr^{III}}]^{3+}$ complex in the crystal structure is highly

dx.doi.org/10.1021/ic301406j | Inorg. Chem. 2012, 51, 10929−10954

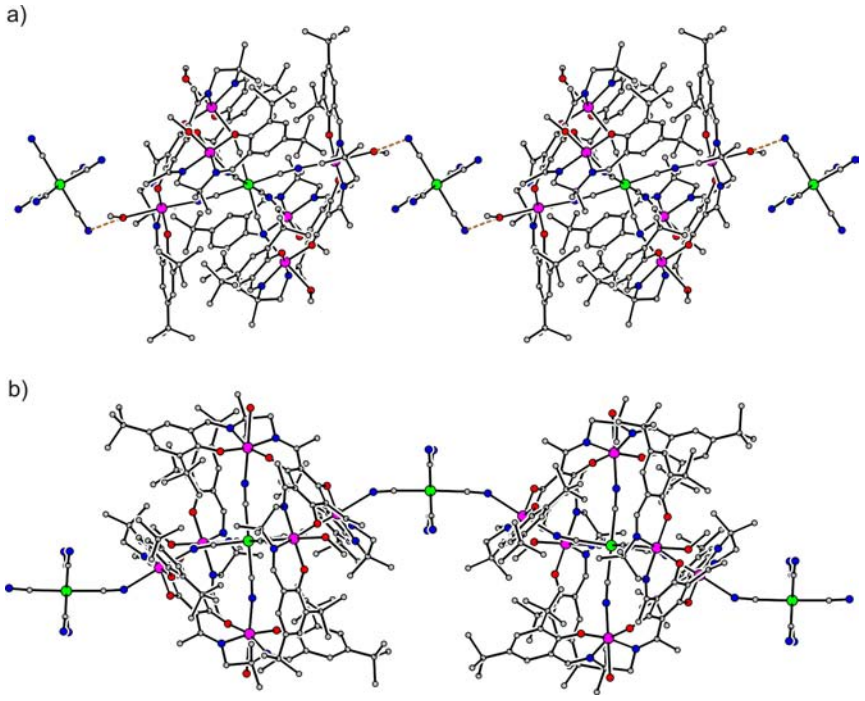

Figure 1. One-dimensional (1D) chain motifs in crystals of (a) **1** and (b) **2**. Crystals of **1** contain quasi-1D chains formed by hydrogen bonding (dashed lines) between the $[Cr^{III}(CN)_6]^{3-}$ trianions and the hydroxyl groups of methanol molecules coordinated to Mn^{III} in neighboring $[\mathbf{Mn^{III}_6Cr^{III}}]^{3+}$ trications. In contrast, the $[\mathbf{Mn^{III}_6Cr^{III}}]^{3+}$ and $[Cr^{III}(CN)_6]^{3-}$ units are covalently linked through $Mn-N^{C\equiv N}$ bonds in crystals of **2**, which results in true 1D chains. Note that the angle between the approximate molecular C_3 axes of adjacent $[\mathbf{Mn^{III}_6Cr^{III}}]^{3+}$ units within a chain is 0° in crystals of **1** and 77.5° in crystals of **2**.

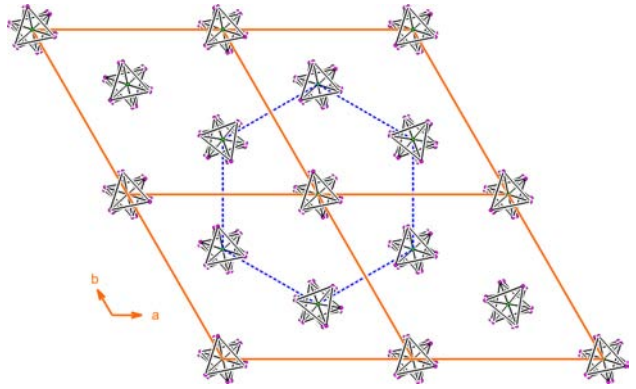

Figure 2. Section of the crystal structure of **3** with the viewing direction parallel to the *c*-axis of the unit cell. The $[\mathbf{Mn^{III}_6Cr^{III}}]^{3+}$ complexes are simplified to connected Cr and Mn atoms. Note that the molecular S_6 axes of the $[\mathbf{Mn^{III}_6Cr^{III}}]^{3+}$ complexes are all parallel to the *c*-axis. The dashed lines highlight the symmetric environment of the molecules enforced by the crystal structure.

symmetric. In contrast, the series of $[\mathbf{Mn^{III}_6Cr^{III}}](BPh_4)_3$ solvates **4**–**6** exhibits noncollinearly arranged $[\mathbf{Mn^{III}_6Cr^{III}}]^{3+}$ complexes in the crystal structures, with **4** and **5** crystallizing in the space group $P\bar{1}$ and **6** in $P2_1$.[81]

The angles between the approximate molecular C_3-axes of the $[\mathbf{Mn^{III}_6Cr^{III}}]^{3+}$ complexes in crystals of **1**–**6**, as well as the separation of the individual complexes in the crystal structures, as evidenced by the shortest intermolecular Cr···Cr and Mn···Mn distances, are summarized in Table 1. There is a rather strong variation in the shortest intermolecular Mn···Mn distances of **4**–**6**, which reflects the different relative orientations of the $[\mathbf{Mn^{III}_6Cr^{III}}]^{3+}$ complexes as the Cr···Cr distance between their centroids remains almost unchanged. Most notable with respect to the separation of the individual molecules within the entire series of $[\mathbf{Mn^{III}_6Cr^{III}}]^{3+}$ compounds **1**–**6** is the significantly shorter Cr···Cr distance in **3** compared to the other compounds, which is obviously related to the high crystal symmetry.

The crystallographically imposed symmetry varies significantly for the $[\mathbf{Mn^{III}_6Cr^{III}}]^{3+}$ trications in **1**–**6**, because of differences in the composition of the asymmetric unit. In the case of **1** and **2**, the asymmetric unit contains half of the $[\mathbf{Mn^{III}_6Cr^{III}}]^{3+}$ molecule, with the other half being generated by a crystallographic center of inversion located at the central chromium ion. In contrast, the asymmetric unit in crystals of **3** consists of two independent metal-containing entities, each forming a sixth of a $[\mathbf{Mn^{III}_6Cr^{III}}]^{3+}$ complex. Thus, these molecules possess a crystallographically imposed S_6 symmetry, which distinguishes compound **3** from all the other $[\mathbf{Mn^{III}_6Cr^{III}}]^{3+}$ compounds. The asymmetric unit in crystals of **4** and **5** consists of two independent halves of $[\mathbf{Mn^{III}_6Cr^{III}}]^{3+}$ complexes, with the other half being generated by a crystallographic center of inversion located at the central chromium ion. On the other hand, crystals of **6** contain the entire $[\mathbf{Mn^{III}_6Cr^{III}}]^{3+}$ molecule in their asymmetric unit,[81] which implies that the $[\mathbf{Mn^{III}_6Cr^{III}}]^{3+}$ complex does not possess a crystallographically imposed symmetry in this compound.

The molecular structures of the $[\mathbf{Mn^{III}_6Cr^{III}}]^{3+}$ trications in compounds **1**–**6** consist of two trinuclear Mn^{III} triplesalen building blocks connected by a hexacyanochromate (Figure 1). Thermal ellipsoid plots of the metal-containing entities in the asymmetric units in crystals of **1**–**5** are depicted in Figures S3–S7 in the Supporting Information, and selected bond distances and angles are summarized in Tables S2–S6 in the Supporting Information. The Mn^{III} ions are in a Jahn–Teller distorted tetragonal environment. Each Mn^{III} is coordinated by an N_2O_2

dx.doi.org/10.1021/ic301406j | *Inorg. Chem.* 2012, 51, 10929–10954

compartment of the ligand and a N atom of the bridging hexacyanochromate, while the sixth position varies. In **1** and **3**, all Mn^{III} ions are coordinated by a methanol molecule, whereas the $[\mathbf{Mn^{III}_6Cr^{III}}]^{3+}$ entities in **2** and **4**–**6** carry different types of molecules at their Mn^{III} sixth coordination sites, in addition to exhibiting some vacant sites.

Table 1 provides mean values of selected structural parameters of **1**–**6** that appear important for the discussion. The Mn^{III} Jahn–Teller axis is along the $N^{C\equiv N}\cdots X^{solv/C\equiv N}$ direction, as evidenced by longer mean $Mn-N^{C\equiv N}$ and $Mn\text{-}X^{solv/C\equiv N}$ bond distances of 2.19 Å and 2.44 Å, respectively, compared to $Mn-O^{Ph}$ (1.88 Å) and $Mn-N^{imine}$ (1.98 Å). While the spread in the values of the $Mn-O^{Ph}$ and $Mn-N^{imine}$ bond distances does not exceed 0.04 Å, there is a significantly larger spread in the individual $Mn-N^{C\equiv N}$ and $Mn-X^{solv/C\equiv N}$ bond lengths of 0.13 Å and 0.48 Å, respectively. The mean value and the broad distribution of the $Mn-X^{solv/C\equiv N}$ bond distances are in accordance with a merely weak bonding of the donor atoms at the Mn^{III} sixth coordination sites, as evidenced by the absence of coordinated solvent molecules in the mass spectra of **1** and **3**–**6** (vide supra). The relative shortness of the $Mn-N^{C\equiv N}$ bond (mean value of 2.19 Å) compared to other $Cr^{III}(CN)_n\text{-}C\equiv N\text{-}Mn(salen)$ systems,[85] including the $Cr-C\equiv N-Mn$ unit linking different $[\mathbf{Mn^{III}_6Cr^{III}}]^{3+}$ entities in compound **2** ($d(Mn-N^{C\equiv N})$ = 2.38 Å), is a distinctive feature of $[\mathbf{Mn^{III}_6Cr^{III}}]^{3+}$. A comparison of the $Mn-N^{C\equiv N}$ bond distances within $[\mathbf{Mn^{III}_6Cr^{III}}]^{3+}$ for Mn^{III} ions with occupied and unoccupied sixth coordination sites reveals a correlation between the state of occupancy and the $Mn-N^{C\equiv N}$ bond length. If only the Mn^{III} ions with vacant sixth coordination sites are considered, the mean $Mn-N^{C\equiv N}$ bond distance reduces to 2.13 Å with a spread of only 0.03 Å in the individual values. In contrast, the six-coordinate Mn^{III} ions exhibit a mean $Mn-N^{C\equiv N}$ bond length of 2.20 Å within $[\mathbf{Mn^{III}_6Cr^{III}}]^{3+}$ with a spread of 0.08 Å in the individual values.

An important aspect regarding the Cr–Mn exchange interaction is the exact structure of the $Cr-C\equiv N-Mn$ pathway. The ionic $[Cr^{III}(CN)_6]^{3-}$ in **1** and **2** may be used as an internal reference for comparison with the bridging $[Cr^{III}(CN)_6]^{3-}$ unit in the $[\mathbf{Mn^{III}_6Cr^{III}}]^{3+}$ complexes, so its mean values are provided in parentheses. The mean Cr–C and C≡N bond distances within the $[\mathbf{Mn^{III}_6Cr^{III}}]^{3+}$ complexes in **1**–**6** are 2.07 Å (2.06 Å) and 1.15 Å (1.16 Å), respectively, while the mean $Cr-C\equiv N$ angle is 176.8° (176.8°) with a spread of 4.9° (2.6°) in the individual values. Thus, the coordination of the cyanide N atoms to Mn^{III} does not introduce severe strain to the bridging $[Cr^{III}(CN)_6]^{3-}$, because the Cr–C≡N units do not exhibit significant structural changes. On the other hand, a nonlinearity is observed for the $C\equiv N-Mn$ angles. Their mean value within in the $[\mathbf{Mn^{III}_6Cr^{III}}]^{3+}$ complexes in **1**–**6** is 160.7° with a spread of 6.6°, while the $C\equiv N-Mn$ angle within the $Cr-C\equiv N-Mn$ unit linking different $[\mathbf{Mn^{III}_6Cr^{III}}]^{3+}$ entities in **2** has a significantly smaller value of 150.6°. The observed bending is common for the $Cr(CN)_n-C\equiv N-Mn$ unit. A search in the Cambridge Structural Database provided 53 individual units with a mean value of 160.4° for the $C\equiv N-Mn$ angles, the large spread of 41.3° indicating a flat potential for bending.[85]

The bending does not occur randomly, but all six $C\equiv N-Mn$ units bend toward the molecular C_3-axis. This has an important impact on the relative arrangement of the six Mn^{III} ions surrounding the central Cr^{III} ion. In the hypothetical limit of linear $C\equiv N-Mn$ angles, the six Mn^{III} ions would form an octahedral (i.e., cubic) arrangement around the central Cr^{III} ion. The concerted bending of the $C\equiv N-Mn$ units leads to a symmetry reduction from approximately O_h to approximately C_3. This symmetry reduction is also evident in the Mn···Mn distances, which are shorter for the Mn^{III} ions of the same trinuclear triplesalen building block (6.73 Å) than for Mn^{III} ions belonging to different trinuclear triplesalen building blocks (8.25 Å). The mean Mn···Mn distances in **3** are 6.85 Å and 8.15 Å and deviate from those in the other compounds, ranging from 6.63 Å to 6.77 Å and from 8.24 Å to 8.37 Å, respectively. This difference correlates with a different distortion of the central $[Cr^{III}(CN)_6]^{3-}$ unit. The octahedron of the central Cr^{III} ion in **3** is slightly compressed along the molecular C_3-axis, as evidenced by a mean C–Cr–C angle of 91.4° within one half of the $[\mathbf{Mn^{III}_6Cr^{III}}]^{3+}$ complex. In contrast, the octahedron of the central Cr^{III} ion in the other $[\mathbf{Mn^{III}_6Cr^{III}}]^{3+}$ compounds is slightly elongated along the approximate molecular C_3-axis, the mean C–Cr–C angle within one half of the complex being 88.8°.

An important consideration for the Mn–Mn exchange interaction is the exact structure of the trinuclear triplesalen building block. We have applied several parameters for a quantitative description of the ligand folding in the study of the trinuclear triplesalen complexes.[74,77] It turned out that the best parameters to quantitatively describe the ligand folding are the bent angles $\varphi^{central}$ and $\varphi^{terminal}$. The bent angle φ (introduced by Cavallo and Jacobsen)[145] is defined by $\varphi = 180° - \angle(M-X_{NO}-X_R)$ (X_{NO} represents the midpoint of adjacent N and O donor atoms; X_R represents the midpoint of the six-membered chelate ring containing the N and O donor atoms). In the trinuclear Ni^{II} and Cu^{II} complexes, $\varphi^{central}$ is in the range of 20°–30° while $\varphi^{terminal}$ is significantly smaller in the range of 3°–9°.[74,77] Coordination of a hexacyanometallate should obviously increase the ligand folding. While the $\varphi^{terminal}$ value of the $[\mathbf{Mn^{III}_6Cr^{III}}]^{3+}$ compounds (Table 1) is still small with 9.3° (spread 10.7°), there is a significant increase in $\varphi^{central}$ when going from the trinuclear to the heptanuclear complexes. However, this increase is not equally pronounced for the different $[\mathbf{Mn^{III}_6Cr^{III}}]^{3+}$ compounds, with **3** differing yet again from the other compounds by exhibiting a mean bent angle at the central phenolates of $\varphi^{central}$ = 34.6° (spread 1.3°), compared to a mean $\varphi^{central}$ value of 46.1° (spread 12.3°) in the other compounds. The value for **3** is similar to those found for $[\mathbf{Mn^{III}_6Fe^{III}}]^{3+}$ (36.0°)[82] and $[\mathbf{Mn^{III}_6Co^{III}}]^{3+}$ (38.1°).[83] Upon comparison of $[\mathbf{Mn^{III}_6Fe^{III}}]^{3+}$, $[\mathbf{Mn^{III}_6Co^{III}}]^{3+}$, and **6**, we have identified a correlation between $\varphi^{central}$ and the angle θ between the benzene plane of the central phloroglucinol and the vector formed by the central phenolate O atom and the central ketimine N atom (see Figure S8a in the Supporting Information).[82,83] The angle θ, which is a measure for the helical distortion in the heptanuclear complexes, has a mean value of 11.7° in $[\mathbf{Mn^{III}_6Fe^{III}}]^{3+}$,[82] 9.0° in $[\mathbf{Mn^{III}_6Co^{III}}]^{3+}$,[83] 8.5° (spread 1.6°) in **3**, and only 1.3° (spread 3.3°) in the other $[\mathbf{Mn^{III}_6Cr^{III}}]^{3+}$ compounds. The stronger helical distortion in **3**, compared to the other $[\mathbf{Mn^{III}_6Cr^{III}}]^{3+}$ compounds comes along with a slighter distortion of the central phloroglucinol ring and its six direct substituents. In the case of **3**, these 12 atoms are all in an idealized plane, whereas in the other $[\mathbf{Mn^{III}_6Cr^{III}}]^{3+}$ compounds, the 3 O atoms lie below the plane and the three ketimine C atoms lie above the plane (see Figure S8a in the Supporting Information).

The series of $[\mathbf{Mn^{III}_6Cr^{III}}]^{3+}$ compounds nicely illustrates that the degree of folding of the triplesalen ligand is not

dx.doi.org/10.1021/ic301406j | Inorg. Chem. 2012, 51, 10929–10954

determined by the size of the hexacyanometallate unit, as **3** and the other $[\mathbf{Mn^{III}_6Cr^{III}}]^{3+}$ compounds all exhibit similar Cr−C distances. However, there seems to be a correlation between $\varphi^{central}$, θ, and the trigonal distortion of the octahedron spanned by the cyanide C atoms around the central metal ion. While the stronger helical distortion in $[\mathbf{Mn^{III}_6Fe^{III}}]^{3+}$, $[\mathbf{Mn^{III}_6Co^{III}}]^{3+}$, and **3**, compared to the other $[\mathbf{Mn^{III}_6Cr^{III}}]^{3+}$ compounds, comes along with a slight compression of the hexacyanometallate unit along the (approximate) molecular C_3-axis, the octahedron of the central Cr^{III} ion in the other $[\mathbf{Mn^{III}_6Cr^{III}}]^{3+}$ compounds is slightly elongated along the approximate molecular C_3-axis (vide supra; see Figure S8a in the Supporting Information).

The mean C−C bond length in the terminal phenolates of the $[\mathbf{Mn^{III}_6Cr^{III}}]^{3+}$ compounds **1**−**6** is 1.40 Å, which is close to the typical benzene bond length of ∼1.39 Å.[146] In contrast, the C−C bond lengths of the central phloroglucinol rings in the $[\mathbf{Mn^{III}_6Cr^{III}}]^{3+}$ compounds are in the range 1.40−1.44 Å with a mean value of 1.42 Å. This comes along with a shortening of the mean C−O bond length of the central phloroglucinol backbone (1.31 Å) compared to the mean terminal C−O bond distance (1.32 Å).

Electronic Absorption Spectroscopy. The electronic absorption spectra of compounds **3**−**6** dissolved in acetonitrile (Figure 3a) exhibit intense transitions above 20 000 cm^{-1}, with a steady increase in the absorption up to a maximum at 34 150 cm^{-1} ($\varepsilon = 115 \times 10^3$ M^{-1} cm^{-1}). It is evident from these spectra that the $[\mathbf{Mn^{III}_6Cr^{III}}]^{3+}$ compounds are all identical in MeCN solution, except within the region above 35 000 cm^{-1}, where the BPh_4^- counterions in **4**−**6** exhibit additional intensity compared to the lactate salt **3**. Electronic absorption spectra of the hexacyanochromate salts **1** and **2** in solution could not be recorded, because of their low solubility.

The spectrum of $(NEt_4)_3[Cr(CN)_6]$ in MeCN (Figure 3a) exhibits only a weak feature above 35 000 cm^{-1}, which implies that the $[Cr(CN)_6]^{3-}$ building block gives only negligible contributions to the spectra of **3**−**6**. The absorption spectrum of the mononuclear analogue $[(salen')Mn(EtOH)_2]ClO_4$ (H_2salen' = *N*,*N*′-bis(3,5-di-*tert*-butylsalicylidene)-1,2-cyclohexanediamine) in MeCN also shows a steady increase in the absorption (Figure 3a). While the features below 23 000 cm^{-1} have been ascribed to d→d transitions (vide infra),[147−153] the 23 000−30 000 cm^{-1} region has been assigned to d→π^* MLCT transitions involving the imine groups, whereas the 31 000−33 000 cm^{-1} region has been assigned to $\pi\rightarrow\pi^*$ transitions of the imine chromophores.[147−151] LMCT and $\pi\rightarrow\pi^*$ transitions involving the phenolates are supposed to occur at energies above 35 000 cm^{-1}.[147−151]

The spectrum of $[\mathbf{Mn^{III}_6Cr^{III}}]^{3+}$ and the 2-fold superposition of the trinuclear Mn^{III} triplesalen complex $[(talen^{t\text{-}Bu_2})Mn_3(solv)_n]^{3+}$ as generated in situ in MeCN[85] (Figure 3b) exhibit significant differences, which can be attributed to distortions of the trinuclear Mn^{III} triplesalen chromophore induced by its coordination to a hexacyanometallate in $[\mathbf{Mn^{III}_6Cr^{III}}]^{3+}$.[85] On the other hand, it is interesting to compare the electronic structure of a trinuclear Mn^{III} triplesalen complex to that of a mononuclear Mn^{III} salen complex. The difference spectrum of the trinuclear Mn^{III} triplesalen complex and the 3-fold superposition of the mononuclear salen analogue exhibits two positive features in the 27 000−35 000 cm^{-1} region (Figure 3b), indicating additional intensity in the absorption spectrum of the trinuclear triplesalen complex in this region. Note that this additional intensity is a lower limit, as three salen

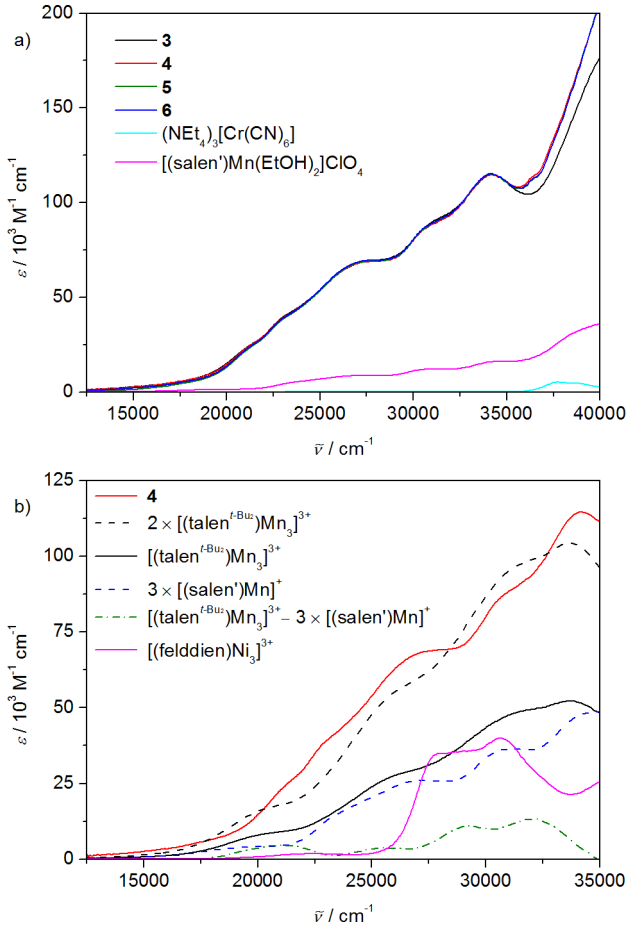

Figure 3. (a) Electronic absorption spectra of **3**−**6**, $(NEt_4)_3[Cr(CN)_6]$, and $[(salen')Mn(EtOH)_2]ClO_4$, all measured in MeCN. (b) Electronic absorption spectrum of **4** (MeCN); the 2-fold superposition of $[(talen^{t\text{-}Bu_2})Mn_3(solv)_n]^{3+}$ as generated in situ in MeCN;[85] spectrum of $[(talen^{t\text{-}Bu_2})Mn_3(solv)_n]^{3+}$, the 3-fold superposition of $[(salen')Mn(EtOH)_2]ClO_4$ (MeCN), and the respective difference spectrum; and spectrum of $[(felddien)Ni_3](BF_4)_3$ (MeCN).[154]

spectra (i.e., the contribution of 6 aromatic rings) have been subtracted from the spectrum of a compound having only 4 aromatic rings. Subtracting only two salen spectra from the triplesalen spectrum results in even more intensity in this region. This difference intensity coincides with two strong absorption features in the 27 000−35 000 cm^{-1} region of $[(felddien)Ni_3]^{3+}$ ($H_3felddien$ = 2,4,6-tris{[2-([2-(dimethylamino)ethyl]methylamino)ethyl]iminomethyl}-1,3,5-trihydroxybenzene)[154] and is a typical signature of the electronic structure of the phloroglucinol backbone that will be discussed later in detail.

For an analysis of the d→d regime, we have performed a Gaussian analysis on the electronic absorption spectrum of $[\mathbf{Mn^{III}_6Cr^{III}}]^{3+}$ below 25 000 cm^{-1}, using a locked background for the bands above 25 000 cm^{-1}. The fitting process for the region below 25 000 cm^{-1} was carried out with a minimum number of Gaussians for which the linewidths were correlated to the same value. We achieved a good reproduction of the experimental data by incorporating three Gaussians at 14 000 cm^{-1} ($\varepsilon = 1.4 \times 10^3$ M^{-1} cm^{-1}), 17 700 cm^{-1} ($\varepsilon = 4.9 \times 10^3$ M^{-1} cm^{-1}), and 21 600 cm^{-1} ($\varepsilon = 21 \times 10^3$ M^{-1} cm^{-1}) (see Figure 4). A fourth band with a correlated linewidth is not resolved in the 22 000−25 000 cm^{-1} region.

dx.doi.org/10.1021/ic301406j | *Inorg. Chem.* 2012, 51, 10929−10954

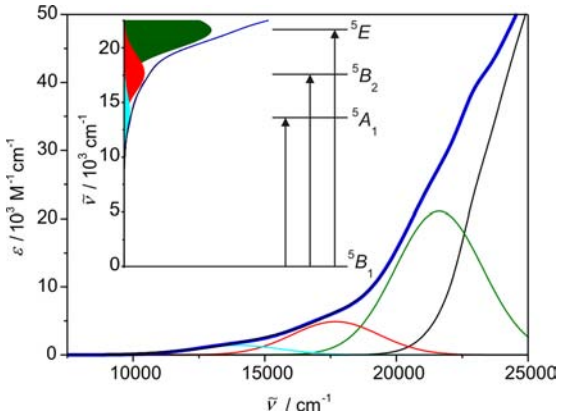

Figure 4. Gaussian resolution of the ligand-field region of the electronic absorption spectrum of **4**. The colored thin lines represent the Gaussian peaks ascribed to ligand-field transitions. The black thin line represents the sum of nonresolved Gaussian peaks at higher energies, the thick line the total sum, and the dashed line the experimental data. Inset: Assignment of the Gaussian peaks to ligand-field transitions, assuming C_{4v} symmetry of the salen-like coordination environment of Mn^{III}.

Ligand-field transitions have been assigned in the 5000–23000 cm^{-1} region for numerous Mn^{III} high-spin complexes with a variety of ligands.[147−153,155−165] Some controversy has arisen over the assignment of these spectra, in particular over the low-intensity band commonly observed in the 5000–16500 cm^{-1} region, which was attributed to (1) a low-energy charge-transfer transition,[155,158] (2) the spin-forbidden $^5E_g \rightarrow {}^3T_{1g}$ transition (in O_h symmetry),[159−161] (3) a spin-allowed transition from the ^5E_g (O_h) ground state to a component of a trigonally split $^5T_{2g}$ (O_h) excited state,[162] or (4) a spin-allowed transition between the components of the ^5E_g (O_h) ground state split by Jahn–Teller distortions.[157,162] The fourth assignment was supported by many investigations, with the bands at higher energy in the ligand-field region being ascribed to transitions between the ground state and the split components of the $^5T_{2g}$ (O_h) excited state.[147−153,156,164,165] Assuming C_{4v} symmetry, the low-energy band then corresponds to the $^5B_1 \rightarrow {}^5A_1$ transition and the bands at higher energy to the $^5B_1 \rightarrow {}^5B_2$ and $^5B_1 \rightarrow {}^5E$ transitions.[164] In mononuclear Mn^{III} salen complexes, three shoulders attributed to these transitions appear in the 11300–16300 cm^{-1} ($\varepsilon \leq 100$ M^{-1} cm^{-1}), 15 000–19 000 cm^{-1} (ε = 100–500 M^{-1} cm^{-1}), and 18 200–22 000 cm^{-1} (ε = 150–1600 M^{-1} cm^{-1}) region, respectively.[147−153]

Based on the literature, we assign the three bands at 14 000, 17 700, and 21 600 cm^{-1} in the absorption spectrum of $[\mathbf{Mn^{III}_6Cr^{III}}]^{3+}$ to the $^5B_1 \rightarrow {}^5A_1$, $^5B_1 \rightarrow {}^5B_2$, and $^5B_1 \rightarrow {}^5E$ transitions, respectively (see Figure 4, inset). The equivalence to the mononuclear Mn^{III} salen complexes indicates that the electronic structure of the Mn^{III} ions is not significantly perturbed by the special electronic structure of the central backbone (vide infra). However, we cannot rule out the possibility of a fourth ligand-field transition being hidden under a CT transition above 22 000 cm^{-1}, as the degeneracy of the ^5E term is most likely removed because the symmetry of the Mn^{III} environment in the trinuclear triplesalen building block is lower than the D_{4h} and C_{4v} symmetries discussed in the literature for mononuclear Mn^{III} salen complexes. The symmetry reduction is also evident from the intensity of the ligand-field transitions in $[\mathbf{Mn^{III}_6Cr^{III}}]^{3+}$, which is increased by a factor of ∼20 compared to the mononuclear Mn^{III} salen complexes. A similar observation has been made in our study on the trinuclear Ni^{II} triplesalen complexes, where an intensity increase by a factor of 8 compared to the mononuclear analogue $[(salen)Ni^{II}]$ was reported for a d→d transition in a trinuclear complex.[77]

Electrochemistry. The electrochemical characterization of $[\mathbf{Mn^{III}_6Cr^{III}}]^{3+}$ is not straightforward as **3**–**6** contain the redox-active anions tetraphenylborate and lactate and the hexacyanochromate salts **1** and **2** do not have sufficient solubility for electrochemical measurements. The cyclic voltammetry (CV) analysis of **6** in acetonitrile (Figure 5) shows a prominent

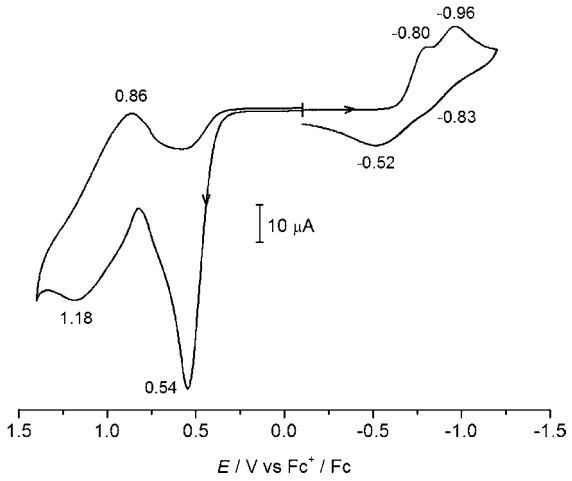

Figure 5. Cyclic voltammogram of **6** in MeCN solution (0.1 M $[NBu_4]PF_6$) at 20 °C recorded at a glassy carbon working electrode. Scan rate = 200 mV s^{-1}.

irreversible oxidation wave at $E_{p,ox}$ = 0.54 V (all potentials are referenced to the Fc^+/Fc couple) which can be attributed to the BPh_4^- counterion, as concluded from the literature[166−168] and confirmed by own electrochemical measurements on $NaBPh_4$ solutions. In addition, nonresolved redox events occur in the 0.8–1.4 V potential range. Several examples of mononuclear Mn^{III} salen complexes being reversibly or quasi-reversibly oxidized in the 0.2–0.9 V potential range were reported in the literature, with the peak potentials depending on the length and substituents of the diimine bridge and on the additional ligands at the fifth and sixth coordination sites of Mn^{III}.[169] Although these oxidations have been termed metal-centered, leading to a Mn^{IV} ion, we refrain from an assignment as they could also be ligand-centered, resulting in the formation of coordinated phenoxyl radicals. This possibility has already been shown for the trinuclear Cu^{II} and Ni^{II} triplesalen complexes[74,77] and for the related trinuclear Cu^{II} triplesalacen complex.[170]

At negative potentials, two irreversible reduction waves occur at $E_{p,red}$ = −0.80 V and −0.96 V. Reversible and irreversible reduction processes in the potential range from −0.7 V to +0.3 V have been described for mononuclear Mn^{III} salen complexes in the literature, which have been attributed to the Mn^{III}/Mn^{II} couple with the peak potentials again depending on the length and substituents of the diimine bridge, on the additional ligands at the fifth and sixth coordination sites of Mn^{III}, and on the nature of the substituents of the phenolates.[169,171,172]

Magnetic Properties. Direct current (DC) and alternating current (AC) magnetic measurements have been performed on various batches of the $[\mathbf{Mn^{III}_6Cr^{III}}]^{3+}$ compounds **1** and **3**–**6**

dx.doi.org/10.1021/ic301406j | Inorg. Chem. 2012, 51, 10929–10954

(see Chart 1). As demonstrated by single-crystal XRD analysis (vide supra), the $[\mathbf{Mn^{III}_6Cr^{III}}]^{3+}$ salts crystallize with several solvent molecules occupying interstitial space in the crystal structures. A loss of solvent molecules occurs immediately upon removal of the crystals from the mother liquor. Therefore, samples of freshly isolated crystals to be magnetically characterized (**1a** and **3a**−**6a**) were prepared by directly transferring the crystals from the mother liquor to the SQUID magnetometer in order to maintain the crystal structure as intact as possible. However, the loss of solvent molecules of crystallization cannot be completely avoided, particularly because the SQUID measurements require purge-and-vent cycles to be performed before the magnetic measurements, in order to exchange the air atmosphere for a helium atmosphere.

In addition to the freshly isolated crystals, samples of air-dried crystals having been kept at room temperature for several days (**3b**−**6b**), and vacuum-dried powder samples (**3c**−**6c**) have been investigated using magnetic measurements. The three different samples of each of the $[\mathbf{Mn^{III}_6Cr^{III}}]^{3+}$ compounds **3**−**6** were prepared from the same batch. Because of the severe difficulties that arose in the preparation of a pure batch of **1** (vide supra), which we finally obtained in a rather small amount, we only performed magnetic measurements on the freshly isolated crystals of this compound.

Importantly, the calculation of μ_{eff} values from experimentally determined magnetization data requires knowledge of the exact molar mass of the homogeneous sample at the precise moment of its weighing. However, this knowledge is rather difficult to obtain, because of the volatility of the solvent molecules of crystallization. In order to establish the formula of the magnetically characterized samples as exactly as possible, we concomitantly submitted a fraction of each sample for elemental analysis. The following example illustrates the significant impact of the quantity of solvent molecules of crystallization on the outcome and interpretation of μ_{eff} values. While single-crystal XRD analysis of **6** led to the formulation as $[\mathbf{Mn^{III}_6Cr^{III}}(MeOH)_3(MeCN)_2](BPh_4)_3{\cdot}4MeCN{\cdot}2Et_2O$,[81] the elemental analysis of the freshly isolated crystals **6a** is in accordance with a formulation as $[\mathbf{Mn^{III}_6Cr^{III}}(MeOH)_3(MeCN)_2](BPh_4)_3{\cdot}3MeCN{\cdot}Et_2O$, $[\mathbf{Mn^{III}_6Cr^{III}}(MeOH)_3(MeCN)_2](BPh_4)_3{\cdot}2MeCN{\cdot}Et_2O$, or $[\mathbf{Mn^{III}_6Cr^{III}}(MeOH)_3(MeCN)_2](BPh_4)_3{\cdot}MeCN{\cdot}Et_2O$. The corresponding molar masses lead to μ_{eff} values of 11.82, 11.76, and 11.70 μ_B, respectively, at 290 K. In this regard, it is important to point out that even for molar masses of ∼4000 g mol^{-1}, the loss of very few solvent molecules of crystallization, which cannot be followed by elemental analysis, results in a considerable variation in μ_{eff} that may lead to significantly different parameter values, especially the *g*-values, in simulations of the magnetic data. Thus, the accuracy of μ_{eff} and such parameter values obtained from magnetic measurements on solvates containing low-boiling solvent molecules of crystallization is limited.

DC Measurements. Temperature-dependent magnetization measurements (2−290 K, 1 T) on the differently prepared samples of the $[\mathbf{Mn^{III}_6Cr^{III}}]^{3+}$ compounds **1** and **3**−**6** reveal an effective magnetic moment (μ_{eff}) in the 11.71−11.92 μ_B range at 290 K (see Figure 6 and Figure S9 in the Supporting Information), with the contribution of the $[Cr^{III}(CN)_6]^{3-}$ counterion to the magnetic moment of **1a** having been subtracted from the experimental data as a Curie $S = {}^3/_2$ spin. The room-temperature values of μ_{eff} are slightly lower than the spin-only value of six uncoupled Mn^{III} h.s. ($S_i = 2$, $g_i = 1.98$) and one uncoupled Cr^{III} ($S_i = {}^3/_2$, $g_i = 1.98$) of 12.48 μ_B. All investigated

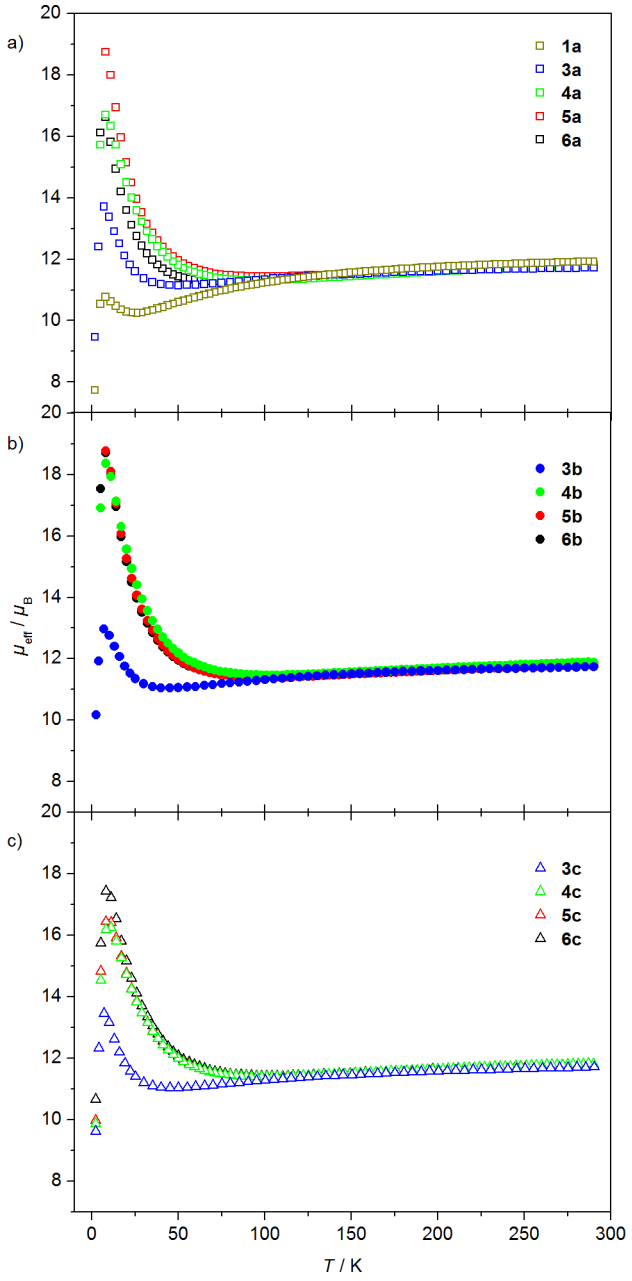

Figure 6. Temperature dependence of μ_{eff} at 1 T for the investigated $[\mathbf{Mn^{III}_6Cr^{III}}]^{3+}$ samples grouped according to their crystallinity, i.e., (a) freshly isolated crystals (**1a** and **3a**−**6a**), (b) air-dried crystals (**3b**−**6b**), and (c) vacuum-dried powder samples (**3c**−**6c**). The contribution of the $[Cr^{III}(CN)_6]^{3-}$ counterion to the magnetic moment of **1a** has been subtracted from the experimental data as a Curie $S = {}^3/_2$ spin.

samples exhibit a slow decrease in μ_{eff} with decreasing temperature until a minimum in μ_{eff} is reached. Further temperature decrease leads to a substantial increase in μ_{eff}. This temperature dependence is characteristic of a ferrimagnetic coupling scheme.

However, the exact curvature of the μ_{eff} vs T curves, in particular the coordinates of their minima and maxima, varies considerably for the different samples, hinting at substantial differences in the exchange interactions between the metal ions. This is particularly striking in the comparison of the μ_{eff} vs T data of **1a** and **3a**−**6a** (Figure 6a). While **1a** reaches a minimum

dx.doi.org/10.1021/ic301406j | *Inorg. Chem.* 2012, 51, 10929−10954

in μ_{eff} of only 10.24 μ_B at 26 K, **3a** has a minimum of 11.14 μ_B at 50 K, and **4a**, **5a**, and **6a** exhibit minima in the 11.27−11.43 μ_B range at 95, 99, and 74 K, respectively. An increase in the temperature of the minimum comes along with an increase in the maximum of μ_{eff} at low temperatures. The highest μ_{eff} value, as measured for **5a** at 8 K (18.74 μ_B), is close to the theoretical value of 21.76 μ_B for an isotropic $S_t = {}^{21}/_2$ with $g = 1.98$. When going from the freshly isolated to the air-dried crystals and further to the vacuum-dried powder samples, the μ_{eff} vs T curves of **4**−**6** approach with the minimum settling at ∼100 K for **4c**−**6c** (Figure 6). This implies a particularly strong curvature variation with changing crystallinity in the case of **6** (see Figure S9d in the Supporting Information).

We have performed field-dependent magnetization measurements at 2 K (see Figure 7 and Figure S10 in the Supporting Information) and VTVH measurements (see Figure 8 and Figure S11 in the Supporting Information) on all samples. In Figures 7a and 8a, the contribution of the $[Cr^{III}(CN)_6]^{3-}$ counterion to the magnetization of **1a** has been subtracted from the experimental data according to the Brillouin function ($S = {}^3/_2$, $g = 2.00$).

The M vs H curves of **4a**−**6a** and **4b**−**6b** exhibit a steeper increase of the magnetization at low fields than those of **1a** and **3a** and **3b** (see Figures 7a and 7b), and the maximum values of the magnetization reached at 7 T are significantly higher for **4a**−**6a** and **4b**−**6b** (17.71−19.00 μ_B) than for **1a** (14.20 μ_B) and **3a** and **3b** (16.13−16.40 μ_B). As observed for μ_{eff} vs T, the M vs H curves of **4**−**6** become increasingly similar when going from the crystalline samples to the vacuum-dried powder samples (Figure 7). In particular, these compounds exhibit qualitatively similar changes, i.e., a less-pronounced increase of the magnetization at low fields and the appearance of a steplike feature at intermediate fields (see Figures S10b−d in the Supporting Information).

The VTVH measurements exhibit a strong nesting behavior of the isofield lines for all samples (see Figure 8 and Figure S11 in the Supporting Information), which is indicative of strong magnetic anisotropy.[173] This is consistent with the magnetization saturation values that do not reach the theoretical value of 20.79 μ_B predicted by the Brillouin function for an isotropic $S = {}^{21}/_2$, $g = 1.98$ system. The very low magnetization of **1a** at 2 K/7 T comes along with a particularly large splitting of the isofield lines (see Figure 8a). While the VTVH curves of **3a**−**c** are almost superimposable (Figure 8b), those of **4**−**6** are strongly dependent on the crystallinity and solvate (see Figures 8c−e and Figure S11 in the Supporting Information). For each of these compounds, the vacuum-dried powder sample exhibits a much stronger splitting of the isofield lines than the crystalline samples, as indicated by significantly lower magnetization values at 1 and 3 T (Figure 8c−e).

DFT Calculations of the J_{Cr-Mn} Exchange Coupling. The J_{Cr-Mn} exchange interaction through the Cr−C≡N−Mn pathway is known to be strongly dependent on the exact structure of the pathway.[174,175] In addition to magnetostructural correlations describing the influence of the C≡N−Mn angle,[175,176] a correlation of J_{Cr-Mn} with the Mn−$N^{C\equiv N}$ bond length has been suggested from magnetic measurements on several $Cr^{III}(CN)_n$-C≡N−Mn(salen) systems, indicating that J_{Cr-Mn} increases with decreasing d(Mn−$N^{C\equiv N}$).[85]

As revealed by single-crystal XRD analysis (vide supra), the C≡N−Mn angles in **1**−**6** do not vary significantly, whereas the Mn−$N^{C\equiv N}$ bond length differs by ∼0.1 Å for six-coordinate Mn^{III} ions compared to Mn^{III} ions with a vacant sixth

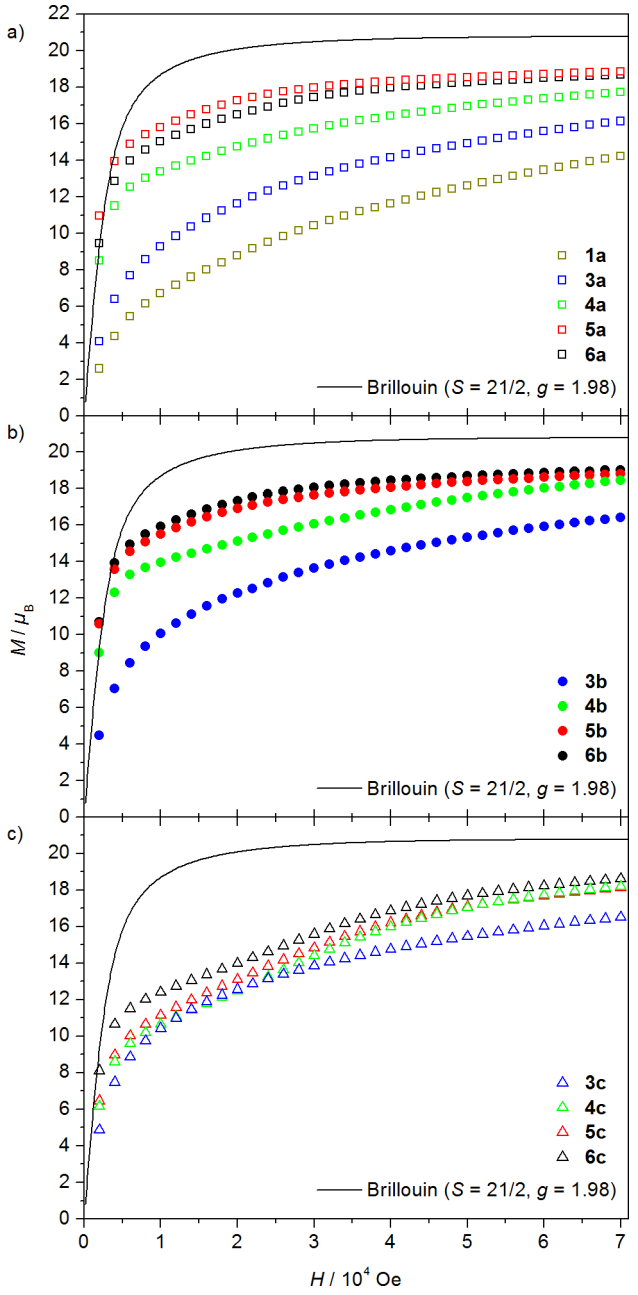

Figure 7. Field dependence of the magnetization at 2 K for the investigated $[Mn^{III}_6Cr^{III}]^{3+}$ samples grouped according to their crystallinity, i.e., (a) freshly isolated crystals (**1a** and **3a**−**6a**), (b) air-dried crystals (**3b**−**6b**), and (c) vacuum-dried powder samples (**3c**−**6c**). In addition to the experimental data, the Brillouin function is shown for $S = {}^{21}/_2$, $g = 1.98$. The contribution of the $[Cr^{III}(CN)_6]^{3-}$ counterion to the magnetization of **1a** has been subtracted from the experimental data according to the Brillouin function ($S = {}^3/_2$, $g = 2.00$).

coordination site. In an attempt to quantify the influence of the Mn−$N^{C\equiv N}$ bond length on the J_{Cr-Mn} exchange coupling, we performed DFT calculations for three molecular structures of $[Mn^{III}_6Cr^{III}]^{3+}$: the experimental structure obtained from single-crystal XRD data of the highly symmetric $[Mn^{III}_6Cr^{III}]^{3+}$ compound **3**, and for two hypothetical structures in which the trinuclear Mn^{III} triplesalen building blocks were rigidly shifted along the molecular S_6 axis, such that a variation of approximately ±0.1 Å, with respect to the experimentally determined

dx.doi.org/10.1021/ic301406j | Inorg. Chem. 2012, 51, 10929−10954

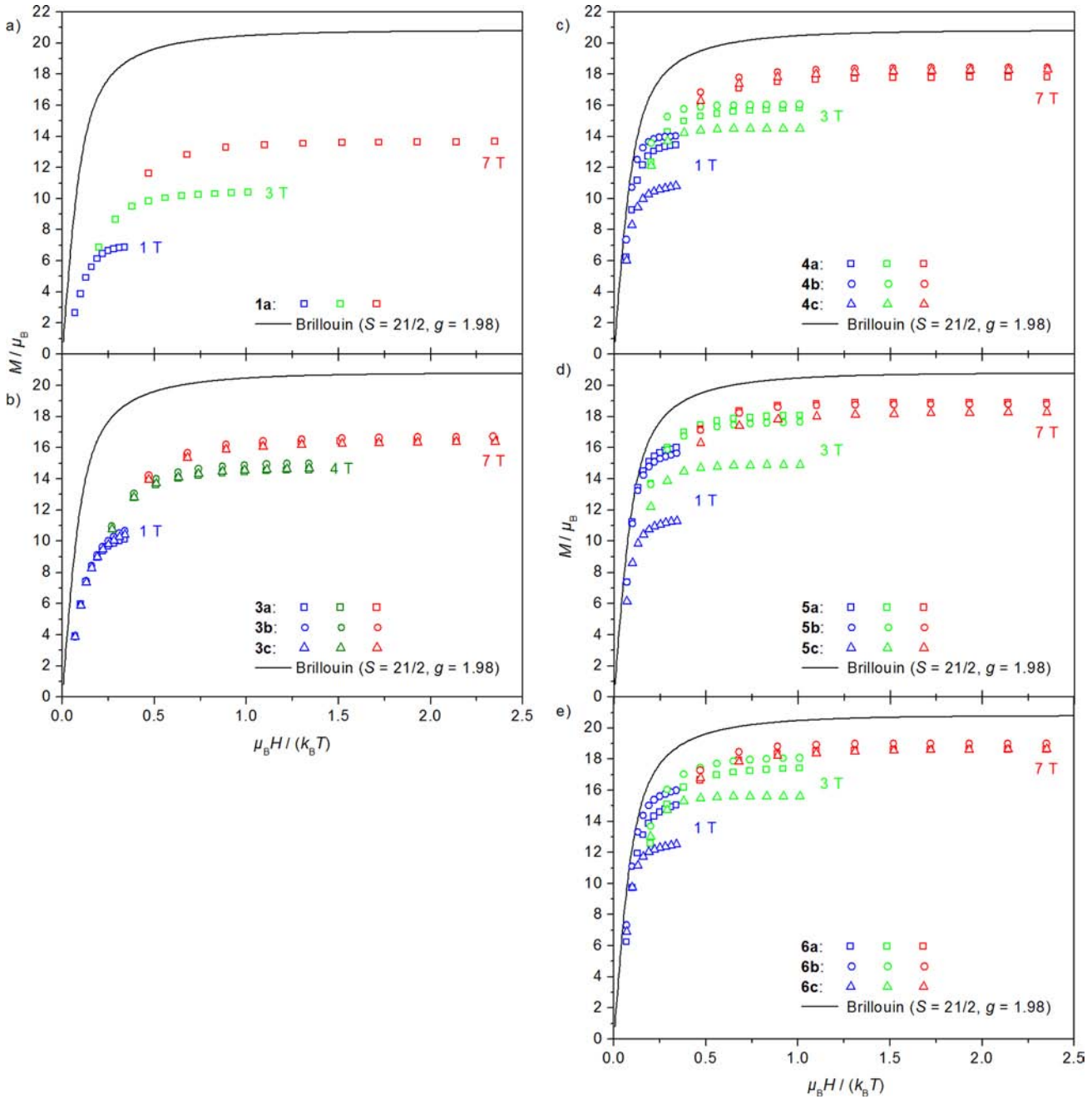

Figure 8. VTVH magnetization measurements at 1 T (blue), 3 or 4 T (green), and 7 T (red) for the investigated $[Mn^{III}_6Cr^{III}]^{3+}$ samples grouped according to compounds, i.e., (a) **1a**, (b) **3a**–**c**, (c) **4a**–**c**, (d) **5a**–**c**, and (e) **6a**–**c**. In addition to the experimental data, the Brillouin function is shown for $S = {}^{21}/_{2}$, $g = 1.98$. The contribution of the $[Cr^{III}(CN)_6]^{3-}$ counterion to the magnetization of **1a** has been subtracted from the experimental data according to the Brillouin function ($S = {}^{3}/_{2}$, $g = 2.00$).

value (2.185 Å), is realized for the $Mn-N^{C\equiv N}$ bond length. This shift entails a variation in the C≡N−Mn angle of negligible magnitude (see Table 2).

For each structure, precise total-energy calculations were performed for two different spin configurations: a parallel alignment of all local spins, i.e., of the six Mn^{III} ($S_i = 2$) spins and the Cr^{III} ($S_i = {}^{3}/_{2}$) spin, referred to as the ferromagnetic configuration (FO); and a ferrimagnetic configuration (FI) with the Cr^{III} spin antiparallel to the Mn^{III} spins. Both configurations resulted in metastable states with the total energy being always lower for the ferrimagnetic configuration, hinting at the antiferromagnetic nature of the Cr−Mn coupling.

Table 2. Structural Parameters of the Cr−C≡N−Mn Pathway, and Exchange Parameters As Estimated from DFT Calculations, for Three Molecular Structures of $[Mn^{III}_6Cr^{III}]^{3+}$ Related by Rigid Shifts of the Trinuclear Mn^{III} Triplesalen Building Blocks along the Molecular S_6 Axis

$d(Mn-N^{C\equiv N})$ [Å]	∠(C≡N−Mn) [°]	$E_{FO} - E_{FI}$ [meV]	J_{Cr-Mn} [cm^{-1}]
2.100	160.0	137.316	−15.4
2.185	158.3	99.570	−11.2
2.300	156.2	67.292	−7.5

In order to achieve quantitative estimations of the corresponding exchange parameter J_{Cr-Mn}, one can refer to a simple model

dx.doi.org/10.1021/ic301406j | Inorg. Chem. 2012, 51, 10929−10954

with isotropic nearest-neighbor interactions between transition-metal ions by retaining the first right-side term only in eq 1:

$$E_{FO} = -2 \times 6J_{Mn-Mn}S_{Mn}{}^2 - 2 \times 6J_{Cr-Mn}S_{Mn}S_{Cr} \quad (2)$$

$$E_{FI} = -2 \times 6J_{Mn-Mn}S_{Mn}{}^2 + 2 \times 6J_{Cr-Mn}S_{Mn}S_{Cr} \quad (3)$$

$$J_{Cr-Mn} = \frac{E_{FI} - E_{FO}}{24S_{Mn}S_{Cr}} = \frac{E_{FI} - E_{FO}}{72} \quad (4)$$

For the sake of simplicity, we assumed in eq 4 the "nominal" spin values $S_{Mn} = 2$ and $S_{Cr} = 3/2$ as obtained from calculations as "rigid" and configuration-independent ones, yielding the total half-integer spin moments $(S_z)_{FO} = {}^{27}/_2$ and $(S_z)_{FI} = {}^{21}/_2$.

As evident from Table 2, a variation of $d(Mn-N^{C\equiv N})$ by approximately ±5% results in the magnitude of J_{Cr-Mn} changing by approximately ±35%. As expected, the interaction strengthens with decreasing $Mn-N^{C\equiv N}$ bond length, but the rapidity of this strengthening is remarkable. It is known from the practice of DFT calculations that the estimates of magnetic exchange parameters, done either from energy-difference arguments or from perturbation-theory formulas, do typically overestimate the experimentally derived data (vide infra) by a factor of ~3. This can be traced to the drawbacks of "conventional" DFT to treat excitations that, as in the present case, occur across the (underestimated) band gap.[177] However, the trends in the variation of exchange parameters, with sources of systematic error when considering similar systems being removed, can be regarded as reliable.

Spin-Hamiltonian Simulations of the DC Magnetic Data. We have performed a full-matrix diagonalization of the appropriate spin-Hamiltonian for the different $[\mathbf{Mn^{III}_6Cr^{III}}]^{3+}$ compounds including isotropic HDvV exchange, zero-field splitting, and Zeeman interaction (see the Experimental Section). A frequently used simplification in such spin-Hamiltonians is a collinearity of the local **D**-tensors, which is not appropriate in all cases. We have incorporated the zero-field splitting for the Mn^{III} ions including the relative orientations of the individual **D**-tensors by the angle ϑ of the Jahn–Teller axes with the molecular axis, while the anisotropy axis of the Cr^{III} ion points along the molecular axis. The counterion $[Cr^{III}(CN)_6]^{3-}$ in **1a** was not taken into account in the spin-Hamiltonian, but the respective experimental data were corrected for the contribution of an isotropic $S = {}^3/_2$ spin (vide supra).

The topology of $[\mathbf{Mn^{III}_6Cr^{III}}]^{3+}$ requires a coupling scheme with at least two different coupling constants: J_{Cr-Mn} describes the interaction between the central Cr^{III} (S_7) with each Mn^{III} (S_1 to S_6), and J_{Mn-Mn} describes the interaction between pairs of Mn^{III} ions in a trinuclear triplesalen subunit (Figure 9a). In our attempts to reproduce the magnetic data of **4**–**6**, which exhibit both five- and six-coordinate Mn^{III} ions and, thus, different $Mn-N^{C\equiv N}$ bond lengths (vide supra), we have taken the results of our DFT calculations (vide supra) into account by also employing a more complex coupling scheme, incorporating two different coupling constants: $J^{(1)}_{Cr-Mn}$ and $J^{(2)}_{Cr-Mn}$ (see Figure 9b).

Figure 10 illustrates the influence of the individual spin-Hamiltonian parameters on the temperature dependence of μ_{eff}. As evident from Figures 10a–c, the variation of coupling constants strongly influences the μ_{eff} vs T curves, whereas they are highly insensitive to zero-field splittings (Figure 10d and 10e). In order to evaluate the impact of the latter, simulations of VTVH measurements are necessary.

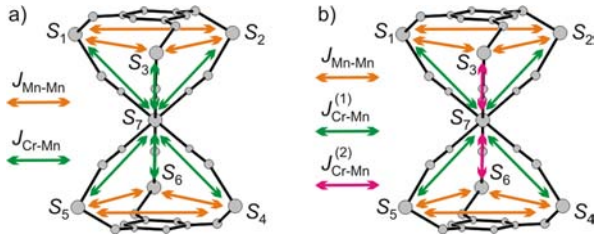

Figure 9. Coupling schemes for the analysis of the magnetic data incorporating the $Mn^{III}-Mn^{III}$ exchange interaction (J_{Mn-Mn}) and (a) only one coupling constant (J_{Cr-Mn}) or (b) two different coupling constants ($J^{(1)}_{Cr-Mn}$ and $J^{(2)}_{Cr-Mn}$), taking into account the inversion symmetry of the employed spin-Hamiltonian.

With the aim of simulating the magnetic data of **1a**, **3a**–**6a**, and **3c**–**6c** as limiting cases of the crystallinity variation in our study, we performed an intensive search in the spin-Hamiltonian parameter space. We were able to satisfactorily reproduce the μ_{eff} vs T data of all these samples and also the VTVH data except for those of **4a**–**6a**. In particular, the unusually high magnetization values of the 1 T isofield lines of **4a**–**6a** (see Figure 8c–e and Figure S11a in the Supporting Information) could not be simulated assuming reasonable values for D_{Mn} and D_{Cr}. With increasing magnetic field, the isofield lines are qualitatively better reproduced. This indicates the presence of quite strong dipolar intermolecular interactions between the large magnetic moments of the $[\mathbf{Mn^{III}_6Cr^{III}}]^{3+}$ molecules that are broken down more efficiently by higher fields, thus leading to better validity of the purely molecular approximation of the simulations.

The parameter sets yielding the best reproductions for **1a**, **3a**–**6a**, and **3c**–**6c** are summarized in Table 3, and selected simulations, together with the experimental data, are shown in Figure 11 and Figures S12–S17 in the Supporting Information. The corresponding energy-level schemes for **1a**, **3a**, **3b**, and **4c**–**6c** are provided in Figures S18–S21 in the Supporting Information. The incorporation of two different $J^{(1,2)}_{Cr-Mn}$ couplings provided no qualitative changes in the simulations (see Figure S14 in the Supporting Information) and, therefore, was omitted. Besides, because of the small contribution of the $S_{Cr} = {}^3/_2$ spin to the overall magnetic moment and the qualitatively similar influence of D_{Cr} and D_{Mn} on the VTVH curves (see Figure S17b in the Supporting Information), D_{Cr} was generally fixed at 0.00 cm^{-1} while D_{Mn} was varied in order to not overparameterize the system. Importantly, the exchange couplings for **6c** ($J_{Mn-Mn} = -0.70 \pm 0.30$ cm^{-1}, $J_{Cr-Mn} = -5.00 \pm 0.50$ cm^{-1}) are in agreement with the previously reported values ($J_{Mn-Mn} = -1.03$ cm^{-1}, $J_{Cr-Mn} = -5.0$ cm^{-1}) from simulations of the μ_{eff} vs T data of a vacuum-dried powder sample of **6** above 50 K, without taking zero-field splittings into account.[81]

AC Measurements. In order to investigate the relaxation behavior of the different $[\mathbf{Mn^{III}_6Cr^{III}}]^{3+}$ salts and solvates, we performed detailed temperature- and frequency-dependent AC magnetic susceptibility measurements. Figure S22–S24 in the Supporting Information summarize the in-phase (χ'_M) and the out-of-phase (χ''_M) components of the AC susceptibility of **1a**, **3a**, and the various samples of **4**–**6** in the 1.8–3.4 K temperature range at seven frequencies between 660 and 1488 Hz. All samples show at least a frequency-dependent onset of the out-of-phase component of the AC susceptibility at low temperatures, demonstrating a slow relaxation of the magnetization indicative of single-molecule magnet behavior. **1a** and **3a** do not exhibit maxima in χ''_M above 1.8 K (see Figure S22 in

dx.doi.org/10.1021/ic301406j | *Inorg. Chem.* 2012, 51, 10929–10954

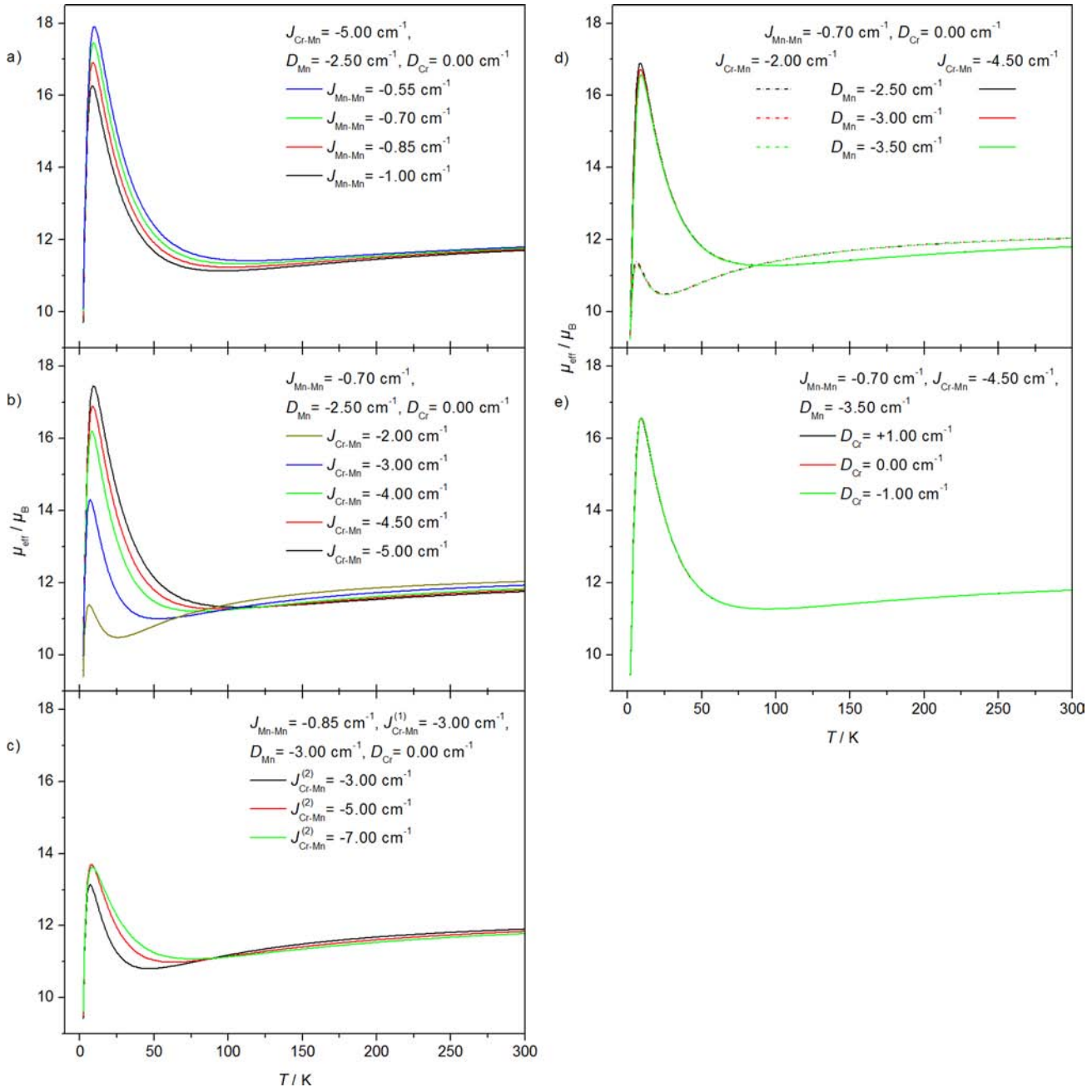

Figure 10. Simulations of the temperature dependence of μ_{eff} at 1 T performed by a full-matrix diagonalization of the complete spin-Hamiltonian. The simulations were carried out (i) using the coupling scheme in Figure 9a with all parameters fixed except for (a) J_{Mn-Mn}, (b) J_{Cr-Mn}, (d) D_{Mn} (for two sets of fixed parameters), and (e) D_{Cr}; or (ii) using the coupling scheme in Figure 9b with all parameters fixed except for $J^{(2)}_{Cr-Mn}$ (see panel c).

the Supporting Information), in contrast to the $[\mathbf{Mn^{III}_6Cr^{III}}](BPh_4)_3$ samples (see Figure S24 in the Supporting Information). While **4** shows only slight differences in the AC susceptibility as a function of crystallinity, with one maximum in χ''_M for all samples, the loss of crystallinity in the case of **5** and **6** comes along with a progressive merging of two peaks or shoulders in χ''_M attributable to distinct species with different magnetization relaxation rates (see Figure S24 in the Supporting Information).

The temperature at a maximum in χ''_M for a given frequency corresponds to the temperature at which the magnetization relaxation rate $1/\tau$ of a species equals the frequency of the AC field. For sufficiently resolved maxima, this temperature was determined for each frequency by fitting the χ''_M vs T data to a Gaussian−Lorentzian sum function, which provides a τ vs T dataset for the respective species. The fitting procedure was performed using the program PeakFit,[178] which offers various combinations of Gaussians and Lorentzians in addition to the pure functions. The best fits were consistently obtained with the Gaussian−Lorentzian sum function. Assuming an Arrhenius expression for the temperature dependence of the magnetization relaxation time,[3]

$$\tau = \tau_0 \times \exp\left(\frac{U_{eff}}{k_B T}\right) \quad (5)$$

the effective energy barrier for spin reversal (U_{eff}) and the pre-exponential factor (τ_0) were determined by fitting the τ vs T

dx.doi.org/10.1021/ic301406j | Inorg. Chem. 2012, 51, 10929−10954

Table 3. Parameter Ranges of J_{Mn-Mn}, J_{Cr-Mn}, and D_{Mn} Determined for 1a, 3a−6a, and 3c−6c By Simulations of Their μ_{eff} vs T and/or VTVH Data[a]

sample	J_{Mn-Mn}[b] [cm^{-1}]	J_{Cr-Mn}[b] [cm^{-1}]	D_{Mn}[c] [cm^{-1}]
1a	−1.00 ± 0.30	−2.40 ± 0.50	−4.00 ± 0.50
3a	−0.85 ± 0.30	−3.00 ± 0.50	−3.00 ± 0.50
3c	−0.85 ± 0.30	−3.00 ± 0.50	−3.00 ± 0.50
4a[d]	−0.70 ± 0.30	−4.50 ± 0.50	-
4c	−0.70 ± 0.30	−4.50 ± 0.50	−3.50 ± 0.50
5a[d]	−0.70 ± 0.30	−5.00 ± 0.50	-
5c	−0.70 ± 0.30	−4.50 ± 0.50	−3.50 ± 0.50
6a[d]	−0.70 ± 0.30	−4.00 ± 0.50	-
6c	−0.70 ± 0.30	−5.00 ± 0.50	−3.00 ± 0.50

[a]The simulations were performed by a full-matrix diagonalization of the complete spin-Hamiltonian using the coupling scheme in Figure 9a. [b]Generally determined by simulations of the experimental μ_{eff} vs T and VTVH data. [c]Determined by simulations of the experimental VTVH data. [d]No satisfactory reproduction of the experimental VTVH data, especially of the unusually high magnetization values of the 1 T isofield line, was possible assuming reasonable values for D_{Mn} and D_{Cr}.

data to eq 5. The resulting values of U_{eff} and τ_0 for the various samples of **4**−**6** are summarized in Table 4. Note that the values obtained for **6c** (especially U_{eff}) are in good agreement with the previously reported values obtained from χ''_M vs T data of a vacuum-dried sample of **6** (U_{eff} = 25.4 K, $\tau_0 = 8 \times 10^{-10}$ s).[81]

To complete the analysis of the χ_{AC} vs T data, we evaluated the parameter F introduced by Mydosh (eq 6),[179] which allows one to distinguish between spin glasses and other systems exhibiting a frequency dependence in χ_{AC}:

$$F = \frac{\Delta T_m(\nu)}{T_f \Delta(\log \nu)} \quad (6)$$

Here, $\Delta T_m(\nu)$ represents the shift of the temperature coordinate $T_m(\nu)$ of the maximum in the χ'_M vs T plot with varying frequency ν, and $T_f = \lim_{\nu \to 0} T_m(\nu)$.[180] For spin glasses, T_f is the phase-transition temperature obtained from DC measurements. For other systems such as single-molecule magnets exhibiting a frequency-dependent AC signal, but no phase transition, T_f cannot be accurately determined, which limits the applicability of the parameter F to such systems.[181] However, F has been frequently estimated for SMMs by using an approximate T_f value determined from the maximum in the χ'_M vs T curve corresponding to the lowest operating frequency. In this respect, F-values between 0.18 and 0.24 were calculated for the various samples of **4**−**6**, which clearly rule out a spin-glass nature of these samples, as typical F-values of spin glasses are one or two decades lower.[179]

In addition to analyzing the temperature dependence of the AC susceptibility at constant frequencies, we investigated its frequency dependence at fixed temperatures. Figure S25 in the Supporting Information, Figure 12, and Figure 13 exhibit the χ'_M vs ω, χ''_M vs ω, and χ''_M vs χ'_M plots, respectively, that were constructed from AC susceptibility measurements on the different samples of **4**−**6** at 1.83, 1.90, 2.00, and 2.10 K in the 0.1−1500 Hz range with the frequency equidistantly sampled on a logarithmic scale. These experimental data are in good agreement with the χ_{AC} vs T data of the various samples of **4**−**6** (vide supra) with respect to the number of different species in each sample and their variation with changing crystallinity. In most cases, the AC data at constant temperatures

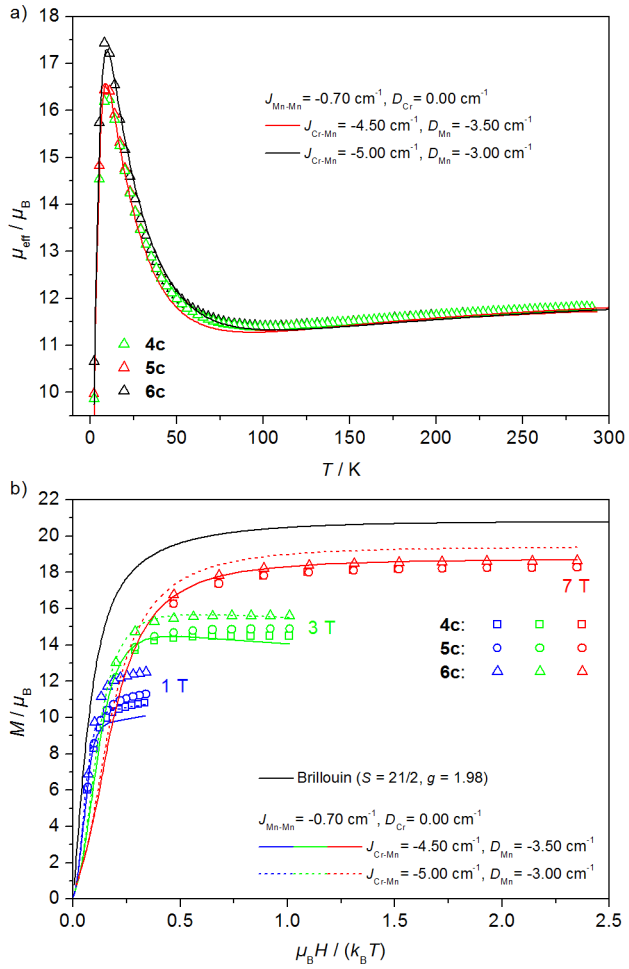

Figure 11. (a) Temperature dependence of μ_{eff} at 1 T and (b) VTVH magnetization measurements at 1 T (blue), 3 T (green), and 7 T (red) for **4c**−**6c**. Experimental data are given as symbols; the lines correspond to simulations performed by a full-matrix diagonalization of the complete spin-Hamiltonian using the coupling scheme in Figure 9a and the parameter sets provided in Table 3 for **4c**−**6c**. For a better appraisal of the estimated accuracy of the parameter values, an extended version of this figure, including a larger number of simulations, is provided in the Supporting Information (Figure S17). In addition, the Brillouin function is shown in panel b for $S = {}^{21}/_{2}$, g = 1.98.

could be fitted to a generalized Debye model describing a single relaxation process with a distribution of relaxation times (the fits are represented as lines in Figure S25 in the Supporting Information, Figure 12, and Figure 13; details of the model, the fitting procedure, and the extracted parameters are provided in the Supporting Information).[4,182] The U_{eff}, τ_0, and α values obtained from these fittings are summarized in Table 4. For some samples, table entries are missing, because a description of the experimental data by a single relaxation process was not possible. In the case of **5a** and **6a**, for which all AC data indicate the presence of at least two relaxation processes with significantly different average relaxation times, a fit to a sum of Debye terms could not be performed, because the relaxation process on the higher-frequency side is insufficiently defined, due to the upper frequency limit (1500 Hz) of the SQUID. The samples for which a fitting to a single relaxation process was possible exhibit α values in the 0.3−0.5 range, indicating a more or less broad distribution of relaxation

dx.doi.org/10.1021/ic301406j | Inorg. Chem. 2012, 51, 10929−10954

Table 4. U_{eff} and τ_0 Values Determined from Least-Squares Fits of $\tau_{(av)}$ vs T Data to the Arrhenius Equation (eq 5), and α Values Obtained from Least-Squares Fits of χ''_M vs χ'_M Data to eq S3 in the Supporting Information, for the Differently Prepared Samples of 4−6

sample	U_{eff}[a] [K]	τ_0[a] [s]	U_{eff}[e] [K]	τ_0[e] [s]	α(1.83 K)[g]	α(1.90 K)[g]	α(2.00 K)[g]	α(2.10 K)[g]
4a	24.2	1.1×10^{-8}	21.2	5.1×10^{-8}	0.29	0.31	0.29	0.31
4b	25.9	8.9×10^{-9}	24.5	1.9×10^{-8}	0.31	0.31	0.31	0.30
4c	26.5	8.2×10^{-9}	25.1	1.8×10^{-8}	0.41	0.40	0.36	0.34
5a	27.6[b,c]	5.6×10^{-9} [b,c]	27.8[b,f]	9.8×10^{-10} [b,f]				
5b	~16[d]		23.0	1.5×10^{-9}	0.41		0.41	
5c	24.6	1.3×10^{-8}	25.3	1.8×10^{-9}	0.51	0.49	0.46	0.42
6a			26.5[b,f]	1.5×10^{-9} [b,f]				
6b	~16[d]				0.52	0.49		
6c	26.4	7.2×10^{-9}	24.8	2.6×10^{-9}	0.37	0.37	0.36	0.35

[a]From χ''_M vs T data. Unless otherwise stated, τ vs T datasets were obtained by fitting the χ''_M vs T data at constant frequencies to a Gaussian−Lorentzian sum function (PeakFit).[178] [b]Slow-relaxing species. [c]A τ vs T dataset was obtained by simulating the χ''_M vs T data at constant frequencies with a Gaussian−Lorentzian sum function (PeakFit).[178] [d]Faster-relaxing species. The goodness of the Arrhenius fit was not sufficient to provide a reliable estimate of τ_0. [e]From χ''_M vs ω data. Unless otherwise stated, τ_{av} vs T datasets were obtained from least-squares fits of the χ''_M vs ω data at constant temperatures to eq S2 in the Supporting Information. [f]A τ_{av} vs T dataset was obtained by visual estimation of the maxima in the χ''_M vs ω curves at constant temperatures. [g]From least-squares fits of χ''_M vs χ'_M data to eq S3 in the Supporting Information.

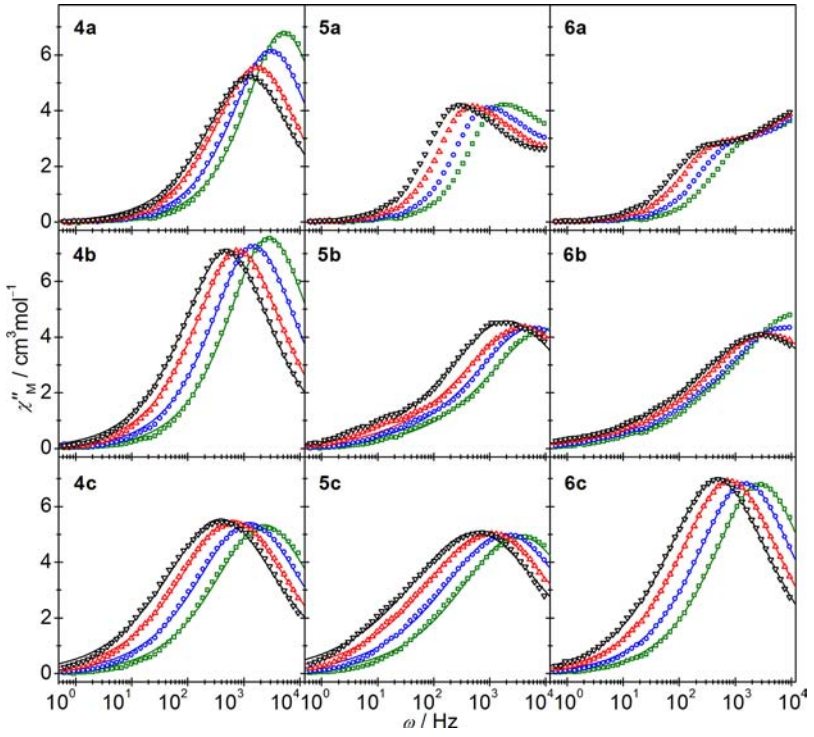

Figure 12. Plots of the out-of-phase component (χ''_M) of the AC susceptibility versus the angular frequency (ω) for the various samples of **4−6** at zero DC field, with the temperature fixed at 1.83 (black), 1.90 (red), 2.00 (blue), and 2.10 K (green). Solid lines are least-squares fits to eq S2 in the Supporting Information.

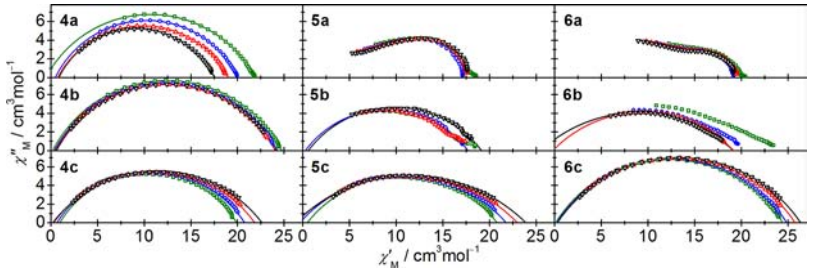

Figure 13. Argand plots of the AC susceptibility of the various samples of **4−6** at zero DC field, with the temperature fixed at 1.83 (black), 1.90 (red), 2.00 (blue), and 2.10 K (green). Solid lines are least-squares fits to eq S3 in the Supporting Information. Note that the χ'_M- and χ''_M-axes of each coordinate system have the same unit length, so that deviations from an ideal semicircle corresponding to $\alpha = 0$ are visualized.

dx.doi.org/10.1021/ic301406j | Inorg. Chem. 2012, 51, 10929−10954

times. For the samples with the smallest α values (i.e., **4a**, **4b**, **6c**), there is virtually no spread in α within the investigated temperature range, and the agreement of the fits with the experimental data is excellent (see especially Figures 12 and 13). In contrast, the samples with larger α values generally exhibit more pronounced spreads in the individual values at different temperatures and a poorer agreement of the fits with the experimental data. This indicates the presence of multiple relaxation processes with an overall distribution of relaxation times that can only approximately be described by a generalized Debye model taking into account a single process.

Finally, we want to comment on the χ_S and χ_T values obtained from the fittings. We refrain from discussing the χ_S values, because these are not well-defined by the experimental data, because of the upper frequency limit (1500 Hz) of the SQUID. On the other hand, the χ_T values provide valuable information about the spin ground state S_t of $[\mathbf{Mn^{III}_6Cr^{III}}]^{3+}$, as saturation effects do not complicate the analysis of AC data at low temperatures in contrast to the respective DC data at higher fields. A calculation of μ_{eff} in the temperature range of 1.83−2.10 K, using χ_T data from χ''_M vs χ'_M fits, leads to μ_{eff} values in the 16−21 μ_B range for the investigated $[\mathbf{Mn^{III}_6Cr^{III}}](BPh_4)_3$ samples. In view of a theoretical value of 21.76 μ_B predicted by Curie's law for an $S = {}^{21}/_2$ spin (g = 1.98), the μ_{eff} values based on χ_T are consistent with an $S_t = {}^{21}/_2$ ground state.

To illustrate the differences between μ_{eff} values determined from AC and DC measurements, the temperature dependence of μ_{eff}, as calculated from the χ_{DC} and χ'_M data of **4c** in the 1.83−35 K range, is depicted in Figure 14, together with some

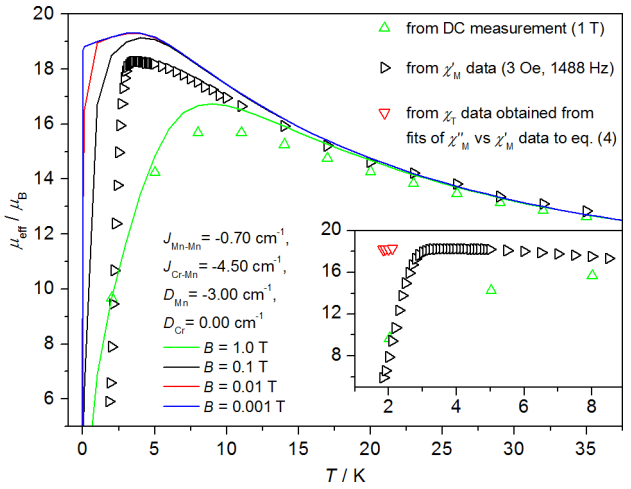

Figure 14. Temperature dependence of μ_{eff}, as calculated from χ_{DC}, χ'_M, and χ_T data of **4c**. Experimental data are given as symbols. The solid lines correspond to simulations performed by a full-matrix diagonalization of the complete spin-Hamiltonian using the coupling scheme in Figure 9a, with all parameters fixed except for B.

simulations showing the influence of a DC field in the 1.0−0.001 T range. In the paramagnetic temperature regime where χ''_M is zero, i.e., above 3.5 K, the χ'_M values are actually χ_T values and, therefore, yield reasonable μ_{eff} values. As evident from Figure 14, the μ_{eff} values obtained from χ_{DC} and χ'_M are in good agreement in the higher-temperature region of the paramagnetic regime, whereas a considerable divergence is observed below 10 K due to saturation effects in the DC measurement, leading to a decrease in the respective μ_{eff}. This is consistent with a better reproduction of the μ_{eff} vs T data based on χ'_M by the simulations at lower fields (B = 0.1−0.001 T).

At temperatures below the paramagnetic regime (i.e., in the region below 3.5 K), χ'_M no longer equals χ_T, because of the onset of the out-of-phase component of the AC susceptibility (see Figure S24 in the Supporting Information). This leads to the observed decrease in μ_{eff} that was determined from χ'_M. As illustrated in the inset of Figure 14, the μ_{eff} values calculated from the fitted parameter χ_T in the 1.83−2.10 K region nicely coincide with the extrapolation of μ_{eff} obtained from χ'_M at the lower-temperature limit of the paramagnetic regime.

DISCUSSION

Crystal Structure Control. The preparation of compounds **1**−**6** starts from the same tricationic species $[\{(talen^{t\text{-}Bu_2})Mn^{III}_3\}_2\{Cr^{III}(CN)_6\}(solv)_n]^{3+}$, but the crystal structures differ significantly. Using 1 equiv of the spherical anion $[Cr^{III}(CN)_6]^{3-}$ per $H_6talen^{t\text{-}Bu_2}$ results in compounds **1** and **2**, both having $[Cr^{III}(CN)_6]^{3-}$ as a counterion, which forms hydrogen-bonded quasi-1D chains with the $[\mathbf{Mn^{III}_6Cr^{III}}]^{3+}$ trications in **1** and covalently linked 1D chains in **2**. The crystal structures obtained with the spherical anion BPh_4^- are dependent on the exact solvent composition, with the resulting $[\mathbf{Mn^{III}_6Cr^{III}}](BPh_4)_3$ solvates exhibiting unpredictable relative orientations of the individual $[\mathbf{Mn^{III}_6Cr^{III}}]^{3+}$ molecules in their crystal structures. This is illustrated by the random distribution of the angle between the approximate molecular C_3 axes, which is almost collinear in **5** (2.2°), 41.7° in **6**, and 68.9° in **4**.

Because the symmetry of the crystal structure and the relative orientation of the individual SMM complexes are crucial for the elimination of rhombic anisotropy terms, which are related to the probability of QTM, we tried to crystallize a $[\mathbf{Mn^{III}_6Cr^{III}}]^{3+}$ compound in a highly symmetric space group. Considering that spherical anions such as those incorporated in **1**, **2**, and **4**−**6** are obviously not suitable to achieve this, we, instead, employed the rod-shaped anion lactate. In this manner, we were able to enforce the crystallization of **3** in the highly symmetric space group $R\bar{3}$ with the $[\mathbf{Mn^{III}_6Cr^{III}}]^{3+}$ complexes all aligned with the c-axis of the unit cell. This simple but efficient approach seems to be a suitable strategy for controlling the crystal structure in further efforts to improve our SMMs.

Molecular Structures. While starting from the same molecular $[\{(talen^{t\text{-}Bu_2})Mn^{III}_3\}_2\{Cr^{III}(CN)_6\}(solv)_n]^{3+}$ species in solution (vide supra), the different crystallization conditions entail subtle variations in the exact molecular structure of the $[\mathbf{Mn^{III}_6Cr^{III}}]^{3+}$ complexes in **1**−**6**. On the one hand, there is a high variability in the occupation of the sixth coordination sites of the Mn^{III} ions. These differ strongly in **1** and **2**, although these compounds crystallize from the same methanol−water reaction solution. The $[\mathbf{Mn^{III}_6Cr^{III}}]^{3+}$ complexes in **1** carry methanol molecules at all Mn^{III} ions, whereas in **2**, the Mn^{III} ions are coordinated either by methanol, water, or a N atom of a $[Cr^{III}(CN)_6]^{3-}$ unit linking different $[\mathbf{Mn^{III}_6Cr^{III}}]^{3+}$ entities. In the $[\mathbf{Mn^{III}_6Cr^{III}}](BPh_4)_3$ solvates **4**−**6**, the Mn^{III} sixth coordination site is particularly variable, being either vacant or occupied by an acetonitrile, an acetone, a methanol, or a water molecule. This randomness is naturally eliminated in the highly symmetric $[\mathbf{Mn^{III}_6Cr^{III}}](lac)_3$ compound **3**, in which each $[\mathbf{Mn^{III}_6Cr^{III}}]^{3+}$ complex is generated by a crystallographic S_6-axis, enforcing identically occupied sixth coordination sites within each molecule. However, as the asymmetric unit contains twice a sixth of a $[\mathbf{Mn^{III}_6Cr^{III}}]^{3+}$ complex, there are two different Mn−O^{MeOH} distances of 2.29 and 2.34 Å in this compound.

dx.doi.org/10.1021/ic301406j | Inorg. Chem. 2012, 51, 10929−10954

The differences in the occupation of the Mn^{III} sixth coordination sites have a strong impact on the $Mn-N^{C\equiv N}$ bond lengths, which are shorter by ~0.1 Å for five-coordinated Mn^{III} ions compared to six-coordinated ones. This variation strongly influences the J_{Cr-Mn} exchange coupling (vide infra).

On the other hand, there are slight variations in the molecular structures of **1**−**6** relating to the trigonal distortion of the central hexacyanochromate. This unit is slightly elongated along the approximate molecular C_3 axis of the $[\mathbf{Mn^{III}_6Cr^{III}}]^{3+}$ complexes in all compounds except **3**, which exhibits a trigonal compression. This difference is accompanied by a less pronounced bending of the individual Mn^{III} salen subunits, as evidenced by the folding angle $\varphi^{central}$, which is smaller by ~10° in **3** compared to the other compounds, and with a stronger helical distortion of the salen subunits as inferred from the angle θ, which is 8.5° in **3** compared to values of <2° in the other compounds.

These subtle differences in the molecular structures of **1**−**6** demonstrate the limitations of molecular design. While atom connectivities and the overall three-dimensional (3D) arrangement of the atoms in a molecule may be predetermined, it is not possible to control bond lengths, torsion angles, and other parameters of a molecular structure exactly. In this respect, we could anticipate the formation of the $[\mathbf{Mn^{III}_6Cr^{III}}]^{3+}$ complex by molecular recognition of three preorganized building blocks, but we cannot predict its exact molecular structure that is governed by specific crystallization conditions.

Superexchange Interactions. Although we have simulated the DC magnetic data of **1a** using the spin-Hamiltonian in eq 1, which provided the exchange coupling constants J_{Mn-Mn} and J_{Cr-Mn} and the zero-field splitting D_{Mn} (see Table 3), we refrain from a quantitative comparison of the parameter values of **1a** with those of the other $[\mathbf{Mn^{III}_6Cr^{III}}]^{3+}$ compounds, because our spin-Hamiltonian does not take into account intermolecular interactions possibly caused by the $[Cr^{III}(CN)_6]^{3-}$ counterions, which are hydrogen-bonded to the $[\mathbf{Mn^{III}_6Cr^{III}}]^{3+}$ trications. The probable influence of the counterions is corroborated by the rather poor reproduction of the experimental data of **1a**, especially its VTVH data, by the simulations (see Figure S12 in the Supporting Information). Therefore, the parameter values obtained for **1a** are afflicted with considerable uncertainty, since contributions from intermolecular interactions between the cations and anions may account for an overestimation (or underestimation) of the J and D values.

J_{Mn-Mn} Exchange Coupling. The J_{Mn-Mn} exchange interaction between Mn^{III} ions of the same trinuclear triplesalen subunit is slightly antiferromagnetic in all $[\mathbf{Mn^{III}_6Cr^{III}}]^{3+}$ compounds, despite being mediated by the bridging phloroglucinol unit, upon which we based our ligand design with the intention of creating ferromagnetic couplings via the spin-polarization mechanism. Our recent studies on extended phloroglucinol ligands have revealed that their central backbone must be described as the N-protonated tautomer, rather than the O-protonated tautomer, with the main contribution to the resonance hybrid coming from a resonance structure with exocyclic C=C double bonds and C=O double bonds instead of phenolic C−O bonds.[154,183,184] This resonance structure is reminiscent of [6]radialenes and has been termed heteroradialene.[185] Radialenes are alicyclic compounds that exhibit a cross-conjugation of the double-bond system (i.e., radialenes do not possess a delocalized aromatic π system).[186−189] We have identified signatures for heteroradialene formation in our extended phloroglucinol ligands by NMR, electronic absorption, and FT-IR spectroscopy. Our investigations of trinuclear Ni^{II}, Cu^{II}, and Fe^{III} complexes based on these ligands indicate that the heteroradialene resonance structure still prevails in the coordinated deprotonated form of the ligands, although to a lower extent than in the free ligands.[154,183,190]

The C−C bond lengths of the central phloroglucinol rings in the $[\mathbf{Mn^{III}_6Cr^{III}}]^{3+}$ compounds **1**−**6** are in the range of 1.40−1.44 Å, with a mean value of 1.42 Å, which is slightly higher than the mean C−C bond length in the terminal phenolates (1.40 Å) serving as an internal reference. This clearly indicates some heteroradialene character of the central phloroglucinol backbone in $[\mathbf{Mn^{III}_6Cr^{III}}]^{3+}$, which is supported by the electronic absorption spectra exhibiting two strong features in the 27 000−35 000 cm^{-1} region and by the FT-IR spectra showing three strong bands at 1560, 1535, and 1491 cm^{-1}, which are typical signatures for a heteroradialene contribution to the resonance hybrid of the central backbone. In summary, the heteroradialene formation entailing a loss of the delocalized aromatic π system in the central phloroglucinol backbone is the main source of the weak antiferromagnetic J_{Mn-Mn} exchange couplings observed in the $[\mathbf{Mn^{III}_6Cr^{III}}]^{3+}$ compounds.

Interestingly, the J_{Mn-Mn} exchange is slightly stronger in **3a** (J_{Mn-Mn} = −0.85 cm^{-1}) than in **4a**−**6a** (J_{Mn-Mn} = −0.70 cm^{-1}). This correlates with a smaller folding angle $\varphi^{central}$ and a larger θ and may be related to a better $d_\pi-p_\pi$ overlap of the Mn^{III} magnetic orbitals with the orbitals of the phloroglucinol O atoms. In the trinuclear Cu^{II} complexes of the triplesalen ligand, we have observed a dependence of the exchange coupling between the Cu^{II} ions on $\varphi^{central}$, indicating a strengthening of the ferromagnetic coupling with increasing ligand folding.[74] This was attributed to a better pseudo-σ overlap of the magnetic Cu^{II} $d_{x^2-y^2}$ orbital with the O $p_{z'}$ orbital for a stronger ligand folding, with the overlap integral vanishing for a coplanar orientation of the $Cu^{II}N_2O_2$ plane and the plane of the phloroglucinol ring. In the case of the d^4 ion Mn^{III}, a less pronounced ligand folding, such as that encountered in **3**, favors the $d_\pi-p_\pi$ overlap, thus increasing the spin density on the phloroglucinol O atoms, which, in turn, may promote stronger J_{Mn-Mn} superexchange interactions.

J_{Cr-Mn} Exchange Coupling. The J_{Cr-Mn} exchange interaction, which ranges from −3 cm^{-1} to −5 cm^{-1} in **3a**−**6a** and **3c**−**6c** (see Table 3), is the strong interaction in $[\mathbf{Mn^{III}_6Cr^{III}}]^{3+}$. It is strong enough to overcome the weak antiferromagnetic J_{Mn-Mn} exchange in the trinuclear triplesalen subunits, thus enforcing a parallel alignment of the Mn^{III} spins, leading to an overall ferrimagnetic coupling scheme. In the limit of strong exchange ($J \gg D$), this scenario results in an $S_t = {}^{21}/_2$ spin ground state. The existence of this high-spin ground state in $[\mathbf{Mn^{III}_6Cr^{III}}]^{3+}$ is supported by the μ_{eff} values at low temperatures, particularly by those calculated from AC data, and by the magnetization saturation values in the M vs B and VTVH data. The stronger the antiferromagnetic J_{Cr-Mn} exchange and the less antiferromagnetic the J_{Mn-Mn} exchange, the better the stabilization of the $S_t = {}^{21}/_2$ spin ground state. This is illustrated by the variations in the temperature dependence of μ_{eff} and in the magnetization saturation values observed for small changes in the ratio of J_{Cr-Mn} and J_{Mn-Mn}.

However, the zero-field splitting of the Mn^{III} ions is sizable (D_{Mn} = −3 cm^{-1} to −4 cm^{-1}) and of the order of the J_{Cr-Mn} exchange interaction. Therefore, the description of $[\mathbf{Mn^{III}_6Cr^{III}}]^{3+}$ using total spin quantum numbers must be considered as an approximation. This interesting aspect will be elaborated further below.

dx.doi.org/10.1021/ic301406j | Inorg. Chem. 2012, 51, 10929−10954

There is a clear variation in J_{Cr-Mn} within the series of crystalline samples **3a**–**6a** (see Table 3). A comparison of the mean values of the bond distances and angles along the Cr–C≡N–Mn exchange pathway in **3**–**6** (see Table 1) does not hint at significant structural differences. However, closer inspection of the individual values of these parameters in the four compounds reveals strong variations in the distribution of $Mn-N^{C\equiv N}$ bond lengths that correlate with the differences in J_{Cr-Mn}. In this respect, there is a stepwise increase in the number of relatively short $Mn-N^{C\equiv N}$ bonds (2.11–2.14 Å) from zero in compound **3**, in which all the $Mn-N^{C\equiv N}$ bonds are rather long (2.19–2.20 Å), to one in compound **6**, two in compound **4**, and three in compound **5**, with the number of short $Mn-N^{C\equiv N}$ bonds reflecting the number of five-coordinate Mn^{III} ions in each compound. At the same time, **3a** exhibits the weakest J_{Cr-Mn} exchange coupling (J_{Cr-Mn} = −3.00 cm^{-1}), followed by **6a** (J_{Cr-Mn} = −4.00 cm^{-1}), **4a** (J_{Cr-Mn} = −4.50 cm^{-1}), and **5a** (J_{Cr-Mn} = −5.00 cm^{-1}), with the variation in J_{Cr-Mn} being visually reflected in a shift of the minimum in μ_{eff} from 50 K (**3a**) to 74 K (**6a**), 95 K (**4a**), and 99 K (**5a**). This analysis implies that the shortening of a single $Mn-N^{C\equiv N}$ bond in $[Mn^{III}_6Cr^{III}]^{3+}$, which only leads to a minor change in the mean $Mn-N^{C\equiv N}$ bond length, has such a strong impact on the J_{Cr-Mn} exchange interaction along that specific Cr–C≡N–Mn pathway that the average J_{Cr-Mn} coupling constant extracted from simulations of the magnetic data of the entire molecule is significantly enhanced. The strong influence of the $Mn-N^{C\equiv N}$ bond length on J_{Cr-Mn} is corroborated by DFT calculations based on the S_6 symmetric molecular structure of the $[Mn^{III}_6Cr^{III}]^{3+}$ trications in **3**, which exhibits six identical Cr–C≡N–Mn pathways. These calculations indicate that a variation of $d(Mn-N^{C\equiv N})$ by approximately ±5% induces a change in the magnitude of J_{Cr-Mn} by approximately ±35%.

Single-Molecule Magnet Behavior. All $[Mn^{III}_6Cr^{III}]^{3+}$ compounds show a frequency-dependent onset of the out-of-phase component of the AC susceptibility at low temperatures, which is indicative of SMM behavior. As evident from the absence of maxima in the χ''_M vs T plots of **1a** and **3a** in the investigated temperature range, the $[Mn^{III}_6Cr^{III}]^{3+}$ species in these samples exhibit a faster relaxation compared to the various samples of **4**–**6**, for which maxima or shoulders are observed. We have analyzed the slow magnetic relaxation in the different samples of **4**–**6** based on two different representations of the AC susceptibility, namely, χ_{AC} vs T at constant frequencies and χ_{AC} vs ω at constant temperatures. Both representations allow the determination of U_{eff} and τ_0 values by employing the Arrhenius relation described by eq 5. We refrain from a quantitative comparison of τ_0 values because these are generally afflicted with considerable uncertainty, as a result of the fitting procedure to eq 5. The U_{eff} values determined from the two representations of the AC susceptibility differ slightly for each sample, but exhibit the same trends upon comparison of different samples. The crystalline samples **4a**–**6a** exhibit U_{eff} values in the 21.2–27.8 K range, while for **1a** and **3a**, U_{eff} is even lower. It is very satisfying to note that the U_{eff} values inferred from the AC data are consistent with the energy barriers obtained from the spin-Hamiltonian simulations of the DC data (**1a**: 12 K between the $M_{S_t} \approx \pm{}^5/_2$ ground level and the lowest $M_{S_t} \approx \pm{}^1/_2$; **3a**, **3b**: 17 K between the $M_{S_t} \approx \pm{}^{21}/_2$ ground level and the lowest $M_{S_t} \approx \pm{}^1/_2$; **4c**, **5c**: 38 K for the $S_t = {}^{21}/_2$ spin ground state; **6c**: 33 K for the $S_t = {}^{21}/_2$ spin ground state; see Figures S18–S21 in the Supporting Information). These values indicate that $[Mn^{III}_6Cr^{III}]^{3+}$ is not an exceptionally slow relaxing SMM. We will now discuss the different factors contributing to the overall relaxation behavior of $[Mn^{III}_6Cr^{III}]^{3+}$.

Importantly, there are two mechanisms to overcome the anisotropy barrier in an SMM: via a thermal pathway over the top of the barrier or via QTM through the barrier. The height of the anisotropy barrier is usually given as $D_{S_t} \times S_t^2$ (for integer spin systems).[3−5] However, this is merely a rough approximation, implying that there is no significant mixing of M_S levels of excited spin states with those of the ground-state multiplet, which holds true in the limit of strong exchange ($J \gg D$).[191,192]

Another important aspect is the origin of D_{S_t}. As anisotropic and dipolar interactions usually provide only minor contributions to the anisotropy of the ground state, the main source of D_{S_t} is the projection of the single-site anisotropies D_i onto the spin ground state.[193] The well-established spin projection formulas[194] provide good guidance to how single-site zero-field splitting tensors contribute to the tensor of the total spin ground state, especially when the number of contributing spin centers is increased. However, these formulas are derived for the limit of strong exchange ($J \gg D$).

Employing the exact spin-Hamiltonian in eq 1, which takes into account the relative orientations of the local anisotropy tensors, and performing a full-matrix diagonalization, which circumvents a restriction of the analysis to the limits of weak or strong exchange, allows one to accurately evaluate the anisotropy barrier in $[Mn^{III}_6Cr^{III}]^{3+}$. Figure 15 illustrates the low-lying energy levels of a spin system as in $[Mn^{III}_6Cr^{III}]^{3+}$ that were exemplarily calculated along the S_6 quantization axis for J_{Mn-Mn} = 0.00 cm^{-1}, J_{Cr-Mn} = −5.00 cm^{-1}, D_{Mn} = −3.00 cm^{-1}, D_{Cr} = 0.00 cm^{-1}, and g_i = 1.98, while assuming different arrangements of the local Mn^{III} anisotropy tensors: an octahedral arrangement corresponding to an angle ϑ = 54.7° between the molecular S_6-axis and the Mn^{III} Jahn–Teller axes, which is approximately realized in a $[Mn^{III}_6Cr^{III}]^{3+}$ analogue based on a mononucleating salen ligand;[195,196] the approximate scenario in our $[Mn^{III}_6Cr^{III}]^{3+}$ complexes with ϑ = 37.5°; and a collinear arrangement (ϑ = 0°). In the octahedral case, the resulting $S_t = {}^{21}/_2$ ground state is completely isotropic due to a cancellation of the local anisotropy tensors, thus precluding SMM behavior. This is consistent with the experimental results for the above-mentioned $[Mn^{III}_6Cr^{III}]^{3+}$ analogue.[195,196] In contrast, the calculations for our $[Mn^{III}_6Cr^{III}]^{3+}$ SMM indicate an anisotropy barrier of ∼35 K. Importantly, a collinear arrangement of the Mn^{III} anisotropy tensors leads to an anisotropy barrier of ∼75 K. These results demonstrate the strong influence of the relative orientation of the local **D**-tensors on their contribution to the overall anisotropy of the spin ground state and thus to the anisotropy barrier.

Furthermore, the relaxation behavior of an SMM is significantly influenced by the symmetry. The above calculations were performed for strict S_6 molecular symmetry. However, in the solid state, the molecular symmetry is strongly reduced by several factors. For instance, the variations in the occupation of the Mn^{III} sixth coordination sites lead to a reduction of the molecular symmetry of $[Mn^{III}_6Cr^{III}]^{3+}$ in most compounds. This entails perturbations of the electronic structure due to differences in the Cr–C≡N–Mn exchange pathways (vide supra). Not only the symmetry of the molecule itself, but also that of its surroundings, which is governed by the crystal struc-

dx.doi.org/10.1021/ic301406j | Inorg. Chem. 2012, 51, 10929–10954

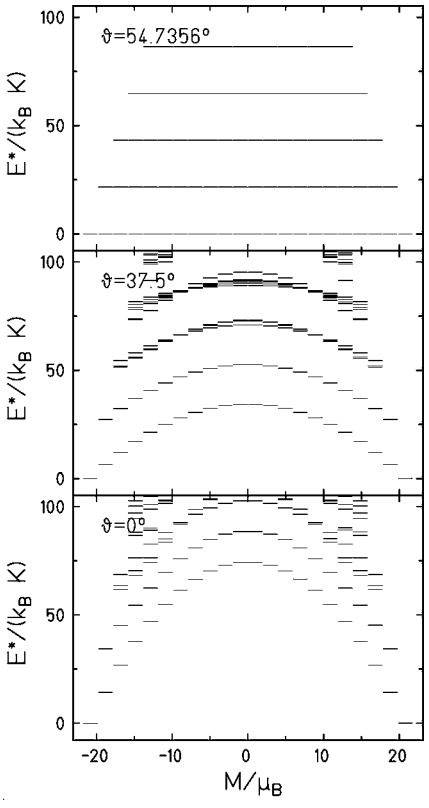

Figure 15. Energy spectra for the $[\mathbf{Mn^{III}_6Cr^{III}}]^{3+}$ spin system (see Figure 9a). Only low-lying energy levels are shown. The *x*-axis represents the magnetization of each eigenstate, which corresponds to the expectation value for a tiny magnetic field along the S_6 quantization axis. The spectra were calculated by a full-matrix diagonalization of the complete spin-Hamiltonian with J_{Mn-Mn} = 0.00 cm^{-1}, J_{Cr-Mn} = −5.00 cm^{-1}, D_{Mn} = −3.00 cm^{-1}, D_{Cr} = 0.00 cm^{-1}, and g_i = 1.98, while assuming different arrangements of the local Mn^{III} anisotropy tensors: an octahedral arrangement corresponding to an angle ϑ = 54.7° between the molecular S_6 axis and the Mn^{III} Jahn−Teller axes (top panel); the arrangement approximately realized in $[\mathbf{Mn^{III}_6Cr^{III}}]^{3+}$ with ϑ = 37.5° (middle panel); and a collinear arrangement (ϑ = 0°, bottom panel).

ture, are crucial factors that influence the relaxation behavior. In this respect, the $[\mathbf{Mn^{III}_6Cr^{III}}](lac)_3$ compound **3** possesses the highest molecular and crystal symmetry, with the latter implying not only a collinear arrangement of the individual $[\mathbf{Mn^{III}_6Cr^{III}}]^{3+}$ complexes in the crystal structure, but also a highly symmetric environment around each SMM complex. However, because of the regular occupation of the Mn^{III} sixth coordination sites with methanol molecules, **3** also exhibits relatively long $Mn-N^{C\equiv N}$ bonds within all $Cr-C\equiv N-Mn$ pathways and thus a relatively weak J_{Cr-Mn} exchange coupling. This significantly reduces the energy separation of the spin ground state from excited states, whose M_S levels therefore mix strongly with those of the ground state, leading to a lower effective anisotropy barrier. In contrast, the highly asymmetric $[\mathbf{Mn^{III}_6Cr^{III}}]^{3+}$ complexes in **4**−**6** exhibit a better separation of the spin ground state due to the presence of some five-coordinate Mn^{III} ions, which promote stronger J_{Cr-Mn} exchange couplings via shorter $Mn-N^{C\equiv N}$ bonds. This translates into a slower magnetic relaxation in **4a**−**6a** compared to **3a**, as evidenced by AC susceptibility measurements, which mainly reflect the thermal pathway over the anisotropy barrier with some influence from thermally activated QTM, which should be favored by the lower symmetry in **4**−**6**. In this respect, the highest U_{eff} value is observed for **5a**, i.e., for the sample exhibiting the strongest J_{Cr-Mn} coupling and the highest symmetry of all $[\mathbf{Mn^{III}_6Cr^{III}}](BPh_4)_3$ compounds, with respect to the surroundings of the individual $[\mathbf{Mn^{III}_6Cr^{III}}]^{3+}$ complexes. The latter is evidenced by the almost collinear arrangement of the $[\mathbf{Mn^{III}_6Cr^{III}}]^{3+}$ molecules in the crystal structure of **5**, which should minimize magnetic stray fields from neighboring $[\mathbf{Mn^{III}_6Cr^{III}}]^{3+}$ spins and, thus, a possible source of QTM.

In the pure quantum regime, i.e., at much lower temperatures, **3** should exhibit superior properties compared to **4**−**6**, because of its high molecular and crystal symmetry, leading to a suppression of the major rhombic anisotropy terms. In this context, it would also be interesting to evaluate the low-temperature properties of **1**, which exhibits an intermediate molecular symmetry compared to **3** and **4**−**6** by carrying a methanol molecule at every Mn^{III} sixth coordination site while lacking a crystallographically imposed S_6 symmetry. With respect to QTM, the influence of the $[Cr^{III}(CN)_6]^{3-}$ counterions in **1** might be relevant, as these $S = {}^3/_2$ spins are expected to generate magnetic stray fields in the immediate vicinity of the $[\mathbf{Mn^{III}_6Cr^{III}}]^{3+}$ complexes. However, it is difficult to anticipate whether these stray fields have a stronger impact on the quantum dynamics of the SMM than the stray fields of the more distant $S_t = {}^{21}/_2$ spins of neighboring SMM complexes. Low-temperature measurements on single crystals of the different $[\mathbf{Mn^{III}_6Cr^{III}}]^{3+}$ compounds are currently underway and will be reported in due course.

In summary, the SMM behavior of $[\mathbf{Mn^{III}_6Cr^{III}}]^{3+}$ is influenced by several opposing effects. While possessing a high molecular and crystal symmetry, the $[\mathbf{Mn^{III}_6Cr^{III}}](lac)_3$ compound **3** lacks a well-separated $S_t = {}^{21}/_2$ spin ground state due to the combination of a relatively weak J_{Cr-Mn} coupling and a rather strong antiferromagnetic J_{Mn-Mn} coupling. In contrast, the $[\mathbf{Mn^{III}_6Cr^{III}}](BPh_4)_3$ solvates **4**−**6** exhibit the drawback of a reduced symmetry, but this allows at least a strong J_{Cr-Mn} exchange along some of the $Cr-C\equiv N-Mn$ pathways, leading to better stabilization of the $S_t = {}^{21}/_2$ spin ground state. These results indicate that the best $[\mathbf{Mn^{III}_6Cr^{III}}]^{3+}$ SMM would possibly be a $[\mathbf{Mn^{III}_6Cr^{III}}](lac)_3$ compound crystallizing in $R\bar{3}$ with all Mn^{III} ions being five-coordinate, thus combining a strongly stabilized spin ground state with a high molecular and crystal symmetry.

Influence of Sample Crystallinity on the Magnetic Properties. With the aim of gaining further insight into the influence of environmental changes on the SMM properties of $[\mathbf{Mn^{III}_6Cr^{III}}]^{3+}$, we investigated three different sample crystallinities. This was inspired by the well-known influence of solvent content and the nature and orientation of peripheral ligands on the relaxation behavior of $\mathbf{Mn_{12}}$,[17−26,86−95] as well as by the difficulties we encountered in preparing the best samples for our magnetic measurements. Upon removal of the crystals from the mother liquor, we frequently observed the loss of solvent as evidenced by the crystals becoming cloudy or even powdery. We did not perform magnetic measurements on crystals maintained in their mother liquor, because of its contamination with paramagnetic residues from the synthetic procedure. Instead, we investigated samples of freshly isolated crystals that were directly transferred from the mother liquor to the SQUID magnetometer in order to keep the crystal structure essentially intact. Furthermore, we studied samples of air-dried crystals having been kept at room temperature for several days as well as vacuum-dried powder samples, with the different

dx.doi.org/10.1021/ic301406j | Inorg. Chem. 2012, 51, 10929−10954

samples of each compound being prepared from the same batch.

All compounds show some influence of sample crystallinity on the magnetic behavior, with this influence being most pronounced for the $[\mathbf{Mn^{III}_6Cr^{III}}](BPh_4)_3$ solvates **4**−**6**. Both the DC and the AC magnetic behavior of these compounds become increasingly similar when going from the crystalline samples to the vacuum-dried powder samples, as evident from the visual convergence of the respective curves and the comparison of the corresponding J_{Cr-Mn} and U_{eff} values.

Interestingly, the vacuum-dried powder samples **4c**−**6c** exhibit rather strong J_{Cr-Mn} couplings, hinting at a loss of coordinated solvent molecules during sample preparation leading to an increase in five-coordinate Mn^{III} ions and, thus, short Mn−$N^{C\equiv N}$ bonds. This is supported by the results of the elemental analyses carried out on **4c**−**6c**.

The AC data of **5a** and **6a** indicate the presence of $[\mathbf{Mn^{III}_6Cr^{III}}]^{3+}$ SMMs in at least two discrete environments that give rise to significantly different relaxation rates. These environments apparently converge upon a loss of crystallinity, as indicated by a gradual merging of the corresponding AC features into a continuous distribution of subtly different environments, evidenced by α-values in the 0.4−0.5 range for the powder samples **5c** and **6c**. In contrast, the AC data of all samples of **4** can be described by a single relaxation process with a distribution of relaxation times, which implies that there are only small differences in the environments of the individual $[\mathbf{Mn^{III}_6Cr^{III}}]^{3+}$ SMMs in these samples. This allows one to estimate the variation of α with sample crystallinity. While the crystalline samples **4a** and **4b** exhibit very similar α-values (see Table 4), there is a substantial increase in α for the powder sample **4c**, accompanied by a poorer agreement of the fits with the experimental data. This indicates a diversification of the $[\mathbf{Mn^{III}_6Cr^{III}}]^{3+}$ environments in **4c**, as expected for a random powder sample compared to crystals exhibiting long-range order.

In summary, these results highlight the importance of sample handling when investigating SMM behavior. Most notably, it is essential to compare only identically prepared samples when discussing the magnetic properties of different SMMs.

CONCLUSIONS

Most attempts to obtain single-molecule magnets (SMMs) with enhanced magnetic properties are based on the simple equation $U_{eff} = D_{S_t} \times S_t^2$ (for integer spin systems), which has inspired numerous efforts to increase the spin ground state in exchange coupled systems by including anisotropic spin centers. The detailed experimental and theoretical investigation of the structural, spectroscopic, and magnetic properties of several $[\mathbf{Mn^{III}_6Cr^{III}}]^{3+}$ compounds, which are all SMMs, shows, as the main conclusion, that a high-spin ground state and a source of magnetic anisotropy are necessary but not sufficient requirements for a good SMM. In order to achieve a high anisotropy D_{S_t} of the total spin ground state, the molecular symmetry of the complex must be lower than cubic to avoid cancellation of the local anisotropies D_i upon projection onto the spin ground state. This is nicely illustrated by our spin-Hamiltonian simulations of a $[\mathbf{Mn^{III}_6Cr^{III}}]^{3+}$ analogue exhibiting an octahedral arrangement of the local Mn^{III} anisotropy tensors, which leads to a completely isotropic spin ground state precluding SMM behavior. At the same time, the symmetry should be at least C_3 in order to minimize the rhombicity of the ground-state spin and, thus, the probability for quantum-mechanical magnetization tunneling (QTM).

Besides the control of the molecular topology of an SMM, there should be control of the crystal structure, especially with respect to symmetry. Non-collinear orientations of the individual SMM molecules in the crystal structure and nonsymmetrical environments caused by interstitial solvent molecules disturb even the best axial molecular symmetry and, thus, introduce some rhombicity in the ground state, which will promote QTM. We have shown that the crystallization of $[\mathbf{Mn^{III}_6Cr^{III}}]^{3+}$ in a highly symmetric space group can be enforced by employing the rod-shaped anion lactate, which leads to a rod packing with a collinear arrangement of the $[\mathbf{Mn^{III}_6Cr^{III}}]^{3+}$ molecules in the crystal structure.

Another important aspect is the separation of the spin ground state from excited spin states, which translates into the necessity to realize strong exchange couplings. In summary, we can now provide an outlook for a further improvement of our $[\mathbf{M^t_6M^c}]^{n+}$-type SMMs. The detailed investigation of the magnetic properties of $[\mathbf{Mn^{III}_6Cr^{III}}]^{3+}$ indicates that the salen-like ligand environment of the Mn^{III} ions provides a good local source of anisotropy. However, the analysis of the influence of the orientation of the local **D**-tensors on the height of the anisotropy barrier also demonstrates that the Mn^{III} Jahn−Teller axes should be forced into a collinear arrangement to enhance the anisotropy barrier. In this respect, we have synthesized the ligand system triplesalophen, exhibiting a completely sp^2 hybridized backbone, which impedes the strong bending of the Mn^{III} salen subunits observed in $[\mathbf{Mn^{III}_6Cr^{III}}]^{3+}$.[184,197] To further promote high molecular symmetry, the concept of using rod-shaped anions is worth further elaboration. Besides, we will try to employ polar but noncoordinating solvents in order to obtain $[\mathbf{Mn^{III}_6Cr^{III}}]^{3+}$ species that exhibit only five-coordinate Mn^{III} ions. Finally, a severe drawback of the triplesalen ligand is the heteroradialene formation, impeding efficient spin polarization via the central phloroglucinol ring and, thus, leading to a weak antiferromagnetic superexchange interaction between the Mn^{III} ions. In order to improve this scenario, we are employing two synthetic strategies. On the one hand, we are substituting the phloroglucinol O atoms with S atoms, because the higher metal−sulfur covalency should increase the spin density on the S atoms, which, in turn, should give rise to a stronger spin polarization via the central ring. On the other hand, we are substituting the triimine units in the 2,4,6-position of the phloroglucinol ring with saturated triamines, which should preclude heteroradialene formation and, thus, enhance the J_{Mn-Mn} exchange coupling. The results of these investigations will provide insight into how far a rational improvement of SMMs is possible.

ASSOCIATED CONTENT

Supporting Information

Crystallographic files in CIF format for compounds **1**−**5**. Summary of crystallographic data, thermal ellipsoid plots, and selected bond distances and angles for **1**−**5**; packing diagrams for **1**−**3**; representations of the molecular structures of **3** and **6**; additional DC and AC magnetic data for all investigated samples; details of the analysis of the AC susceptibility according to a generalized Debye model. This material is available free of charge via the Internet at http://pubs.acs.org.

dx.doi.org/10.1021/ic301406j | Inorg. Chem. 2012, 51, 10929−10954

AUTHOR INFORMATION

Corresponding Author

*E-mail: thorsten.glaser@uni-bielefeld.de.

Notes

The authors declare no competing financial interest.

ACKNOWLEDGMENTS

We thank the Fonds der Chemischen Industrie and the DFG (FOR945 "Nanomagnets") for financial support. V.H. also gratefully acknowledges the Fonds der Chemischen Industrie for a doctoral fellowship. We are grateful to Professor Arndt Simon (Max Planck Institute for Solid State Research, Stuttgart) for his advice regarding rod packings.

REFERENCES

(1) Sessoli, R.; Gatteschi, D.; Caneschi, A.; Novak, M. A. *Nature* **1993**, *365*, 141−143.
(2) Sessoli, R.; Tsai, H. L.; Schake, A. R.; Wang, S. Y.; Vincent, J. B.; Folting, K.; Gatteschi, D.; Christou, G.; Hendrickson, D. N. *J. Am. Chem. Soc.* **1993**, *115*, 1804−1816.
(3) Gatteschi, D.; Sessoli, R. *Angew. Chem., Int. Ed.* **2003**, *42*, 268−297.
(4) Gatteschi, D.; Sessoli, R.; Villain, J. *Molecular Nanomagnets*; Oxford University Press: Oxford, U.K., 2006.
(5) Christou, G.; Gatteschi, D.; Hendrickson, D. N.; Sessoli, R. *MRS Bull.* **2000**, *25*, 66−71.
(6) Thomas, L.; Lionti, F.; Ballou, R.; Gatteschi, D.; Sessoli, R.; Barbara, B. *Nature* **1996**, *383*, 145−147.
(7) Dei, A.; Gatteschi, D. *Angew. Chem., Int. Ed.* **2011**, *50*, 11852−11858.
(8) Tejada, J. *Polyhedron* **2001**, *20*, 1751−1756.
(9) Tejada, J.; Chudnovsky, E. M.; del Barco, E.; Hernandez, J. M.; Spiller, T. P. *Nanotechnology* **2001**, *12*, 181−186.
(10) Awschalom, D. D.; Di Vincenzo, D. P.; Smyth, J. J. *Science* **1992**, *258*, 414−421.
(11) Leuenberger, M. N.; Loss, D. *Nature* **2001**, *410*, 789−793.
(12) Cornia, A.; Fabretti, A. C.; Pacchioni, M.; Zobbi, L.; Bonacchi, D.; Caneschi, A.; Gatteschi, D.; Biagi, R.; Del Pennino, U.; De Renzi, V.; Gurevich, L.; Van der Zant, H. S. J. *Angew. Chem., Int. Ed.* **2003**, *42*, 1645−1648.
(13) Wedge, C. J.; Timco, G. A.; Spielberg, E. T.; George, R. E.; Tuna, F.; Rigby, S.; McInnes, E. J. L.; Winpenny, R. E. P.; Blundell, S. J.; Ardavan, A. *Phys. Rev. Lett.* **2012**, *108*, 107204.
(14) Timco, G. A.; Carretta, S.; Troiani, F.; Tuna, F.; Pritchard, R. J.; Muryn, C. A.; McInnes, E. J. L.; Ghirri, A.; Candini, A.; Santini, P.; Amoretti, G.; Affronte, M.; Winpenny, R. E. P. *Nat. Nanotechnol.* **2009**, *4*, 173−178.
(15) Lee, C.-F.; Leigh, D. A.; Pritchard, R. G.; Schultz, D.; Teat, S. J.; Timco, G. A.; Winpenny, R. E. P. *Nature* **2009**, *458*, 314−318.
(16) Bogani, L.; Wernsdorfer, W. *Nat. Mater.* **2008**, *7*, 179−186.
(17) Bagai, R.; Christou, G. *Chem. Soc. Rev.* **2009**, *38*, 1011−1026.
(18) Wernsdorfer, W.; Sessoli, R.; Gatteschi, D. *Europhys. Lett.* **1999**, *47*, 254−259.
(19) Aubin, S. M. J.; Sun, Z.; Eppley, H. J.; Rumberger, E. M.; Guzei, I. A.; Folting, K.; Gantzel, P. K.; Rheingold, A. L.; Christou, G.; Hendrickson, D. N. *Inorg. Chem.* **2001**, *40*, 2127−2146.
(20) Boskovic, C.; Pink, M.; Huffman, J. C.; Hendrickson, D. N.; Christou, G. *J. Am. Chem. Soc.* **2001**, *123*, 9914−9915.
(21) Mertes, K. M.; Suzuki, Y.; Sarachik, M. P.; Paltiel, Y.; Shtrikman, H.; Zeldov, E.; Rumberger, E.; Hendrickson, D. N.; Christou, G. *Phys. Rev. Lett.* **2001**, *87*, 227205.
(22) Cornia, A.; Sessoli, R.; Sorace, L.; Gatteschi, D.; Barra, A. L.; Daiguebonne, C. *Phys. Rev. Lett.* **2002**, *89*, 257201.
(23) Sòler, M.; Wernsdorfer, W.; Abboud, K. A.; Huffman, J. C.; Davidson, E. R.; Hendrickson, D. N.; Christou, G. *J. Am. Chem. Soc.* **2003**, *125*, 3576−3588.
(24) Chakov, N. E.; Soler, M.; Wernsdorfer, W.; Abboud, K. A.; Christou, G. *Inorg. Chem.* **2005**, *44*, 5304−5321.
(25) Wernsdorfer, W.; Murugesu, M.; Christou, G. *Phys. Rev. Lett.* **2006**, *96*, 057208.
(26) Hill, S.; Murugesu, M.; Christou, G. *Phys. Rev. B* **2009**, *80*, 174416.
(27) Winpenny, R. E. P. *J. Chem. Soc., Dalton Trans.* **2002**, 1−10.
(28) Long, J. R. In *Chemistry of Nanostructured Materials*; Yang, P., Ed.; World Scientific: Hong Kong, 2003; p 291−315.
(29) Aromi, G.; Brechin, E. K. *Struct. Bonding (Berlin)* **2006**, *122*, 1−67.
(30) Miyasaka, H.; Saitoh, A.; Abe, S. *Coord. Chem. Rev.* **2007**, *251*, 2622−2664.
(31) Roubeau, O.; Clérac, R. *Eur. J. Inorg. Chem.* **2008**, 4325−4342.
(32) Kostakis, G. E.; Ako, A. M.; Powell, A. K. *Chem. Soc. Rev.* **2010**, *39*, 2238−2271.
(33) Murrie, M. *Chem. Soc. Rev.* **2010**, *39*, 1986−1995.
(34) Beltran, L. M. C.; Long, J. R. *Acc. Chem. Res.* **2005**, *38*, 325−334.
(35) Rebilly, J.-N.; Mallah, T. *Struct. Bonding (Berlin)* **2006**, *122*, 103−131.
(36) Atanasov, M.; Comba, P.; Hausberg, S.; Martin, B. *Coord. Chem. Rev.* **2009**, *253*, 2306−2314.
(37) Das, A.; Gieb, K.; Krupskaya, Y.; Demeshko, S.; Dechert, S.; Klingeler, R.; Kataev, V.; Büchner, B.; Müller, P.; Meyer, F. *J. Am. Chem. Soc.* **2011**, *133*, 3433−3443.
(38) Miyasaka, H.; Clerac, R.; Wernsdorfer, W.; Lecren, L.; Bonhomme, C.; Sugiura, K.-i.; Yamashita, M. *Angew. Chem., Int. Ed.* **2004**, *43*, 2801−2805.
(39) Inglis, R.; White, F.; Piligkos, S.; Wernsdorfer, W.; Brechin, E. K.; Papaefstathiou, G. S. *Chem. Commun.* **2011**, *47*, 3090−3092.
(40) Manoli, M.; Inglis, R.; Manos, M. J.; Nastopoulos, V.; Wernsdorfer, W.; Brechin, E. K.; Tasiopoulos, A. J. *Angew. Chem., Int. Ed.* **2011**, *50*, 4441−4444.
(41) Langley, S. K.; Stott, R. A.; Chilton, N. F.; Moubaraki, B.; Murray, K. S. *Chem. Commun.* **2011**, *47*, 6281−6283.
(42) Milios, C. J.; Inglis, R.; Vinslava, A.; Bagai, R.; Wernsdorfer, W.; Parsons, S.; Perlepes, S. P.; Christou, G.; Brechin, E. K. *J. Am. Chem. Soc.* **2007**, *129*, 12505−12511.
(43) Piligkos, S.; Bendix, J.; Milios, C. J.; Brechin, E. K. *Dalton Trans.* **2008**, 2277−2284.
(44) Ako, A. M.; Hewitt, I. J.; Mereacre, V.; Clérac, R.; Wernsdorfer, W.; Anson, C. E.; Powell, A. K. *Angew. Chem., Int. Ed.* **2006**, *45*, 4926−4929.
(45) Waldmann, O.; Ako, A. M.; Güdel, H. U.; Powell, A. K. *Inorg. Chem.* **2008**, *47*, 3486−3488.
(46) Wang, X.-Y.; Avendaño, C.; Dunbar, K. R. *Chem. Soc. Rev.* **2011**, *40*, 3213−3238.
(47) Sokol, J. J.; Hee, A. G.; Long, J. R. *J. Am. Chem. Soc.* **2002**, *124*, 7656−7657.
(48) Schelter, E. J.; Prosvirin, A. V.; Dunbar, K. R. *J. Am. Chem. Soc.* **2004**, *126*, 15004−15005.
(49) Martínez-Lillo, J.; Armentano, D.; De Munno, G.; Wernsdorfer, W.; Julve, M.; Lloret, F.; Faus, J. *J. Am. Chem. Soc.* **2006**, *128*, 14218−14219.
(50) Freedman, D. E.; Jenkins, D. M.; Iavarone, A. T.; Long, J. R. *J. Am. Chem. Soc.* **2008**, *130*, 2884−2885.
(51) Hilfiger, M. G.; Zhao, H.; Prosvirin, A.; Wernsdorfer, W.; Dunbar, K. R. *Dalton Trans.* **2009**, 5155−5163.
(52) Zadrozny, J. M.; Freedman, D. E.; Jenkins, D. M.; Harris, T. D.; Iavarone, A. T.; Mathonière, C.; Clérac, R.; Long, J. R. *Inorg. Chem.* **2010**, *49*, 8886−8896.
(53) Pedersen, K. S.; Schau-Magnussen, M.; Bendix, J.; Weihe, H.; Palii, A. V.; Klokishner, S. I.; Ostrovsky, S.; Reu, O. S.; Mutka, H.; Tregenna-Piggott, P. L. W. *Chem.—Eur. J.* **2010**, *16*, 13458−13464.
(54) Pedersen, K. S.; Dreiser, J.; Nehrkorn, J.; Gysler, M.; Schau-Magnussen, M.; Schnegg, A.; Holldack, K.; Bittl, R.; Piligkos, S.; Weihe, H.; Tregenna-Piggott, P.; Waldmann, O.; Bendix, J. *Chem. Commun.* **2011**, *47*, 6918−6920.

(55) Mironov, V. S.; Chibotaru, L. F.; Ceulemans, A. *J. Am. Chem. Soc.* **2003**, *125*, 9750−9760.
(56) Sorace, L.; Benelli, C.; Gatteschi, D. *Chem. Soc. Rev.* **2011**, *40*, 3092−3104.
(57) Rinehart, J. D.; Long, J. R. *Chem. Sci.* **2011**, *2*, 2078−2085.
(58) Sessoli, R.; Powell, A. *Coord. Chem. Rev.* **2009**, *253*, 2328−2341.
(59) Katoh, K.; Isshiki, H.; Komeda, T.; Yamashita, M. *Coord. Chem. Rev.* **2011**, *255*, 2124−2148.
(60) Ishikawa, N.; Sugita, M.; Ishikawa, T.; Koshihara, S.; Kaizu, Y. *J. Am. Chem. Soc.* **2003**, *125*, 8694−8695.
(61) Gonidec, M.; Luis, F.; Vílchez, À.; Esquena, J.; Amabilino, D. B.; Veciana, J. *Angew. Chem., Int. Ed.* **2010**, *49*, 1623−1626.
(62) Guo, Y.-N.; Xu, G.-F.; Wernsdorfer, W.; Ungur, L.; Guo, Y.; Tang, J.; Zhang, H.-J.; Chibotaru, L. F.; Powell, A. K. *J. Am. Chem. Soc.* **2011**, *133*, 11948−11951.
(63) Hewitt, I. J.; Tang, J.; Madhu, N. T.; Anson, C. E.; Lan, Y.; Luzon, J.; Etienne, M.; Sessoli, R.; Powell, A. K. *Angew. Chem., Int. Ed.* **2010**, *49*, 6352−6356.
(64) Rinehart, J. D.; Fang, M.; Evans, W. J.; Long, J. R. *Nat. Chem.* **2011**, *3*, 538−542.
(65) Rinehart, J. D.; Fang, M.; Evans, W. J.; Long, J. R. *J. Am. Chem. Soc.* **2011**, *133*, 14236−14239.
(66) Ako, A. M.; Mereacre, V.; Clérac, R.; Wernsdorfer, W.; Hewitt, I. J.; Anson, C. E.; Powell, A. K. *Chem. Commun.* **2009**, 544−546.
(67) Karotsis, G.; Kennedy, S.; Teat, S. J.; Beavers, C. M.; Fowler, D. A.; Morales, J. J.; Evangelisti, M.; Dalgarno, S. J.; Brechin, E. K. *J. Am. Chem. Soc.* **2010**, *132*, 12983−12990.
(68) Longuet-Higgins, H. C. *J. Chem. Phys.* **1950**, *18*, 265−274.
(69) McConnell, H. M. *J. Chem. Phys.* **1963**, *39*, 1910.
(70) Fernández, I.; Ruiz, R.; Faus, J.; Julve, M.; Lloret, F.; Cano, J.; Ottenwaelder, X.; Journaux, Y.; Munoz, C. *Angew. Chem., Int. Ed.* **2001**, *40*, 3039−3042.
(71) Pardo, E.; Ruiz-Garcia, R.; Cano, J.; Ottenwaelder, X.; Lescouezec, R.; Journaux, Y.; Lloret, F.; Julve, M. *Dalton Trans.* **2008**, 2780−2805.
(72) Glaser, T.; Gerenkamp, M.; Fröhlich, R. *Angew. Chem., Int. Ed.* **2002**, *41*, 3823−3825.
(73) Glaser, T.; Heidemeier, M.; Grimme, S.; Bill, E. *Inorg. Chem.* **2004**, *43*, 5192−5194.
(74) Glaser, T.; Heidemeier, M.; Strautmann, J. B. H.; Bögge, H.; Stammler, A.; Krickemeyer, E.; Huenerbein, R.; Grimme, S.; Bothe, E.; Bill, E. *Chem.—Eur. J.* **2007**, *13*, 9191−9206.
(75) Theil, H.; Frhr. v. Richthofen, C.-G.; Stammler, A.; Bögge, H.; Glaser, T. *Inorg. Chim. Acta* **2008**, *361*, 916−924.
(76) Glaser, T. *Chem. Commun.* **2011**, *47*, 116−130.
(77) Glaser, T.; Heidemeier, M.; Fröhlich, R.; Hildebrandt, P.; Bothe, E.; Bill, E. *Inorg. Chem.* **2005**, *44*, 5467−5482.
(78) Lehn, J.-M. *J. Inclusion Phenom. Macrocyclic Chem.* **1988**, *6*, 351−396.
(79) Cram, D. J. *J. Inclusion Phenom. Macrocyclic Chem.* **1988**, *6*, 397−413.
(80) Busch, D. H. *Chem. Rev.* **1993**, *93*, 847−860.
(81) Glaser, T.; Heidemeier, M.; Weyhermüller, T.; Hoffmann, R.-D.; Rupp, H.; Müller, P. *Angew. Chem., Int. Ed.* **2006**, *45*, 6033−6037.
(82) Glaser, T.; Heidemeier, M.; Krickemeyer, E.; Bögge, H.; Stammler, A.; Fröhlich, R.; Bill, E.; Schnack, J. *Inorg. Chem.* **2009**, *48*, 607−620.
(83) Krickemeyer, E.; Hoeke, V.; Stammler, A.; Bögge, H.; Schnack, J.; Glaser, T. *Z. Naturforsch.* **2010**, *65b*, 295−303.
(84) Hoeke, V.; Gieb, K.; Müller, P.; Ungur, L.; Chibotaru, L. F.; Heidemeier, M.; Krickemeyer, E.; Stammler, A.; Bögge, H.; Schröder, C.; Schnack, J.; Glaser, T. *Chem. Sci.* **2012**, *3*, 2868−2882.
(85) Frhr. v. Richthofen, C.-G.; Stammler, A.; Bögge, H.; DeGroot, M. W.; Long, J. R.; Glaser, T. *Inorg. Chem.* **2009**, *48*, 10165−10176.
(86) Aubin, S. M. J.; Sun, Z.; Pardi, L.; Krzystek, J.; Folting, K.; Brunel, L.-C.; Rheingold, A. L.; Christou, G.; Hendrickson, D. N. *Inorg. Chem.* **1999**, *38*, 5329−5340.
(87) Tsai, H.-L.; Chen, D.-M.; Yang, C.-I.; Jwo, T.-Y.; Wur, C.-S.; Lee, G.-H.; Wang, Y. *Inorg. Chem. Commun.* **2001**, *4*, 511−514.
(88) Sòler, M.; Wernsdorfer, W.; Sun, Z.; Huffman, J. C.; Hendrickson, D. N.; Christou, G. *Chem. Commun.* **2003**, 2672−2673.
(89) del Barco, E.; Kent, A. D.; Chakov, N. E.; Zakharov, L. N.; Rheingold, A. L.; Hendrickson, D. N.; Christou, G. *Phys. Rev. B* **2004**, *69*, 020411(R).
(90) Hill, S.; Anderson, N.; Wilson, A.; Takahashi, S.; Petukhov, K.; Chakov, N. E.; Murugesu, M.; North, J. M.; del Barco, E.; Kent, A. D.; Dalal, N. S.; Christou, G. *Polyhedron* **2005**, *24*, 2284−2292.
(91) Chakov, N. E.; Lee, S.-C.; Harter, A. G.; Kuhns, P. L.; Reyes, A. P.; Hill, S. O.; Dalal, N. S.; Wernsdorfer, W.; Abboud, K. A.; Christou, G. *J. Am. Chem. Soc.* **2006**, *128*, 6975−6989.
(92) Imaz, I.; Luis, F.; Carbonera, C.; Ruiz-Molina, D.; Maspoch, D. *Chem. Commun.* **2008**, 1202−1204.
(93) Redler, G.; Lampropoulos, C.; Datta, S.; Koo, C.; Stamatatos, T. C.; Chakov, N. E.; Christou, G.; Hill, S. *Phys. Rev. B* **2009**, *80*, 094408.
(94) Burzurí, E.; Carbonera, C.; Luis, F.; Ruiz-Molina, D.; Lampropoulos, C.; Christou, G. *Phys. Rev. B* **2009**, *80*, 224428.
(95) Carbonera, C.; Luis, F.; Campo, J.; Sánchez-Marcos, J.; Camón, A.; Chaboy, J.; Ruiz-Molina, D.; Imaz, I.; van Slageren, J.; Dengler, S.; González, M. *Phys. Rev. B* **2010**, *81*, 014427.
(96) Yoo, J.; Brechin, E. K.; Yamaguchi, A.; Nakano, M.; Huffman, J. C.; Maniero, A. L.; Brunel, L.-C.; Awaga, K.; Ishimoto, H.; Christou, G.; Hendrickson, D. N. *Inorg. Chem.* **2000**, *39*, 3615−3623.
(97) Boskovic, C.; Brechin, E. K.; Streib, W. E.; Folting, K.; Bollinger, J. C.; Hendrickson, D. N.; Christou, G. *J. Am. Chem. Soc.* **2002**, *124*, 3725−3736.
(98) Tomsa, A.-R.; Martinez-Lillo, J.; Li, Y.; Chamoreau, L.-M.; Boubekeur, K.; Farias, F.; Novak, M. A.; Cremades, E.; Ruiz, E.; Proust, A.; Verdaguer, M.; Gouzerh, P. *Chem. Commun.* **2010**, *46*, 5106−5108.
(99) Henderson, J. J.; Koo, C.; Feng, P. L.; del Barco, E.; Hill, S.; Tupitsyn, I. S.; Stamp, P. C. E.; Hendrickson, D. N. *Phys. Rev. Lett.* **2009**, *103*, 017202.
(100) Wernsdorfer, W.; Aliaga-Alcalde, N.; Hendrickson, D. N.; Christou, G. *Nature* **2002**, *416*, 406−409.
(101) Hill, S.; Edwards, R. S.; Aliaga-Alcalde, N.; Christou, G. *Science* **2003**, *302*, 1015−1018.
(102) Boskovic, C.; Bircher, R.; Tregenna-Piggott, P. L. W.; Güdel, H. U.; Paulsen, C.; Wernsdorfer, W.; Barra, A.-L.; Khatsko, E.; Neels, A.; Stoeckli-Evans, H. *J. Am. Chem. Soc.* **2003**, *125*, 14046−14058.
(103) Yang, E.-C.; Wernsdorfer, W.; Hill, S.; Edwards, R. S.; Nakano, M.; Maccagnano, S.; Zakharov, L. N.; Rheingold, A. L.; Christou, G.; Hendrickson, D. N. *Polyhedron* **2003**, *22*, 1727−1733.
(104) Bagai, R.; Wernsdorfer, W.; Abboud, K. A.; Christou, G. *J. Am. Chem. Soc.* **2007**, *129*, 12918−12919.
(105) Ferguson, A.; Parkin, A.; Sanchez-Benitez, J.; Kamenev, K.; Wernsdorfer, W.; Murrie, M. *Chem. Commun.* **2007**, 3473−3475.
(106) Nguyen, T. N.; Wernsdorfer, W.; Abboud, K. A.; Christou, G. *J. Am. Chem. Soc.* **2011**, *133*, 20688−20691.
(107) Glaser, T.; Heidemeier, M.; Lügger, T. *Dalton Trans.* **2003**, 2381−2383.
(108) Sheldrick, G. M. *SADABS 2.10*; University of Göttingen: Göttingen, Germany, 2003.
(109) Sheldrick, G. M. *Acta Crystallogr., Sect. A: Found. Crystallogr.* **2008**, *A64*, 112−122.
(110) Soler, J. M.; Artacho, E.; Gale, J. D.; García, A.; Junquera, J.; Ordejón, P.; Sánchez-Portal, D. *J. Phys.: Condens. Matter* **2002**, *14*, 2745−2779.
(111) http://www.icmab.es/siesta.
(112) Perdew, J. P.; Burke, K.; Ernzerhof, M. *Phys. Rev. Lett.* **1996**, *77*, 3865−3868.
(113) Perdew, J. P.; Burke, K.; Ernzerhof, M. *Phys. Rev. Lett.* **1997**, *78*, 1396.
(114) Troullier, N.; Martins, J. L. *Phys. Rev. B* **1991**, *43*, 1993−2006.
(115) Junquera, J.; Paz, Ó.; Sánchez-Portal, D.; Artacho, E. *Phys. Rev. B* **2001**, *64*, 235111.
(116) Schnack, J. *Condens. Matter Phys.* **2009**, *12*, 323−330.

(117) Mallah, T.; Ferlay, S.; Auberger, C.; Hélary, C.; L'Hermite, F.; Ouahès, R.; Vaissermann, J.; Verdaguer, M.; Veillet, P. *Mol. Cryst. Liq. Cryst.* **1995**, *273*, 141−151.
(118) Ohkoshi, S.-i.; Iyoda, T.; Fujishima, A.; Hashimoto, K. *Phys. Rev. B* **1997**, *56*, 11642.
(119) Usuki, N.; Yamada, M.; Ohba, M.; Okawa, H. *J. Solid State Chem.* **2001**, *159*, 328−335.
(120) Dong, W.; Zhang, W.; Ou-Yang, Y.; Zhu, L.-N.; Liao, D.-Z.; Yoshimura, K.; Jiang, Z.-H.; Yan, S.-P.; Cheng, P. *J. Magn. Magn. Mater.* **2007**, *309*, 7−10.
(121) Dong, W.; Zhu, L.-N.; Song, H.-B.; Liao, D.-Z.; Jiang, Z.-H.; Yan, S.-P.; Cheng, P.; Gao, S. *Inorg. Chem.* **2004**, *43*, 2465−2467.
(122) Griebler, W.-D.; Babel, D. *Z. Naturforsch.* **1982**, *37b*, 832−837.
(123) Toma, L.; Lescouëzec, R.; Vaissermann, J.; Delgado, F. S.; Ruiz-Pérez, C.; Carrasco, R.; Cano, J.; Lloret, F.; Julve, M. *Chem.—Eur. J.* **2004**, *10*, 6130−6145.
(124) O'Keeffe, M.; Andersson, S. *Acta Crystallogr., Sect. A: Cryst. Phys., Diffr., Theor. Gen. Crystallogr.* **1977**, *A33*, 914−923.
(125) Starostin, E. L. *J. Phys.: Condens. Matter* **2006**, *18*, 187−204.
(126) Steinbrenner, U.; Simon, A. *Z. Kristallogr.* **1997**, *212*, 428−438.
(127) Steinbrenner, U.; Simon, A. *Z. Anorg. Allg. Chem.* **1998**, *624*, 228−232.
(128) Schaloske, M. C.; Kienle, L.; Mattausch, H.; Duppel, V.; Simon, A. *Eur. J. Inorg. Chem.* **2011**, 4049−4056.
(129) Jerbi, H.; Hidouri, M.; Ben Amara, M. *J. Rare Earths* **2010**, *28*, 481−487.
(130) Meier, S. F.; Schleid, T. *J. Solid State Chem.* **2003**, *171*, 408−411.
(131) Yong, L.; Hoffmann, S. D.; Fässler, T. F. *Z. Anorg. Allg. Chem.* **2004**, *630*, 1977−1981.
(132) Frisch, G.; Röhr, C. *Z. Naturforsch.* **2005**, *60b*, 1224−1230.
(133) Arroyabe, E.; Kahlenberg, V. *Eur. J. Mineral.* **2011**, *23*, 101−110.
(134) Su, Y.-H.; Luo, F.; Li, H.; Che, Y.-X.; Zheng, J.-M. *Cryst. Eng. Commun.* **2011**, *13*, 44−46.
(135) Klepp, K. O.; Schmidt, H. *Z. Kristallogr. NCS* **2002**, *217*, 567−568.
(136) Thess, A.; Lee, R.; Nikolaev, P.; Dai, H.; Petit, P.; Robert, J.; Xu, C.; Lee, Y. H.; Kim, S. G.; Rinzler, A. G.; Colbert, D. T.; Scuseria, G. E.; Tománek, D.; Fischer, J. E.; Smalley, R. E. *Science* **1996**, *273*, 483−487.
(137) Livolant, F.; Levelut, A. M.; Doucet, J.; Benoit, J. P. *Nature* **1989**, *339*, 724−726.
(138) Livolant, F.; Leforestier, A. *Prog. Polym. Sci.* **1996**, *21*, 1115−1164.
(139) Durand, D.; Doucet, J.; Livolant, F. *J. Phys. II* **1992**, *2*, 1769−1783.
(140) Tilney, L. G. *J. Cell Biol.* **1975**, *64*, 289−310.
(141) Glaser, T.; Heidemeier, M.; Theil, H.; Stammler, A.; Bögge, H.; Schnack, J. *Dalton Trans.* **2010**, *39*, 192−199.
(142) Garde, R.; Villain, F.; Verdaguer, M. *J. Am. Chem. Soc.* **2002**, *124*, 10531−10538.
(143) Mascharak, P. K. *Inorg. Chem.* **1986**, *25*, 245−247.
(144) Glaser, T.; Heidemeier, M.; Fröhlich, R. *C. R. Chim.* **2007**, *10*, 71−78.
(145) Cavallo, L.; Jacobsen, H. *Eur. J. Inorg. Chem.* **2003**, 892−902.
(146) Allen, F. H.; Kennard, O.; Watson, D. G.; Brammer, L.; Orpen, A. G.; Taylor, R. *J. Chem. Soc., Perkin Trans.* **1987**, S1.
(147) Boucher, L. J. *J. Inorg. Nucl. Chem.* **1974**, *36*, 531−536.
(148) Boucher, L. J.; Coe, C. G. *Inorg. Chem.* **1975**, *14*, 1289−1294.
(149) Boucher, L. J.; Coe, C. G. *Inorg. Chem.* **1976**, *15*, 1334−1340.
(150) Boucher, L. J.; Farrell, M. O. *J. Inorg. Nucl. Chem.* **1973**, *35*, 3731−3738.
(151) Boucher, L. J.; Herrington, D. R. *Inorg. Chem.* **1974**, *13*, 1105−1108.
(152) Gohdes, J. W.; Armstrong, W. H. *Inorg. Chem.* **1988**, *27*, 1841−1842.
(153) Dey, K.; De, R. L. *J. Inorg. Nucl. Chem.* **1977**, *39*, 153−155.
(154) Feldscher, B.; Stammler, A.; Bögge, H.; Glaser, T. *Polyhedron* **2011**, *30*, 3038−3047.
(155) Fackler, J. P.; Davis, T. S.; Chawla, I. D. *Inorg. Chem.* **1965**, *4*, 130−132.
(156) Davis, T. S.; Fackler, J. P.; Weeks, M. J. *Inorg. Chem.* **1968**, *7*, 1994−2002.
(157) Dingle, R. *J. Mol. Spectrosc.* **1962**, *9*, 426−427.
(158) Dingle, R. *Acta Chem. Scand.* **1966**, *20*, 33−44.
(159) Barnum, D. W. *J. Inorg. Nucl. Chem.* **1961**, *21*, 221−237.
(160) Lever, A. B. P.; Lewis, J.; Nyholm, R. S. *J. Chem. Soc.* **1962**, 5262−5270.
(161) Piper, T. S.; Carlin, R. L. *Inorg. Chem.* **1963**, *2*, 260−263.
(162) Jørgensen, C. K. *Acta Chem. Scand.* **1962**, *16*, 2406−2410.
(163) van den Bergen, A.; Murray, K. S.; O'Connor, M. J.; West, B. O. *Aust. J. Chem.* **1969**, *22*, 39−48.
(164) Bellitto, C.; Tomlinson, A. A. G.; Furlani, C. *J. Chem. Soc. A* **1971**, 3267−3271.
(165) Lever, A. B. P. *Inorganic Electronic Spectroscopy*, Second Edition); Elsevier: Amsterdam, 1984.
(166) Pal, P. K.; Chowdhury, S.; Drew, M. G. B.; Datta, D. *New J. Chem.* **2002**, *26*, 367−371.
(167) Thibon, A.; England, J.; Martinho, M.; Young, V. G.; Frisch, J. R.; Guillot, R.; Girerd, J.-J.; Münck, E.; Que, L.; Banse, F. *Angew. Chem.* **2008**, *120*, 7172−7175.
(168) Drew, M. G. B.; Cairns, C.; McFall, S. G.; Nelson, S. M. *J. Chem. Soc., Dalton Trans.* **1980**, 2020−2027.
(169) Mitra, K.; Biswas, S.; Lucas, C. R.; Adhikary, B. *Inorg. Chim. Acta* **2006**, *359*, 1997−2003.
(170) Walleck, S.; Theil, H.; Heidemeier, M.; Heinze-Brückner, G.; Stammler, A.; Bögge, H.; Glaser, T. *Inorg. Chim. Acta* **2010**, *363*, 4287−4294.
(171) Bermejo, M. R.; Castiñeiras, A.; Garcia-Monteagudo, J. C.; Rey, M.; Sousa, A.; Watkinson, M.; McAuliffe, C. A.; Pritchard, R. G.; Beddoes, R. L. *J. Chem. Soc., Dalton Trans.* **1996**, 2935−2944.
(172) Srinivasan, K.; Michaud, P.; Kochi, J. K. *J. Am. Chem. Soc.* **1986**, *108*, 2309−2320.
(173) Girerd, J.-J.; Journaux, Y. In *Physical Methods in Bioinorganic Chemistry*; Que, L. J., Ed.; University Science Books: Sausalito, 2000; p 321−374.
(174) Miyasaka, H.; Takahashi, H.; Madanbahsi, T.; Sugiura, K.-i.; Clerac, R.; Nojiri, H. *Inorg. Chem.* **2005**, *44*, 5969−5971.
(175) Pan, F.; Wang, Z.-M.; Gao, S. *Inorg. Chem.* **2007**, *46*, 10221−10228.
(176) Zhang, Y.-Z.; Gao, S.; Wang, Z.-M.; Su, G.; Sun, H.-L.; Pan, F. *Inorg. Chem.* **2005**, *44*, 4534−4545.
(177) Postnikov, A. V.; Kortus, J.; Pederson, M. R. *Phys. Status Solidi B* **2006**, *243*, 2533−2572.
(178) *PeakFit*; AISN Software, Inc., 1995.
(179) Mydosh, J. A. *Spin Glasses: An Experimental Introduction*; Taylor & Francis: London, 1993.
(180) Fischer, K. H.; Hertz, J. A. *Spin Glasses*; Cambridge University Press: Cambridge, U.K., 1993.
(181) Mydosh, J. A. Private communication.
(182) Cole, K. S.; Cole, R. H. *J. Chem. Phys.* **1941**, *9*, 341−351.
(183) Feldscher, B.; Stammler, A.; Bögge, H.; Glaser, T. *Dalton Trans.* **2010**, *39*, 11675−11685.
(184) Frhr. v. Richthofen, C.-G.; Stammler, A.; Bögge, H.; Glaser, T. *J. Org. Chem.* **2012**, *77*, 1435−1448.
(185) Maas, G.; Hopf, H. In *The Chemistry of Dienes and Polyenes, Vol. 1: Synthesis and Transformation of Radialenes*; Rappoport, Z., Ed.; Wiley: Chichester, U.K., 1997; pp 927−977.
(186) Hopff, H.; Wick, A. K. *Helv. Chim. Acta* **1961**, *44*, 380−386.
(187) Hopf, H.; Maas, G. *Angew. Chem., Int. Ed.* **1992**, *31*, 931−954.
(188) Hopf, H. *Classics in Hydrocarbon Chemistry*; Wiley−VCH: New York, 2000; pp 290−300.
(189) Gholami, M.; Tykwinski, R. R. *Chem. Rev.* **2006**, *106*, 4997−5027.

(190) Feldscher, B.; Krickemeyer, E.; Moselage, M.; Theil, H.; Hoeke, V.; Kaiser, Y.; Stammler, A.; Bögge, H.; Glaser, T. *Sci. China: Chem.* **2012**, *55*, 951−966.
(191) Pieper, O.; Guidi, T.; Carretta, S.; van Slageren, J.; El Hallak, F.; Lake, B.; Santini, P.; Amoretti, G.; Mutka, H.; Koza, M.; Russina, M.; Schnegg, A.; Milios, C. J.; Brechin, E. K.; Julià, A.; Tejada, J. *Phys. Rev. B* **2010**, *81*, 174420.
(192) Carretta, S.; Guidi, T.; Santini, P.; Amoretti, G.; Pieper, O.; Lake, B.; Slageren, J. v.; El Hallak, F.; Wernsdorfer, W.; Mutka, H.; Russina, M.; Milios, C. J.; Brechin, E. K. *Phys. Rev. Lett.* **2008**, *100*, 157203.
(193) Abragam, A.; Bleaney, B. *Electron Paramagnetic Resonance of Transition Ions*; Clarendon Press, Oxford, U.K., 1970.
(194) Bencini, A.; Gatteschi, D. *Electron Paramagnetic Resonance of Exchanged Coupled Systems*; Springer−Verlag: Berlin, 1990.
(195) Shen, X.; Li, B.; Zou, J.; Xu, Z.; Yu, Y.; Liu, S. *Transition Met. Chem. (Dordrecht, Neth.)* **2002**, *27*, 372−376.
(196) Choi, H. J.; Sokol, J. J.; Long, J. R. *J. Phys. Chem. Solids* **2004**, *65*, 839−844.
(197) Frhr. v. Richthofen, C.-G.; Stammler, A.; Bögge, H.; Glaser, T. *Eur. J. Inorg. Chem.* **2011**, *2011*, 49−52.